DE GRUYTER
OPEN

DOI 10.1515/ama-2017-0013

acta mechanica et automatica, vol.11 no.2 (2017)

STIFFNESS ANALYSIS OF 4-LINK COUPLER MECHANISM USED IN LOW FLOOR TRAMS

TOMASZ CZAUDERNA*, MICHAŁ MANIOWSKI**

Cracow City Transportation Company (MPK SA.), ul. Św. Wawrzyńca 13, 31-060 Cracow, Poland
**Cracow University of Technology, Institute of Automobiles and IC Engines, adress

tczauder@mpk.krakow.pl, mmaniowski@pk.edu.pl

received 27 May 2015, revised 9 February 2017, accepted 13 February 2017

Abstract: The paper presents elastokinematic analysis of spatial, 4-link coupler system used in low floor tram power-trains with classic drive bogies. This article is a continuation of previous work, where were analysed only the kinematic properties of such coupling. In this paper, the experimental characterization of linear and angular stiffness of metal and rubber bushing installed in the coupler rods. Estimated stiffness coefficients were then inserted into the coupler model with compliant bushings jointed with perfectly rigid platforms and rods. Stiffness matrix of the coupler was calculated and its selected coefficients were interpreted.

Key words: Low Floor Tram, Power Train, Multi-Link Couplers, Elasto-Kinematic Analysis

1. INTRODUCTION

The paper goal is elasto-kinematic analysis of 4-link couplers (Flender) utilized in power trains (Fig.1a) of low-floor trams (Cracow City Transport Company, Madej, 2000).

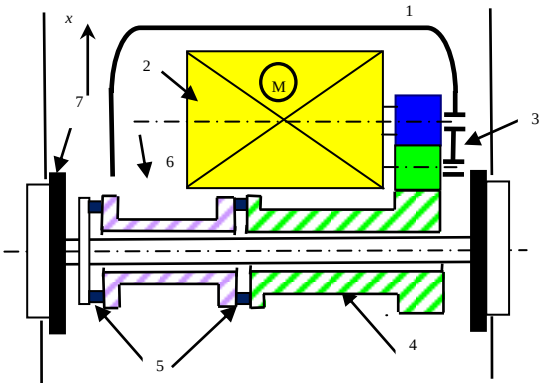

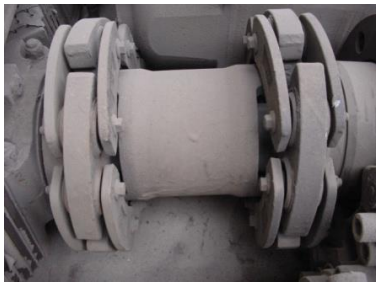

Fig. 1. Typical configuration of tram power train, b) actual 4-link coupler (FLENDER); (1) boogie, 2) electric motor, (3) reduction gear, (4) hollow, (5) four-link couplers, (6) intermediate hollow, (7) axle with rail wheels

These couplings are used to compensate for primary suspension misalignments in the bogie (1 – Fig.1a) with full torque (6000÷24000 Nm) transmission between the gear unit and the powered wheel set shaft. They permit very large shaft displacements and allow major misalignments between the axle and the gear unit while generating only very slight reaction forces.

In the actual 4-link coupler each link includes compliant bushings (Fig.1b), in form of steel-rubber sleeves, in order to obtain: vibroisolation level, increase of the coupler allowable displacements and the mechanism costs reduction (Czauderna and Maniowski, 2013).

Analyses of 4-link coupler spatial stiffness are not widely described. In most of known literature (Farshidianfar et al., 2000; Frączek et al., 2009; Madej, 2000; Zou et al., 2001) these types of couplers are considered as planar mechanisms. Algorithms for calculation of some components of such couplers stiffness are given in Madej (2000).

In this paper spatial stiffness matrices for: single cylindrical bushing, link with 2 bushings in series, and ultimately whole 4-link coupler, will be determined analytically based on tensor calculus (Farshidianfar et al., 2000).

2. ELASTOKINEMATIC MODEL OF THE COUPLER

2.1. Model assumptions

Kinematic scheme of the 4-link coupling mechanism is presented in Fig. 2. The mechanism model was formulated under the following assumptions (Czauderna and Maniowski, 2013; Madej, 2000):

- rods, shafts and platforms are assumed to be rigid;
- the only source of the system compliance comes frommetal-rubber bushings (Fig.3) which act as joints in points A_i and B_i of the clutch;
- elastokinematic analysis is performed for small, quasi-static displacements;
- the bushings exhibit linear force-deflection characteristics;

DOI 10.1515/ama-2017-0013

– the bushings are described by coaxial symmetry;
– the active shaft (with the reference system $X_aY_aZ_a$) rotates only around its own axis coinciding with OY axis;
– the passive shaft is described by reference system $X_bY_bZ_b$.

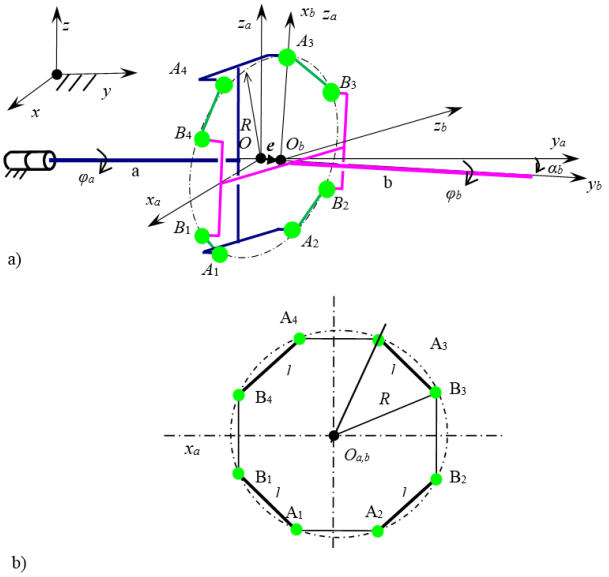

Fig. 2. Scheme of the 4 –link coupler mechanism in general pose (a), Dimensions of the coupler in $x - z$ plane (b)

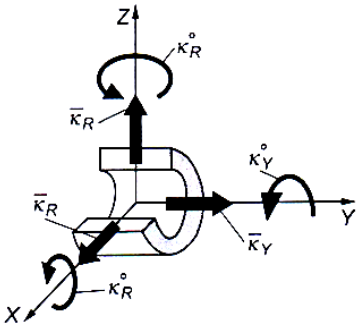

Fig. 3a. Scheme of cylindrical bushing with elastomeric insert (Madej, 2000)

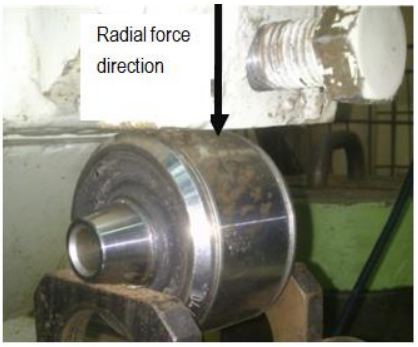

Fig. 3b. Actual bushing installed in test rig

2.2 Compliant bushing model

With the above assumptions, problem of the bushing stiffness (Fig.3a) is described as follows:

$$\mathbf{w}_B = \mathbf{K}_B \ \Delta\mathbf{p}_B \tag{1}$$

where:

$$\Delta\boldsymbol{p_B} = \begin{bmatrix} \Delta x \\ \Delta y \\ \Delta z \\ \Delta\alpha \\ \Delta\varphi \\ \Delta\theta \end{bmatrix} \tag{2}$$

– spatial displacement vector of the sleeve, where the linear displacement is expressed in [m], and angular displacement in [rad];

$$\mathbf{w}_B = \begin{bmatrix} f_x \\ f_y \\ f_z \\ m_x \\ m_y \\ m_z \end{bmatrix} \tag{3}$$

– spatial load vector on the bushing, where force components are expressed in [N], and the components of torque in [Nm];

$$\mathbf{K}_B = \begin{bmatrix} k_{11} & & \cdots & & & 0 \\ & k_{22} & & & & \\ & & k_{33} & & & \\ \cdots & & & k_{44} & & \\ & & & & k_{55} & \\ 0 & & & & & k_{66} \end{bmatrix} \tag{4}$$

– symmetric stiffness matrix of the sleeve with the stiffness coefficients on the matrix diagonal only.

Tab. 1. Coefficients of the bushing stiffness determined from measurements

Stiffness coefficients accord. to eq. (4)	**Notations from [9]**	**Measurements results**
k_{11}= k_{33}	κ_R, [N/m]	3.92x10^6 ± 5%
k_{22}	κ_y [N/m]	1.66x10^6 ± 5%
k_{44}= k_{66}	κ_{Ro} [Nm/rad]	1410 ± 5%
k_{55}	κ_{yo} [Nm/rad]	797 ± 5%

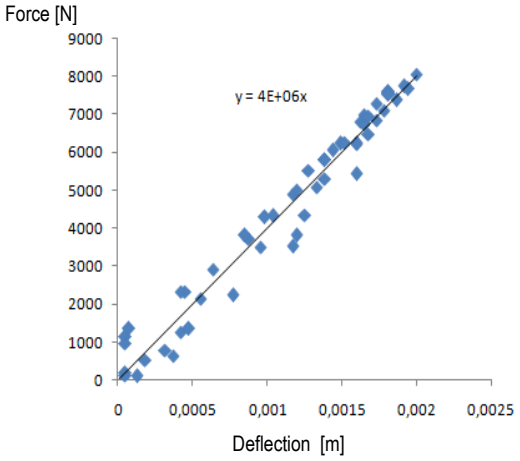

Fig. 4. Radial stiffness characteristic of the considered bushing from measurements

DOI 10.1515/ama-2017-0013

Bushing stiffness parameters in Eq. 4 were determined on the basis of measurements on the test rig (Fig. 3b). Sample of radial force-deflection characteristics is presented in Fig. 4. The considered bushing with rubber insert exhibits linearity in all directions. Determined coefficients of the bushing stiffness are given in Tab. 1.

2.3. Model of coupler link with 2 bushings

Coupler link (Fig. 5), with length l, can be treated as a serial connection of two compliant bushings, located in points A_i and B_i along longitudinal axis (x). It is assumed that the bushings have the same stiffness (K_B) and orientation. Substitute stiffness matrix (K_L) of the coupler link, reduced to joint A_i, is to be evaluated according to the following formula:

$$\mathbf{K}_L = [\mathbf{J}_L(\mathbf{K}_B{}^{-1})\mathbf{J}_L{}^T + \mathbf{K}_B{}^{-1}]^{-1} \tag{5}$$

where:

$$\mathbf{J}_L = \begin{bmatrix} [\mathbf{1}]_{3x3} & [\tilde{\mathbf{l}}]_{3x3} \\ [\mathbf{0}]_{3x3} & [\mathbf{1}]_{3x3} \end{bmatrix} \tag{6}$$

– means a jacobian matrix of transformation of point B to A on the link.

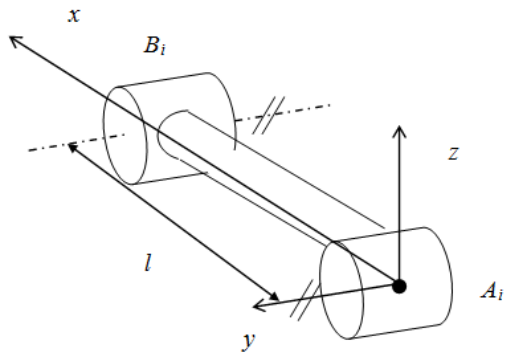

Fig.5. Model of the coupler link with two bushings

Equation (5) concerns a serial connection of two elastic elements, through summing its flexibilities (inverse of the stiffness). Inversion of the diagonal stiffness matrix (4) is straightforward.

In case when the link orientation has to be changed, its stiffness matrix (5) can be transformed in the following way:

$$\mathbf{K}_{LR} = \mathbf{H}^T\,\mathbf{K}_L\mathbf{H} \tag{7}$$

where:

$$\mathbf{H} = \begin{bmatrix} [\mathbf{R}]_{3x3} & [\mathbf{0}]_{3x3} \\ [\mathbf{0}]_{3x3} & [\mathbf{R}]_{3x3} \end{bmatrix} \tag{8}$$

$\boldsymbol{R}$ – orthogonal orientation matrix of the link.

2.4. Model of the coupler with 4 links

The whole coupler mechanism (Fig. 2) can be treated as parallel connection of 4 links described by stiffness matrix (7). Therefore, the coupler stiffness matrix represents a summation of the link stiffnesses transformed to the center of the platform:

$$\mathbf{K}_C = \sum_{i=1}^{4} \mathbf{J}_{C,i}\mathbf{K}_{LR,i}\;\mathbf{J}_{C,i}{}^T \tag{9}$$

where:

$$\mathbf{J}_C = \begin{bmatrix} [\mathbf{1}]_{3x3} & [\tilde{\mathbf{a}}]_{3x3} \\ [\mathbf{0}]_{3x3} & [\mathbf{1}]_{3x3} \end{bmatrix} \tag{10}$$

ã - skew symmetric matrix from vector a, describing position of B point with respect to A point on the coupler link.

3. NUMERICAL EXAMPLE

Numerical example concerns the 4-link coupler according to Fig. 2 with dimensions:

$l_o = 0.1305$ m;

$\gamma = 0.2967$ rad.

The bushing (Fig. 3) stiffness matrix K_B (4), supplemented by the stiffness coefficients determined from measurements, is as follows:

$$K_B = 10^6 \begin{pmatrix} 3.92 & 0 & 0 & 0 & 0 & 0 \\ 0 & 1.66 & 0 & 0 & 0 & 0 \\ 0 & 0 & 3.92 & 0 & 0 & 0 \\ 0 & 0 & 0 & 1.41 & 0 & 0 \\ 0 & 0 & 0 & 0 & 0.797 & 0 \\ 0 & 0 & 0 & 0 & 0 & 1.41 \end{pmatrix} \tag{11}$$

The bushing exhibits the highest linear stiffness (3.92e6 N/m) in both radial (x and z) directions. Axial (y) linear stiffness is about two times lower.

The coupler link (Fig. 5) jacobian matrix (6) is given below:

$$\boldsymbol{J}_L = \begin{pmatrix} 1 & 0 & 0 & 0 & 0 & 0 \\ 0 & 1 & 0 & 0 & 0 & -0.1305 \\ 0 & 0 & 1 & 0 & 0.1305 & 0 \\ 0 & 0 & 0 & 1 & 0 & 0 \\ 0 & 0 & 0 & 0 & 1 & 0 \\ 0 & 0 & 0 & 0 & 0 & 1 \end{pmatrix} \tag{12}$$

The stiffness matrix (5) of the horizontal link (Fig.5) is as follows:

DOI 10.1515/ama-2017-0013

$$\mathrm{K}_L = 10^6 \begin{pmatrix} 1.96 & 0 & 0 & 0 & 0 & 0 \\ 0 & 0.0893 & 0 & 0 & 0 & 0.0058 \\ 0 & 0 & 0.138 & 0 & -0.009 & 0 \\ 0 & 0 & 0 & 0.0007 & 0 & 0 \\ 0 & 0 & -0.009 & 0 & 0.0013 & 0 \\ 0 & 0.0058 & 0 & 0 & 0 & 0.0008 \end{pmatrix} \quad (13)$$

The link exhibits the highest linear stiffness (1.96e6 N/m) in x direction, that is longitudinal link axis. Other (y and z) linear stiffnesses are about 10 times lower. Besides the main stiffness coefficients on the diagonal (13), there appear cross-stiffness coefficients also.

Ultimately, numerical representation of the 4-link coupler (Fig.2) stiffness matrix (9) is as follows:

$$\mathrm{K}_C = 10^6 \begin{pmatrix} 4.0986 & 0 & 0 & 0 & 0 & 0 \\ 0 & 0.5521 & 0 & 0 & 0 & 0 \\ 0 & 0 & 4.0986 & 0 & 0 & 0 \\ 0 & 0 & 0 & 0.0079 & -0.0007 & 0.0032 \\ 0 & 0 & 0 & -0.0007 & 0.0444 & 0.0034 \\ 0 & 0 & 0 & 0.00032 & 0.0034 & 0.0035 \end{pmatrix} \quad (14)$$

The 4-link coupler exhibits the lowest linear stiffness (0.5521e6 N/m) in y direction, what is utilized to take over relative displacements of the coupler axles. Linear stiffness of the coupler in radial directions (x and z) is ten times greater due to links action. The highest torsional stiffness (0.0444e6 Nm/rad) the coupler exhibits about y axis, what is needed for effective transmission of (Fig. 1) engine torque. Two other axes (x and z) are described by low angular stiffness, what enables compensation of the coupler axles slope.

4. CONCLUSIONS

Formulated elastokinematic model enables to analysis of the 4-link coupler design parameters on spatial stiffness of the considered mechanism. Stiffness characteristics of the metal-rubber joints were determined on the basis of test rig measurement.

The single 4-link coupler exhibits the greatest linear stiffness in radial directions (x and z). Stiffness in longitudinal direction (y axis) is about 8 times less, enabling slight compensation of axial displacements of the coupler axles. The coupler exhibits the greatest torsional stiffness about y axis, where the powertrain torque can be transferred. In other directions the coupler torsional stiffness is 7 times less, making possible slight variations of the axles inclination.

Further works include measurements of the actual 4-link coupler used in NGT6 low floor trams in Cracow city transport. Formulation of the 4-link coupler dynamic model is also planned.

REFERENCES

1. Cracow City Transport Company (MPK SA.)
2. **Czauderna T.** (2012), Kinematic analysis of spatial double 4-link coupler system used in low floor tram (in Polish), *Conference of Modern Rail Technologies*, 103-118.
3. **Czauderna T., Maniowski M.** (2013), Elastic-kinematic analysis of spatial 4-link coupler system (in Polish), *Conference of Modern Rail Technologies*, 61-72.
4. **Czauderna T., Grzyb A.** (9/2009), Reaserch on kinematic excitations of trams vibrations (in Polish), *Rail Transport Engineering*, 64-68.
5. **Farshidianfar, M. Ebrahimi, H. Rahnejat, Menday M.T** (2000), Low-frequency torsional vibration of vehicular driveline systems in shuffle, *Multibody Dynamics: Monitoring & Simulation Techniques*, Editors: Homer Rahnejat, Morteza Ebrahimi, Robert Whalley; 263-282.
6. **Frączek J., Wojtyra M.** (2009), *Kinematics of multibody systems* (in Polish), Technical Edition, Warsaw.
7. **Knapczyk J., Maniowski M.** (2006), Elastokinematic Modeling and Study of Five-Rod Suspension with Subframe, *Mechanism and Machine Theory*, 41, 1031-1047.
8. **Madej J.** (2000), *Mechanics of drive torque transmission* (in Polish, Publishing House of Warsaw University of Technology.
9. **Quennouelle C., Gosselin C. M.** (2008), Stiffness Matrix of Compliant Parallel Mechanisms, *Advances in Robot Kinematics: Analysis and Design*, Editors: Jadran Lenarcic, Philippe Wenger, 331-341.
10. **Romaniszyn Z.** (2005), *Boogies suspensions of rail vehilces* (in Polish), Publishing House of Cracow University of Technology.
11. **Zou Z., Zhang Y., Zhang X., Tobler W.** (2001), Modelling and Simulation of Traction Drive Dynamics and Control, *Journal of Mechanical Design*, 123(4), 556-561.

DE GRUYTER
OPEN

DOI 10.1515/ama-2017-0014 acta mechanica et automatica, vol.11 no.2 (2017)

COMPARISON OF CORROSION RESISTANCE IN PHYSIOLOGICAL SALINE SOLUTION OF TWO AUSTENITIC STAINLESS STEELS – 316LV AND REX734

Eliza ROMAŃCZUK*, Zbigniew OKSIUTA*

*Faculty of Mechanical Engineering, Bialystok University of Technology, ul. Wiejska 45C, 15-351 Bialystok, Poland

e.romanczuk@doktoranci.pb.edu.pl, z.oksiuta@pb.edu.pl

received 31 March 2016, revised 14 March 2017, accepted 17 March 2017

Abstract: In this work two austenitic stainless steels, REX734 and 316LV were tested in terms of their microstructure and corrosion properties. The REX734 is a newer generation stainless steel, with modified chemical composition, in comparison to the 316LV grade. Potentiodynamic study of corrosion resistance was conducted in physiological saline solution (0.9% NaCl solution). In spite of the similarities of microstructure, grain size and phase structure in both materials, the corrosion tests revealed that the REX734, with lower nickel and higher nitrogen content, had better corrosion resistance than 316LV. Repassivation potential in the REX734 was almost six times higher than for the 316LV steel. Superior corrosion resistance of the REX734 steel was also confirmed by surface observations of both materials, since bigger and more densely distributed pits were detected in 316LV alloy.

Key word: REX734 Austenitic Stainless Steel, 316LV Austenitic Stainless Steel, Potentiodynamic Corrosion Tests, XRD Analysis, SEM Observation

1. INTRODUCTION

Biomaterials based on metals and metal alloys are commonly used in medicine. They can be used in objects such as implants, plates, screws or surgical instruments as a replacement for human body parts. These materials should meet the requirements of biocompatibility, good mechanical strength and corrosion resistance. It is known that the corrosion resistance is an effective prognostic of the biocompatibility and further application of these materials (Burnat et al., 2014; Sumita et al., 2004; Reclaru et al., 2003; Uggowitzer et al., 2003). From the very large group of biomaterials, an austenitic stainless steel 316LV (ISO 3581-A) is frequently used for various orthopaedic and surgical applications, due to good ductility and fatigue behaviour, decent corrosion resistance, good formability and low cost of production (Thomann and Uggowitzer, 2000, Giordani et al., 2004, Gotman, 1997). This steel however, has some disadvantages including: low biocompatibility, susceptibility to fracture due to fatigue and fretting corrosion, high amount of expensive nickel alloying element, toxicity of corrosion products or insufficient affinity for cells and tissues integrations (Sumita et al., 2004, Yang and Ren, 2010).

Corrosion, as one of the main issues of the austenitic stainless steels, leads to releasing of metal ions. They concentrate on the boundaries of an implant causing toxic and allergic reactions of tissues after relatively short time of implantation (Reclaru et al., 2003, Teoh, 2000). The 316LV steel, most frequently used in surgical applications with high nickel content, has aforementioned disadvantages (Sumita et al., 2004).

Nickel is one of the primary alloying element used in stainless steels production. It is stabilizing Fe-γ (Face Centered Cubic, FCC) austenite phase structure, increasing the stacking fault energy and therefore improving mechanical and fracture properties of steels. On the other hand, nickel ions (products of corrosion) cause toxic and carcinogenic response of the human tissue (Uggowitzer et al., 1996, IARC, 1996). Therefore, this toxic element has been gradually replaced by other strong austenite-stabilizing elements: nitrogen and manganese. Nitrogen occurring in austenitic stainless steel, added up to the solubility limit, improves tensile strengths and corrosion resistance, extends the passives range, promotes passivity that restrains the pitting corrosion and tightens an oxide layer (Yingli and Zhangijan, 2013, Filemonowicz et al., 1995, Bayoumi and Ghanem, 2005). If nitrogen contain is higher than 0.4 wt %, the austenitic stainless steel is considered as high-nitrogen steel. However, the solubility of nitrogen in room temperature is quite low, Sawer placed it at 0.03% and Fry at 0.0015% wt % (Epstein et al.,1929, Gillett, 1928). When nitrogen content exceeds the solubility limit, brittle Cr2N precipitations may be formed, decreasing ductility and corrosion resistance of the steels. REX734 (ISO 5832-9) nitrogen- and niobium-bearing austenitic stainless steel, with reduced nickel content, higher amount of chromium, manganese and nitrogen has been designated to improve and replace the 316LV steel on the market (Giordano et al., 2010).

Basing on the present knowledge it has to be pointed out that available experimental data about corrosion resistance of the REX734 steel is very limited. Therefore, in this work, the potentiodynamic corrosion, phase structure, microstructure and hardness tests, of two conventional stainless steel, 316LV and REX734, commonly used in medical applications were carried out.

2. MATERIALS AND METHODS

Commercially available, 8 mm in diameter rods of austenitic stainless steels 316LV and REX734 were cut into cylinders 5 mm high. Those cylinders were mechanically grinded (using 600-,

DOI 10.1515/ama-2017-0014

800- and 1200-grit papers), polished in an alumina (Al_2O_3) suspension, and cleaned in an ultrasonic bath. Prior to corrosion tests, the samples were kept in the physiological saline solution (0.9% NaCl solution), for 6 hours at room temperature. Potentiodynamic corrosion tests were performed according to ASTM G48 standard and carried out in a three-electrode electrolytic cell consisting of a platinum electrode as counter electrode, a saturated calomel electrode as reference electrode and the sample as a working electrode. The corrosion resistance (Rp), corrosion potential (E_{cor}), current corrosion density (I_{cor}), corrosion rate (C_R), breakdown potential (E_b) and repassivation potential (E_{cp}) were determined using software Volta Master 4. The E_{cor}, E_{cp} and Rp parameters were defined by applying Stern method while the I_{cor} and C_R were defined by Tafel method described elsewhere (McCafferty, 2010). The samples were polarized with the potential rate of 3 mV/s. Before and after the potentiodynamic tests, pH of the solution in which the process was carried out, was measured. The surface of the samples was observed by means of OLYMPUS BX51M Optical Microscope (OM) and Hitachi S-3000N Scanning Electron Microscope (SEM) equipped with Energy Dispersive Spectroscopy (EDS). Vickers hardness of the materials was measured using NEOPHOT 21 microscope equipped with Hanneman's apparatus with a load of 0.1 kg. Chemical analysis for both materials was performed by means of a Thermo ARL Quantris Gas Emission Spectrometer (GES). Phase structure of the prepared samples was studied using a Bruker D8 Advanced X-ray diffraction (XRD) diffractometer with the Cu-Kα radiation (λ = 1.5498 Å). The all diffraction patterns were recorded at room temperature with a step 0.01° in the range of 20° to 100° two theta.

3. RESULTS AND DISCUSSION

Chemical compositions of tested materials are summarized in Tab. 1. As expected the REX734 steel has lower nickel and molybdenum, but higher chromium and manganese content. Higher level of chromium can affect corrosion properties by improving thickness of the passive layer and therefore, reducing corrosion rate of steels (Oksiuta and Och, 2013). Two times greater manganese quantity in the steel can increase the solubility of nitrogen and reduce nickel content (Tverberg, 2014). The REX734 also contains 0.4% of niobium and 0.3% (in wt.%) of nickel. Niobium is added to austenitic stainless steels to reduce formation of detrimental chromium carbides and to prevent reduction of corrosion properties (Sordi and Bueno, 2010). Since the solubility of niobium in austenitic steels is very low, a Laves brittle phase (Fe_2Nb) or Nb(C,N) can be formed what may cause a decrease of ductility and corrosion resistance of steels (Itman Filho et al., 2014). Nitrogen, an interstitial solute element, has a limited solubility in steels, however, it was reported that with the amount of 0.7% it increases the breakdown potential, stabilizes the passive layer and enhances resistance to pitting initiation (Szklarska-Śmiałowska, 2005).

Tab. 1. Chemical composition of the tested austenitic stainless steels (in wt.%)

Material	C	Si	Mn	Cr	Mo	Ni	Nb	N	Fe
REX 734	0.04	0.25	4.10	21.10	2.35	9.10	0.40	0.28	Ball
316 LV	0.03	0.40	1.85	17.25	2.65	14.30	-	-	Ball

The microstructure after etching is shown in Figure 1. After etching, both materials have typical austenitic microstructure with annealing twins and an average grain size of 25±5, measured using the mean interception length technique (according to ASTM E 112-96).

The hardness tests revealed that different chemical composition has no influence on the mechanical properties of both tested steels. This means that hardness of the 316LV steel ($HV_{0.1}$ 371±11) is slightly lower in comparison to the REX734 grade ($HV_{0.1}$ 399±15).

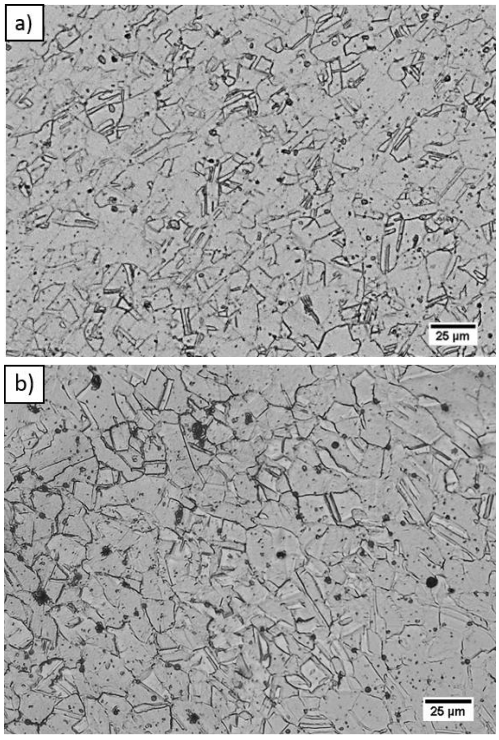

Fig. 1. Typical OM microstructure of the tested steels after etching: a) REX734 and b) 316LV, respectively

The phase structure of the austenitic steels measured by XRD is shown in Fig. 2. The X-ray diffractograms show that the samples contain only the austenite (Fe-γ). No peak of ferrite (Fe-α) was detected.

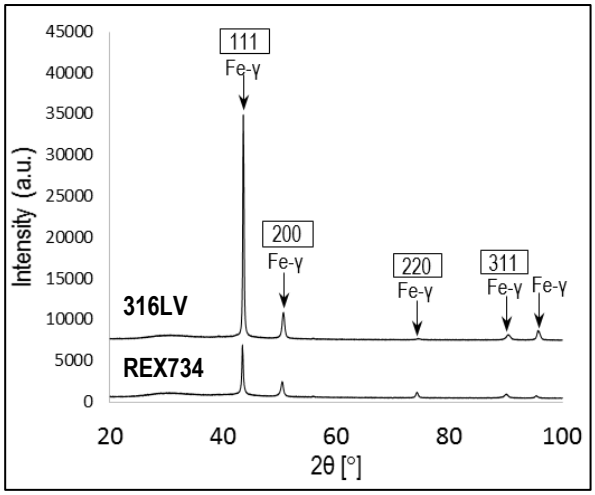

Fig. 2. XRD patterns of the REX734 and 316LV steels

DOI 10.1515/ama-2017-0014

Typical anodic polarization curves of both tested steels are presented in Fig. 3, and major parameters describing the corrosion properties are summarized in Table 2. Analyzing polarization curves, one can observe that in REX734 steel the passive range is about 65% longer in comparison to the 316LV (see Fig. 3). It is known that the transpassivation starts when the breakdown potential is achieved, and this is a moment of initiation of corrosion pits. For the 316LV steel, the breakdown potential took place at 0.7±0.13 V, while for the REX734 steel this potential has considerably higher value (1.15±0.1 V). Similar results were reported by other author (Burnat et al., 2008).

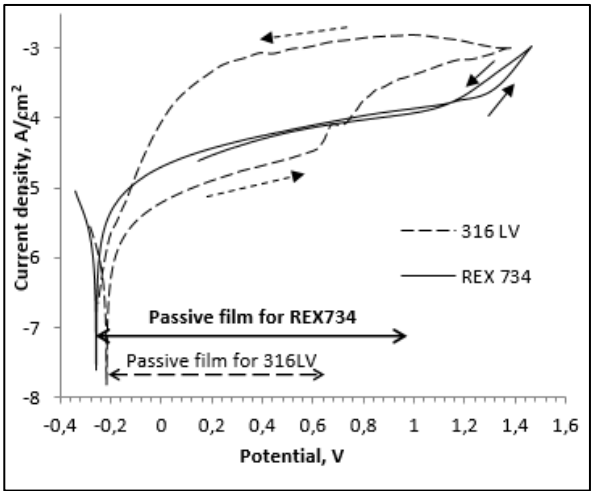

Fig. 3. Typical potentiodynamic polarization curves of: a) REX 734 steel, b) 316 LV steels.

The repassivation potential, measured at the moment when the polarization curve reverses and intersects the forward scan in the passive area (cross over potential measured during forward scan), revealed differences for both tested alloys. For the 316LV the potential is nearly six times lower than for the REX734 and reaches about -0.22V and 1.08V, respectively. Visible large hysteresis loop for 316LV can clearly indicate deep pitting attack and susceptibility of this alloy to crevice corrosion. According to other author (Rondelli et al., 1997), the passivation and repassivation potential is strongly related to the alloying elements concentration on the surface of the sample and the chemical composition inside the pit, mainly pH of a solution and ions concentration. Another author (Bayoumi and Ghanem, 2005) claimed that the hysteresis loop can be strongly suppressed by the presence of nitrogen. Nitrogen, not only delays the pit initiation, but also reduces the pit growth by fast repassivation. This process can be explained as follows. In the aggressive physiological solution, many anions of Cl^-, F^- and others may be introduced. The corrosion mechanism involves movement of these anions through the passive film to the metal-oxide interface, as it is presented in the Fig. 4. Negatively charged nitrogen N^{3-} particles deposited under passive layer can repulsively interact with the Cl^- anions causing desorption reaction and the further removal of these anions. This might be the main reason for fast repassivation process of the pits in the nitrogen containing stainless steels (Bayoumi and Ghanem, 2005; Grabke, 1996).

In potentiodynamic curves of the REX734 small hysteresis loop was clearly observed, thus less corrosion pits after initiation might be expected on the surface of this sample, in comparison to the 316LV grade. Indeed, surface observation in Fig. 5, confirmed these anticipations. Careful stereological analysis of these images revealed that the surface of the 316LV steel has more corrosion pits, which are also bigger in size in comparison to the REX734. Average pits area presented in Table 2 as well as an average pit size of 12.33±0.11 and 5.16±0.18 μm for the 316LV and REX 734 steels, respectively, is significantly higher for the 316LV alloy.

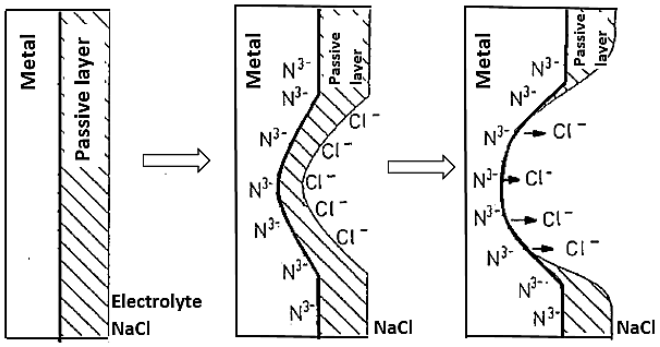

Fig. 4. Schematics view for pit initiation in steel (Grabke, 1996)

However, it is interesting to note that in the REX734 steel (see Fig. 3), after the moment when the curve reaches the repassivation point, the reverse scan follows slightly below the forward curve running and touches it again at 0.45 V. This emphasize that the passive layer is not very stable and pitting corrosion in some areas of the samples can take place. This is probably related to the chemical composition of the REX734 steel; not uniform distribution of main alloying elements on the surface or insufficient quantity of nitrogen content. According to the author's knowledge, this kind of behavior of the stainless steel was not reported by other research workers.

Tab. 2. Major parameters describing corrosion properties of both tested steels

Materials	E_{cor}, V	R_p, Ωcm²	I_{cor}, μA/cm²	C_R, μM/Y	E_b, V	E_{cp}, V	Pits area, %
REX 734	-0.25 ±0.02	7.2 ±0.7	2.8 ±0.4	31.0 ±1	1.15 ±0.10	1.08 ±0.13	1.52 ±0.21
316 LV	-0.27 ±0.04	15.6 ±0.9	3.5 ±0.2	39.8 ±1.50	0.7 ±0.13	-0.22 ±0.11	8.02 ±0.20

Also, in the data presented in Tab. 2 it is visible that the corrosion potentials (E_{cor}) of both steels are similar. The corrosion density (I_{cor}) however, is considerably lower for REX734 steel, which indicates higher corrosion resistance of this material. Furthermore, the polarization resistance (R_p), a parameter which is inversely proportional to the corrosion density, has the higher value for the 316LV and is two times higher than for REX734. Nonetheless, the corrosion rate (C_R) is only about 20% lower for the REX734 in comparison to the high nickel 316lV stainless steel.

In this work, pH of the sodium chloride solution was measured before and after the corrosion tests to find out more about the environment (in which the process took place), pits initiation and stability. The stability of corroding pits depends on the chemical composition of stainless steels, type of electrolyte used and pH value. Information about pH alterations, during various stages of corrosion tests, often provide an explanation about the stability of pits after the corrosion initiation (Bayoumi and Ghanem, 2005; Ghanem et al., 2015).

DOI 10.1515/ama-2017-0014

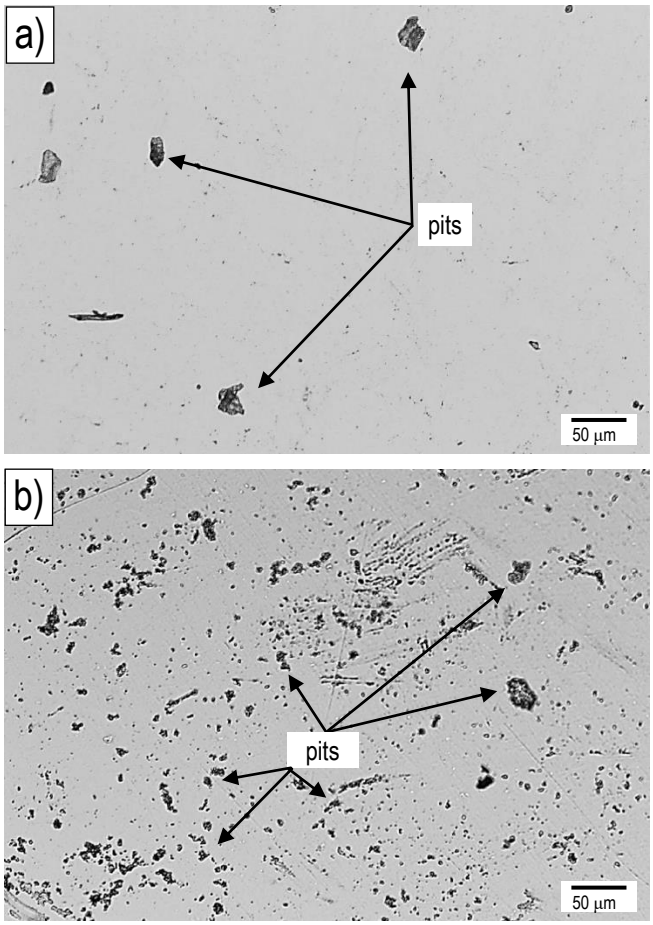

Fig. 5. Surface observations of the samples after the potentiodynamic corrosion tests: a) REX734 steel, b) 316LV steel

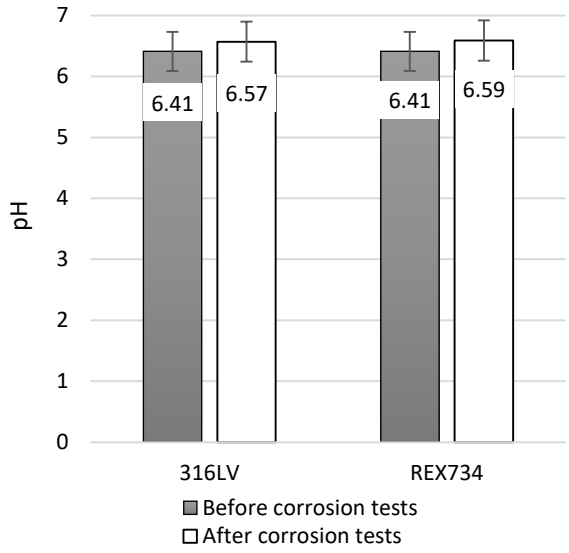

Fig. 6. Results of pH measurement of the 0.9% NaCl solution

At the time of pits formation, the surface of the sample becomes the anode, which means that the metal dissolves into the pit interior (McCafferty, 2010, Baba et al., 2002). Assuming that pit is the cathode, where oxygen is reduced, it leads to the reaction (McCafferty,2010):

$$O_2 + 2H_2O + 4e = 4OH^- \quad (1)$$

Results of pH measurements, presented in Fig. 6, revealed that the solution pH of both materials increased after corrosion tests. It means that OH^- ions, according to the equation (1), might have been released to the solution and form pits on the surface of both materials. On the other hand, it is well known (Grabke, 1996) that nitrogen reduces the acidification in pits, retarding the pitting corrosion process. It seems that in the case of REX734 steel some of the pits can be tightly protected by the passive layer and some of them remained open what confirms the need for increasing the nitrogen content that favours repassivation process.

These data also confirms the role of nitrogen in active corrosion protection of the stainless steel.

4. CONCLUSION

In this paper, the potentiodynamic corrosion tests of two austenitic stainless steels were performed. Commonly used in medical applications the 316LV steel was compared to the REX734 - modified version of the austenitic stainless steel. Both materials have similar microstructure, with an average grain size of 25 μm, and hardness values of $HV_{0.1}$ 371±11 and $HV_{0.1}$ 399±15 for the 316LV and REX734, respectively. XRD analysis also confirmed presence of the only FCC (Fe-γ) austenite phase structure. The corrosion tests revealed however, that the REX734 steel, with lower Ni and higher Cr, Mn and N content, has better corrosion resistance in comparison to the 316LV grade. In spite of the microstructure similarities, higher amount of chromium and nitrogen ensures reduction of the current corrosion density, improves the breakdown potential and fast repassivation potential for the REX734 steel. Also, on the surface of tested 316LV steel, larger area of coarser pits were observed what confirms better potentiodynamic corrosion resistance of the REX734 alloy. pH measurements performed before and after corrosion tests revealed an increase in pH of both materials solutions, associated with pitting corrosion observed on the surface of the tested samples.

The results presented in this work confirmed that an appropriate selection and quantity of the alloying elements have great influence on the corrosion properties of steels. Therefore, it seems reasonable to continue researches leading to obtain optimal chemical composition of the austenitic stainless steel. Thus, future activity will be focused on the production of new generation, nickel-free austenitic stainless steel, with enhanced mechanical properties and corrosion resistance, where expensive and toxic nickel will be entirely replaced by nitrogen.

REFERENCES

1. **Baba H., Kodan T., Katada Y.** (2002), Role of nitrogen on the corrosion behavior of austenitic stainless steels, *Corrosion Science*, 44, 2393–2407.
2. **Bayoumi F.M., Ghanem W.A.** (2005), Effect of nitrogen on the corrosion behavior of austenitic stainless steel in chloride solution, *Meterials Letters*, 59(26), 3311-3314.
3. **Burnat B., Błaszczyk T., Scholl H., Klimek L.** (2008), The influence of TiO_2 sol-gel layers obtained in different temperatures on corrosion properties of biomedical REX 734 alloy, *Engineering of biomaterials*, 77-88, 63-67.
4. **Burnat B., Dercz G., Błaszczyk T.** (2014), Structural analysis and corrosion studies on an ISO 5832-9 biomedical alloy with TiO2 sol-gel layers, *Journal Materials Science*: *Materials in Medicine,* 25, 623-34.

DOI 10.1515/ama-2017-0014

5. **Epstein S., Cross H.C., Groesbeck E.C., Wymore I. J.** (1929), Observations on the iron-nitrogen system, *Bureau of Standards journal of research*, 6, 1005-1009.
6. **Filemonowicz A.C., Clemens D., Quadaakkers W.J.** (1995), The effect of high temperature exposure on the structure and oxidation behaviour of mechanically alloyed ferritic ODS alloys, *Journal of Materials Processing and Technology,* 53, 93-99.
7. **Ghanem W.A., Hussein W.A., Saeed S.N., Bader S.M., Abou Shahba R.M.** (2015)**,** Effect of nitrogen on the corrosion behavior of austenitic stainless steel in chloride solution, *Modern Applied Science*, 9(11), 119-134
8. **Gillett H.W**. (1928), discussion of paper by M. A. Grossman on Oxygen Dissolved in Steel, and Its In- fluence on the Structure, presented at A. S. S. T. convention.
9. **Giordani E.J, Guimaraes V.A, Pinto T.B, Ferreira I.** (2004), Effect of precipitates on the corrosion – fatigue crack initiation of ISO 5832-9 stainless steel biomaterial, *International Journal of Fatigue*, 26, 1129-1136.
10. **Giordano E.J., Allonso-Falleiros N., Ferreira I., Balancin O.** (2010), Electrochemical behavior of two austenitic stainless steel biomaterial, *Rem: Revista Escola de Minas*, 63(1), 159-166.
11. **Gotman I.** (1997), Characteristic of metals used in implants, *Journal of Endourology*, 11(6), 383-389.
12. **Grabke H.J.** (1996), The role of nitrogen in the corrosion of iron and steel, *ISIJ International*, 36(7), 777-786,
13. **IARC**, (1996) Monographs on Evaluation of Carcinogenic Risk to Human: Surgical Implants and Other Foreign Bodies, *Lyon*, 74, 65.
14. **Itman Filho A., Vilarim Silva R., Wandercleiton da Silva Cardoso, Casteletti L.C** (2014), Effect of niobium in the phase transformation and corrosion resistance of one austenit-ic-ferritic stainless steel*, Materials Research Bulletin*, 17(4), 801-806.
15. **McCafferty E.** (2010), *Introduction to corrosion science*, Springer, London.
16. **Oksiuta Z., Och E.** (2013), Corrosion resistance of mechanically alloyed 14% Cr ODS ferritic steel, *Acta Mechanica et Automatica*, 7(1), 38-41.
17. **Reclaru L., Lerf R., Eschles P.Y, Blatter A., Meyer A.M.** (2003), Pitting, crevice and galvanic corrosion of REX734 stainless steel/CoCr orthopedic implant material, *Biomaterials,* 23, 3479-3485.
18. **Rondelli G., Vicentini B., Cigada A.** (1997), Localized corrosion tests on austenitic stainless steels for biomedical applications, *British Corrosion Journal*, 32(3), 193-196.
19. **Simmson J.**W. (1996), Overview: high-nitrogen alloying of stainless steel, *Materials Science and Engineering A*, 207(I.2), 159-169.
20. **Sordi V.L., Bueno L.O.** (2010), Tensile strength and creep behaviour of austenitic stainless steel type 18Cr - 12Ni with niobium additions at 700°C, *Journal of Physics: Conference Series 240*, 012088.
21. **Sumita M., Hanawa T., Teoh S.H.** (2004), Development of nitrogen-containing nickel-free austenitic stainless steels for metallic biomaterials—review, *Materials Science & Engineering C*, 24, 753-760.
22. **Szklarska-Śmiałowska Z.** (2005), *Pitting and Cervice Corrosion, NACE*, Houston, Texas.
23. **Teoh S.H.** (2000), Fatigue of biomaterials: a review, *International Journal of Fatigue*, 22, 825-837.
24. **Thomann U.I, Uggowitzer P. J**. (2000), Wear-corrosion behavior of biocompatible austenitic stainless steel, *Wear*, 239, 48-58.
25. **Tverberg J. C.** (2014) *The role of alloying elements on the fabricability of austenitic stainless steel,* P.E. Metals and Materials Consulting Engineers, Wisconsin.
26. **Uggowitzer P.J., Magdowski R., Speidel M.O.** (1996), Nickel free high nitrogen austenitic steels, *ISIJ International*, 36, 91-8.
27. **Yang K, Ren Y.** (2010), Nickel-free austenitic stainless steels for medical applications, *Science and Technology of Advanced Materials*, 11, 1-13.
28. **Yingli X., Zhangijan Z.** (2013), Processing and structure of a Nitrogen Alloyed Oxide Dispersion Strengthened Austenitic Stainless Steel by mechanical alloying, *Journal of Physics: Conference Series,* 419.

Acknowledgement: This work was supported by the Bialystok University of Technology under the grant No. W/WM/1/2015.

DOI 10.1515/ama-2017-0015

HYBRID PASSIVITY BASED AND FUZZY TYPE-2 CONTROLLER FOR CHAOTIC AND HYPER-CHAOTIC SYSTEMS

Fernando SERRANO[*], Josep M. ROSSELL[**]

[*]Central American Technical University (UNITEC), Tegucigalpa, Zona Jacaleapa, Honduras
[**]Department of Mathematics, Universitat Politècnica de Catalunya (UPC), Av. Bases de Manresa, 61-73 08242-Manresa, Spain

serranofer@eclipso.eu, josep.maria.rossell@upc.edu

received 6 January 2016, revised 9 May 2017, accepted 12 May 2017

Abstract: In this paper a hybrid passivity based and fuzzy type-2 controller for chaotic and hyper-chaotic systems is presented. The proposed control strategy is an appropriate choice to be implemented for the stabilization of chaotic and hyper-chaotic systems due to the energy considerations of the passivity based controller and the flexibility and capability of the fuzzy type-2 controller to deal with uncertainties. As it is known, chaotic systems are those kinds of systems in which one of their Lyapunov exponents is real positive, and hyper-chaotic systems are those kinds of systems in which more than one Lyapunov exponents are real positive. In this article one chaotic Lorentz attractor and one four dimensions hyper-chaotic system are considered to be stabilized with the proposed control strategy. It is proved that both systems are stabilized by the passivity based and fuzzy type-2 controller, in which a control law is designed according to the energy considerations selecting an appropriate storage function to meet the passivity conditions. The fuzzy type-2 controller part is designed in order to behave as a state feedback controller, exploiting the flexibility and the capability to deal with uncertainties. This work begins with the stability analysis of the chaotic Lorentz attractor and a four dimensions hyper-chaotic system. The rest of the paper deals with the design of the proposed control strategy for both systems in order to design an appropriate controller that meets the design requirements. Finally, numerical simulations are done to corroborate the obtained theoretical results.

Key words: Chaos Synchronization, Passive Control, Type-2 Fuzzy Controller, Chaotic System

1. INTRODUCTION

Chaotic systems have been extensively studied during the last decades, due to their complexity and applications in which this phenomenon is found in chemical, physical, power and mechanical systems just to mention some of them (Effati et al., 2014). Chaos is found in some systems when only one Lyapunov exponent is positive yielding a complex dynamic behaviour. Meanwhile, hyper-chaos is found in those systems which have more than one positive Lyapunov exponent where this phenomenon is mostly found in social and economic systems (Effati et al., 2014). In this article, the control of chaotic and hyper-chaotic systems with a fuzzy type-2 and passivity based control is proposed. The main idea of this hybrid control strategy is to take advantage of the energy considerations for the design of passivity based controllers and the flexibility and capability to deal with uncertainties of the fuzzy type-2 controller. Considering the dynamical complexity of chaotic and hyper-chaotic systems, the fuzzy type-2 controller along with the passivity based controller is a suitable control strategy due to the fuzzy type-2 controller part is designed using the expert knowledge in order to stabilize and improve the chaotic and hyper-chaotic performance systems. Passivity based control has been implemented for the control of different kinds of nonlinear systems. For example, in (Dadras and Momeni, 2013) a passivity based and fractional order integral sliding mode control for uncertain fractional order nonlinear system is proposed, where this controller is designed for some kinds of chaotic systems, specifically, a fractional order Chua circuit and a Van Der Pol oscillator. Meanwhile, in Liu et al. (2013) a passivity based attitude controller is implemented for a rigid spacecraft taking into account the respective energy considerations for an appropriate control design. In(Zhu and Huo (2013) a passivity based controller for a model scaled unmanned helicopter is proposed for trajectory linearization control for this kind of unmanned aerial vehicle, where the energy properties of the systems are considered to design a suitable passivity based control strategy. There is a considerable number of passivity based controllers found in literature, but a complete explanation of this controller can be seen in Haddad and Chellaboina (2008). The references cited before are important because they are fundamental for the design of the passivity based controller part to stabilize the chaotic and hyper-chaotic systems analyzed in this article, so it is important to consider several energy properties of these kinds of systems such as dissipativity in order to stabilize these kinds of systems.

Fuzzy type-2 systems have become an alternative for fuzzy type-1 systems because they have two degrees of freedom, composed by a primary and secondary membership functions. Fuzzy type-2 systems are considered as a generalization of fuzzy type-1 systems, in which uncertainty is considered in the membership functions and not only in the linguistic variables (Castillo and Melin, 2008). Fuzzy type-2 systems process consists in the following steps: a fuzzifier, an inference engine, a type reducer and a defuzzifier (Karnik et al., 1999; Mendel, 2007b; Turksen, 1999). Fuzzy type-2 controllers have been implemented recently and are evolving continuously nowadays. For example, in Fayek et al. (2014) a controller based on optimal fuzzy type-2 systems is proposed, where the gains of the controller are optimized using particle swarm optimization to implement this controller in a real

DOI 10.1515/ama-2017-0015

time setup. Different examples of fuzzy type-2 controllers can be found in Castillo and Melin (2014) where some bio-inspired optimization algorithms are implemented to find the parameters and structure of the fuzzy type-2 controllers. Based on this theoretical background, a fuzzy type-2 and a passivity based controller for chaotic and hyper-chaotic systems are proposed, considering the advantages of fuzzy type-2 controllers (Fayek et al., 2014) with the combination of a passivity based controller which have proved to be effective due to its energy consideration. In this article a chaotic Lorentz attractor and a hyper chaotic 4D systems (Effati et al., 2014) are studied to apply the proposed control strategy. Before deriving the proposed controller, an analysis of the stability properties of both systems is performed by studying their eigenvalues and Lyapunov exponents along with their bifurcation diagrams. The fuzzy type-2 part is designed in order to behave as a state feedback controller (Morales-Mata et al., 2008) while the passivity based part is done using an appropriate storage function to find a suitable control law according to the dissipativity properties of the system. Finally to illustrate the theoretical background proposed in this article, some examples are shown with the conclusions of this work.

2. PROBLEM FORMULATION

Before deriving the proposed control strategy, the definitions of the chaotic and hyper-chaotic systems studied in this article are shown in this section. The proposed controller in this paper is designed for different kinds of chaotic and hyper-chaotic systems, but in this case is only considered the stabilization of a chaotic Lorentz attractor (Richter, 2003), (Ontanon-Garcia and Campos-Canton, 2013) and a 4D chaotic system as shown in (Effati et al., 2014), (Zhou and Huang, 2014). A brief analysis of the chaotic Lorentz attractor and hyper-chaotic 4D system stability properties are done in the following subsections where the Lyapunov exponents are analyzed to determine if the system is either chaotic or hyper-chaotic. Apart from this, bifurcation diagrams for both systems are depicted to analyze their chaotic behaviour.

2.1. Stability Properties of the Chaotic Lorentz Attractor

The studied chaotic system, in this case the Lorentz attractor (forced), is shown in (1) (Richter, 2003; Ontanon-Garcia and Campos-Canton, 2013):

$$\begin{aligned} \dot{x}_1 &= \sigma(x_2 - x_1) + u_1 \\ \dot{x}_2 &= \rho x_1 - x_2 - x_1 x_3 + u_2 \\ \dot{x}_3 &= x_1 x_2 - \beta x_3 + u_3 \\ y(x) &= [x_1 \quad x_2 \quad x_3]^T \end{aligned} \tag{1}$$

where $\mathrm{y(x)}$ is the measured output and x_1, x_2 and x_3 are the state variables. In order to set the system (1) in chaotic regime, the constants are set as follows: $\sigma = 10$, $\rho = 28$ and $\beta = 8/3$ (Richter, 2003; Ontanon-Garcia and Campos-Canton, 2013) and $\mathrm{u_i}$ for $\mathrm{i} = 1,2,3$ are the system inputs.

In order to analyze the stability properties of the Lorentz attractor the Lyapunov exponents are shown in Tab. 1.

As it is shown in Tab. 1, only one Lyapunov exponent is positive, obtained by using the methods explained in Yonemoto and Yanagawa (2007), He et al. (1999), and Chen et al. (2006) but more methodologies can be found in (Protasov and Jungers, 2013), (Dieci and Vleck, 1995)

Tab. 1. Eigenvalues and Lyapunov exponents of the Lorentz attractor system

Number	Eigenvalues	Lyapunov exponents
1	11.8277	2.4716
2	-22.8277	-15.9288
3	-2.6667	-15.5890

The phase portrait for the variables x_1 and x_3 is shown in Fig. 1, where as it is noticed these state variables evince the chaotic behaviour of the Lorentz attractor for specific initial conditions. As it is known, the periodicity of this system can be analyzed using Poincare maps (more details can be found in Haddad and Chellaboina (2008)).

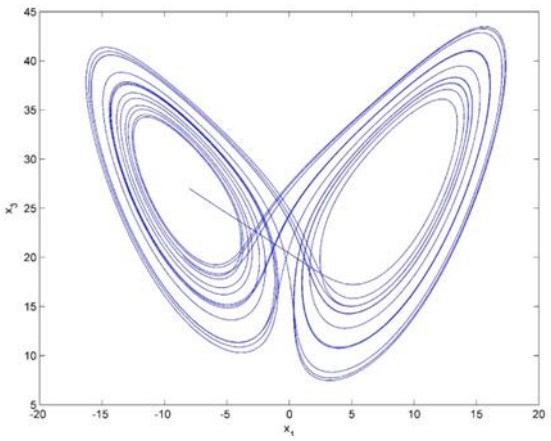

Fig. 1. Phase portrait of the Lorentz attractor

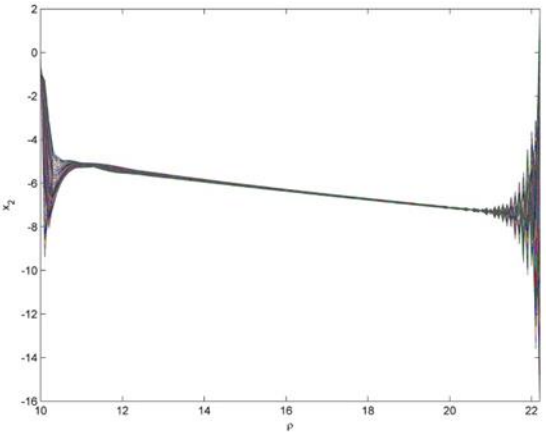

Fig. 2. Bifurcation diagram of the Lorentz attractor

The bifurcation diagram of this system is shown in Fig. 2. It can be noticed that the system (1) is in chaotic regime when $10 \leq \rho \leq 10.5$ and $21 \leq \rho \leq 22$. This system is stabilized by the proposed controller as shown in Section 4.

2.2. Stability Properties of a Hyper-Chaotic 4D System

The studied 4D hyper-chaotic system (forced) (E ffati et al., 2014) used in this paper for stabilization purposes is shown in (2)

DOI 10.1515/ama-2017-0015

$$\begin{aligned}\dot{x}_1 &= ax_1 - x_2x_3 + u_1\\ \dot{x}_2 &= x_1x_3 - bx_2 + u_2\\ \dot{x}_3 &= cx_1x_2 - dx_3 + gx_1x_4 + u_3\\ \dot{x}_4 &= kx_4 - hx_2 + u_4\\ y(x) &= [x_1 \quad x_2\ x_3 \quad x_4]^T\end{aligned} \tag{2}$$

where $y(x)$ is the measured output and x_1, x_2 , x_3 and x_4 are the state variables. In order to yield a hyper - chaotic behaviour, the constants are set as a=8, b=40, c=2, d=14, g=5, h=0.2 and k=0.05; u_i are the system inputs for i=1,2,3,4. The Lyapunov exponents and eigenvalues of the system are shown in Tab. 2.

Tab. 2. Eigenvalues and Lyapunov exponents of the 4D hyper-chaotic system

Number	Eigenvalues	Lyapunov exponents
1	8.0000	7.3246
2	0.0500	0.0110
3	-40.0000	-30.3907
4	-14.0000	-0.5755

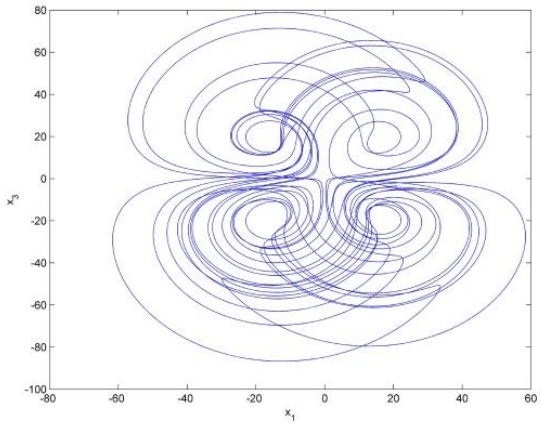

Fig. 3. Phase portrait of the 4D hyper-chaotic system

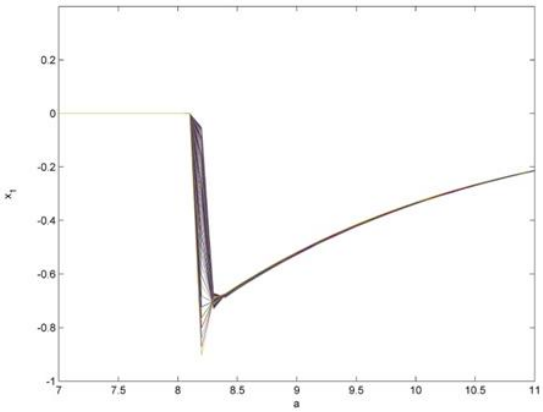

Fig. 4. Bifurcation diagram of the 4D hyper-chaotic system

As it is noticed in Tab. 2, there are two positive eigenvalues and Lyapunov exponents that set the system in hyper-chaotic regime. In Fig. 3 the phase portrait for x_1 and x_3 is shown.

Finally, in Fig. 4 the bifurcation diagram is shown and it can be noticed that the system is stable in the range $7 \leq a \leq 8.2$ and in the range $8.2 \leq a \leq 8.4$ the system is in hyper-chaotic regime. This is the studied hyper - chaotic system that will be stabilized by the proposed control strategy.

3. CONTROLLER DESIGN

In this section the design of the fuzzy type-2 passivity based controllers is shown. In this case, both controllers to stabilize chaotic and hyper-chaotic systems of several kinds and dimensions and later this controller is implemented for the stabilization of the chaotic Lorentz attractor and the 4D hyper-chaotic systems. The control law of both systems is defined as follow:

$$u = u_{pb} + u_{ft2} \tag{3}$$

where u_{pb} is the passivity based component and u_{ft2} is the fuzzy type-2 controller component.

In order to derive both controllers, consider the following chaotic and/or hyper-chaotic system:

$$\begin{aligned}\dot{x}(t) &= F(x(t), u(t))\\ y(t) &= H(x(t))\end{aligned} \tag{4}$$

where $x(t) \in D \subseteq \mathbb{R}^n$, $u(t) \in U$, $y(t) \in Y \subseteq \mathbb{R}^l$, $F: D \times U \to \mathbb{R}^n$ and $H: D \times U \to Y$ with the initial condition $x(t_0) = x_0$ (Haddad and Chellaboina, 2008). In Subsection 3.1 a brief description of fuzzy type-2 controllers is shown first, and then the derivation of the control law of this controller is depicted in this subsection. Then in Subsection 3.2, the passivity based controller is evinced based on the energy and dissipativity considerations of the system.

3.1. Fuzzy type-2 Controller Component

Before explaining the fuzzy type-2 controller part, a brief explanation on fuzzy type-2 system is depicted. Consider a fuzzy type-2 set X represented by:

$$\tilde{A} = \int_{x \in X} \mu_{\tilde{A}}(x)/x = \int_{x \in X} \left(\int_{u \in J_x} f_x(u)/u \right)/x \tag{5}$$

where $J_x \subseteq [0,1]$, $\mu_{\tilde{A}}$ is the membership grade of $x \in X$ which is a type-1 fuzzy set in $[0,1]$; J_x is the primary membership function of x and a secondary membership function of x in $\tilde{A}$ denoted as $f_x(u)$ (Wang and Yu, 2011). The fuzzy type-2 set is in a region bounded by an upper membership function and a lower membership function denoted as $\overline{\mu}_{\tilde{A}(x)}$ and $\underline{\mu}_{\tilde{A}(x)}$ and is called the footprint of uncertainty FOU (Castillo and Melin, 2008; Karnik et al., 1999; Mendel, 2007b; Wang and Yu, 2011).

$$FOU(\tilde{A}) = U_{x \in X} \left[\underline{\mu}_{\tilde{A}(x)}, \overline{\mu}_{\tilde{A}(x)} \right] \tag{6}$$

The fuzzy type-2 process consists in the following steps: fuzzification, inference engine, type reducer and defuzzification. The inference process is done as follow according to the firing strength for the k rule as specified in Karnik et al. (1999):

$$F^k = \left[\underline{f}^k, \overline{f}^k \right] \tag{7}$$

where:

$$\begin{aligned}\underline{f}^k &= \min\left[\underline{\mu}_{E_1^k}(x_1), \ldots, \underline{\mu}_{E_p^k}(x_p) \right]\\ \overline{f}^k &= \min\left[\overline{\mu}_{E_1^k}(x_1), \ldots, \overline{\mu}_{E_p^k}(x_p) \right]\end{aligned} \tag{8}$$

for the $p-$th input (Mendel, 2007a; Mendel and Wu, 2007; Zhou et al., 2009). Then the type reduction is done by finding the centroid of a fuzzy type-2 systems as shown below (Mendel, 2007a;

DOI 10.1515/ama-2017-0015

Mendel and Wu, 2007; Zhou et al., 2009; Mendel, 2005; Singh and Gupta, 2007):

$$y_l = min_{\theta_i \in \left[\underline{f}^k(y_i), \overline{f}^k(y_i)\right]} \frac{\sum_{i=1}^{N} y_i \theta_i}{\sum_{i=1}^{N} \theta_i}$$
$$y_r = max_{\theta_i \in \left[\underline{f}^k(y_i), \overline{f}^k(y_i)\right]} \frac{\sum_{i=1}^{N} y_i \theta_i}{\sum_{i=1}^{N} \theta_i} \quad (9)$$

for N samples. Then the defuzzified output is obtained by:

$$y = \frac{y_l + y_r}{2} = \frac{1}{2}\left(\underline{\xi}_r \quad \underline{\xi}_l\right)\left(\underline{\Theta}_r \quad \underline{\Theta}_l\right) = \xi^T \Theta \quad (10)$$

where ξ and Θ are the defuzzified parameters used in the design of our proposed fuzzy type-2 MIMO controller component for the stabilization of chaotic and hyper-chaotic systems as explained in the following paragraph (Morales-Mata et al., 2008; Kang and Vachtsevanos, 1992) .

Consider the fuzzy type-2 MIMO controller part with p inputs and q outputs, according to the chaotic and hyper-chaotic systems to be stabilized. The controller output (system input) is defined as Castillo and Melin (2014), Martino and Sessa (2014):

$$u_{ft2} = \begin{bmatrix} \xi_1^T \Theta_1 \\ \vdots \\ \xi_q^T \Theta_q \end{bmatrix} = \begin{bmatrix} u_{ft2,1} \\ \vdots \\ u_{ft2,q} \end{bmatrix} \quad (11)$$

Therefore the outputs of the fuzzy type-2 controller to stabilize the chaotic and hyper-chaotic systems are given by

$$u_{ft2,j}(y_j) = \frac{\sum_{i=1}^{N} y_{i,j} f_u(y_{i,j})}{N} \quad (12)$$

where N is the number of samples of the universe of discourse of input $\mathrm{y_j}$ for $j = 1, \ldots, q$ where $\mathrm{f_u(y_{i,j})} = 1$ considering that the secondary membership value is 1 (Wang and Yu, 2011). It is important to consider that if $\mathrm{y_{1,j}} = \mathrm{y_{l,j}}$, $\mathrm{y_{N,j}} = \mathrm{y_{r,j}}$, and N=2 then (10) is obtained. The fuzzy type-2 controller component for the control of the chaotic and hyper-chaotic system is given by Wang and Yu (2011), Castillo and Rico (2006) and Hagras (2004).

With these derivations the fuzzy type-2 controller component

$$u_{ft2,j}(y_j) = \frac{\sum_{i=1}^{N} y_{i,j}}{N} \quad (13)$$

is established. Then, the passivity based controller component is explained in the following subsection.

3.2. Passivity Based Controller Component

Even when there are some control strategies found in literature for chaotic and hyper-chaotic systems such as Effati et al. (2014) and Zhou and Huang (2014), passivity based control is a suitable control strategy for both kinds of systems, and with the addition of a fuzzy type-2 controller the performance is augmented significantly. In order to obtain the passivity based controller component for the two kinds of systems to be stabilized, the following definition is necessary (Liu et al., 2013; Haddad and Chellaboina, 2008)

Definition 1: The system (4) is passive if there exist a storage function $\mathrm{V_s}$ such that:

$$u^T y \geq \dot{V}_s = \frac{\partial V_s}{\partial x} f(x, u) \quad (14)$$

With this definition the passivity based control law component $\mathrm{u_{pb}}$ can be designed in order to meet the passivity condition. With this requirement the controlled chaotic and hyper-chaotic systems are stabilized according to their energy properties. The results obtained in this section are used to stabilize the chaotic Lorentz attractor and 4D hyper-chaotic systems; it is important to consider that the fuzzy type-2 control law $\mathrm{u_{ft2}}$ and the passivity based control law $\mathrm{u_{pb}}$ are designed independently in order to stabilize the two kinds of systems explained in Section 2 and improve the performance of the controlled systems. The appropriate membership functions and rules for the MIMO fuzzy type-2 controller are selected along with the passivity based controller for the two studied systems in this article.

4. PROPOSED CONTROL STRATEGIES FOR THE STUDIED CHAOTIC AND HYPER-CHAOTIC SYSTEMS

In this section the proposed control strategy is designed for the chaotic (Lorentz attractor) and hyper-chaotic system (4D system) studied in this paper. In the following subsections the MIMO fuzzy type-2 component is derived first showing the structure of this part of the control law including the membership functions and rules for the two systems analyzed in this article. Then, the passivity based controller is designed according to the energy considerations shown in Definition 1 in a separate fashion.

4.1. Proposed Control Strategy for the Chaotic Lorentz Attractor

In order to design the proposed control strategy for the Lorentz chaotic attractor shown in (1), the results obtained in Section 3 are implemented deriving first the MIMO fuzzy type-2 controller component and then the passivity based controller component shown in that section.

The MIMO fuzzy type-2 component for the chaotic Lorentz attractor is represented by (15) according to the results shown in (10) and (11) for q=3 due to the dimension of the system is 3 (three inputs and three outputs).

$$u_{ft2} = \begin{bmatrix} \xi_1^T \Theta_1 \\ \xi_2^T \Theta_2 \\ \xi_3^T \Theta_3 \end{bmatrix} = \begin{bmatrix} u_{ft2,1} \\ u_{ft2,2} \\ u_{ft2,3} \end{bmatrix} \quad (15)$$

The membership functions for the inputs of the MIMO fuzzy type-2 controller are shown in Tab. 3 with the membership functions N (negative), Z (zero), and P (positive).

Meanwhile in Tab. 4 the output membership functions of the fuzzy type-2 controller component are shown; where N (negative), Z (zero), P (positive) are the membership functions for each output. In Fig. 5 the respective membership functions for input and output 1 of the fuzzy controller component are shown.

Tab. 3. Input membership functions of the fuzzy type-2 controller component

Input variable	mf1	mf2	mf3
x_1	N	Z	P
x_2	N	Z	P
x_3	N	Z	P

DOI 10.1515/ama-2017-0015

Tab. 4. Output membership functions of the fuzzy type-2 controller component

Output variable	mf1	mf2	mf3
$u_{ft2,1}$	N	Z	P
$u_{ft2,2}$	N	Z	P
$u_{ft2,3}$	N	Z	P

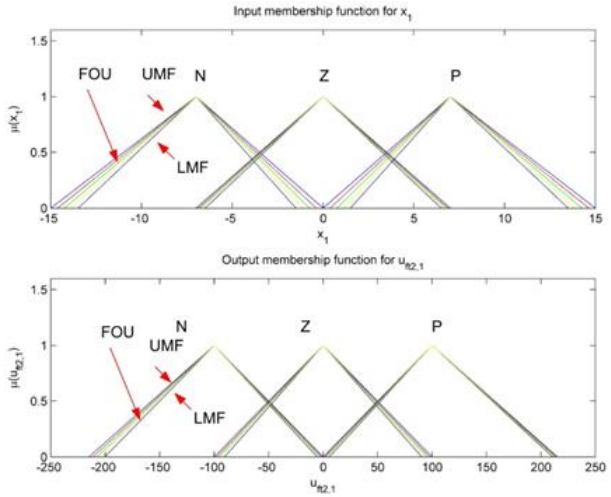

Fig. 5. Membership functions for the input and output 1

The rules of the MIMO fuzzy type-2 controller component for the chaotic Lorentz attractor are in the form:

$$\textit{IF } x_1 = N \textit{ AND } x_2 = N \textit{ AND } x_3 = N \textit{ THEN } u_{ft2,1} = Z \quad \vdots \tag{16}$$

so, the passivity based controller component is defined as follow based on the energy considerations explained in Definition 1, designing the passivity based controller independently, so the input u defined in (1) is $\mathrm{u} = \mathrm{u_{pb}}$. The passivity based control law is derived according to the following theorem:

Theorem 1: A suitable passivity based control law $\mathrm{u_{pb}}$ component for the chaotic Lorentz attractor is found, according to the requirements of Definition 1, if there exists an appropriate storage function such as $\mathrm{V_s}(0) = 0$.

Proof: Consider the following storage function and system input $\mathrm{u_{pb}(t)} = [\mathrm{u_{pb1}} \quad \mathrm{u_{pb2}} \quad \mathrm{u_{pb3}}]^{\mathrm{T}}$, as shown below:

$$V_s(x) = \frac{1}{2}x_1^2 + \frac{1}{2}x_2^2 + \frac{1}{2}x_3^2 \tag{17}$$

Now deriving (17) along the trajectory of (1) and reorganizing yields:

$$\dot{V}_s(x) = \begin{bmatrix} \sigma x_1(x_2 - x_1) \\ \rho x_1 x_2 - x_2^2 - x_1 x_2 x_3 \\ x_1 x_2 x_3 - \beta x_3^2 \end{bmatrix} + y^T u_{pb} \tag{18}$$

Then, in order to make the closed loop system passive, the following control law is chosen:

$$u_{pb} = \begin{bmatrix} -\sigma(x_2 - x_1) \\ -\rho x_1 + x_2 + x_1 x_3 \\ -x_1 x_2 + \beta x_3 \end{bmatrix} + v \tag{19}$$

where v is the input of the passivity based controller. Substituting (19) in (18) yields:

$$\dot{V}_s(x) = y^T v \leq y^T v \tag{20}$$

So the y system is passive by implementing the control law (19), where is defined in (1).

Finally, the input of the passivity based controller v is selected as $\mathrm{v} = -[\mathrm{x_1} \quad \mathrm{x_2} \quad \mathrm{x_3}]^{\mathrm{T}}$. With these results the hybrid control law u shown in (3) can be implemented with (19) as $\mathrm{u_{pb}}$.

4.2. Proposed Control Strategy for the Hyper-Chaotic 4D System

The design of the proposed strategy for the control of the 4D hyper-chaotic system shown in (2) is done by following the procedure explained in Section 3. In this subsection a similar methodology as the implemented in the controller design for the chaotic Lorentz attractor is followed. First, the fuzzy type-2 controller component is derived and then the passivity based controller is derived.

The fuzzy type-2 controller part is given below:

$$u_{ft2} = \begin{bmatrix} \xi_1^T \Theta_1 \\ \xi_2^T \Theta_2 \\ \xi_3^T \Theta_3 \\ \xi_4^T \Theta_4 \end{bmatrix} = \begin{bmatrix} u_{ft2,1} \\ u_{ft2,2} \\ u_{ft2,3} \\ u_{ft2,4} \end{bmatrix} \tag{21}$$

The membership functions for the inputs of the MIMO fuzzy type-2 controller component of the 4D hyper-chaotic system is shown in Table 5, where they are called as N (negative), Z (zero) and P (positive).

Tab. 5. Input membership functions of the fuzzy type-2 controller component

Input variable	mf1	mf2	mf3
x_1	N	Z	P
x_2	N	Z	P
x_3	N	Z	P
x_4	N	Z	P

In Tab. 6 the output membership functions of the fuzzy type-2 controller component for the hyper-chaotic system are shown, where they are denoted as N (negative), Z (zero) and P (positive).

Tab. 6. Output membership functions of the fuzzy type-2 controller component

Output variable	mf1	mf2	mf3
$u_{ft2,1}$	N	Z	P
$u_{ft2,2}$	N	Z	P
$u_{ft2,3}$	N	Z	P
$u_{ft2,4}$	N	Z	P

The fuzzy type-2 membership functions for the input and output 1 of this controller component are shown in Fig. 6.

DOI 10.1515/ama-2017-0015

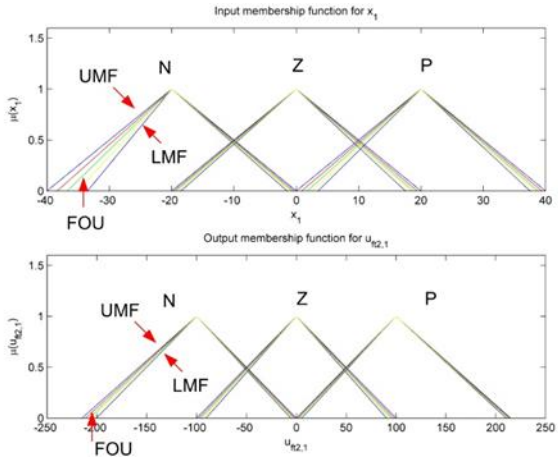

Fig. 6. Membership functions for the input and output 1

The rules of the MIMO fuzzy type-2 controller component implemented for the stabilization of the 4D chaotic system are in the form:

$$IF\ x_1 = N\ AND\ x_2 = P\ AND\ x_3 = Z\ AND\ x_4 = N$$

then

$$u_{ft2,1} = Z \qquad (22)$$

$$\vdots$$

so, the passivity based controller component is defined as follow based on the energy considerations explained in Definition 1, designing the passivity based controller independently, so the input u defined in (2) is $\mathrm{u} = \mathrm{u}_{\mathrm{pb}}$. The passivity based control law is derived according to the following theorem:

Theorem 2: A suitable passivity based control law u_{pb} component for the hyper-chaotic 4D system is found, according to the requirements of Definition 1, if an appropriate storage function such as $\mathrm{V}_{\mathrm{s}}(0) = 0$ is selected.

Proof: Consider the storage function $\mathrm{V}_{\mathrm{s}}(\mathrm{x})$ and system input vector, $\mathrm{u}_{\mathrm{pb}}(\mathrm{t}) = [\mathrm{u}_{\mathrm{pb1}} \quad \mathrm{u}_{\mathrm{pb2}}\ \mathrm{u}_{\mathrm{pb3}} \quad \mathrm{u}_{\mathrm{pb4}}]^{\mathrm{T}}$, as shown below:

$$V_s(x) = \frac{1}{2}x_1^2 + \frac{1}{2}x_2^2 + \frac{1}{2}x_3^2 + \frac{1}{2}x_4^2 \qquad (23)$$

By taking the derivative of (23) along (2) and reorganizing the following result is obtained:

$$\dot{V}_s(x) = \begin{bmatrix} ax_1^2 - x_1x_2x_3 \\ x_1x_2x_3 - bx_2^2 \\ cx_1x_2x_3 - dx_3^2 + gx_1x_3x_4 \\ kx_4^2 - hx_2x_4 \end{bmatrix} + y^T u_{pb} \qquad (24)$$

Therefore the following control law makes the closed loop system passive:

$$u_{pb} = \begin{bmatrix} -ax_1 + x_2x_3 \\ -x_1x_3 + bx_2 \\ -cx_1x_2 + dx_3 - gx_1x_4 \\ -kx_4 + hx_2 \end{bmatrix} + v \qquad (25)$$

Then, substituting (25) in $\dot{\mathrm{V}}_{\mathrm{s}}(\mathrm{x})$ given in (24) with y defined in (2):

$$\dot{V}_s(x) = y^T v \leq y^T v \qquad (26)$$

where the controller input v is selected as $\mathrm{v} = -[\mathrm{x}_1 \quad \mathrm{x}_2\ \mathrm{x}_3 \quad \mathrm{x}_4]^{\mathrm{T}}$. Then u_{pb} is given by (25) and can be substituted in the hybrid control law (3).

5. NUMERICAL EXAMPLES

In this section two numerical examples to evince the effectiveness of the proposed hybrid control strategy are shown in the following subsections.

5.1. Example 1: Hybrid Controller Strategy for the Chaotic Lorentz Attractor

The Lorentz attractor used in this example is (1) with initial conditions $\mathrm{X}(0) = [-8 \quad 8 \quad 27]^{\mathrm{T}}$. All the simulations were performed in MATLAB implementing the Runge-Kutta method to solve the chaotic and hyper-chaotic system.

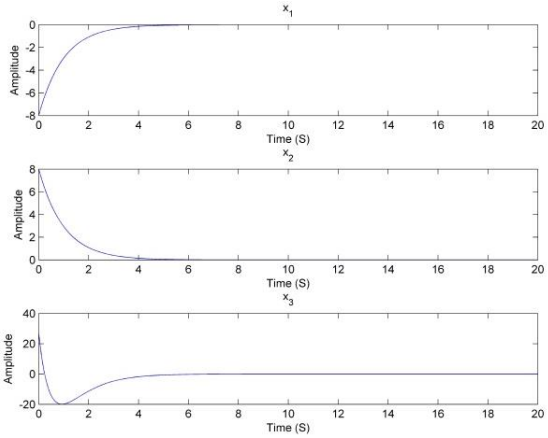

Fig. 7. State variables response of the Lorentz attractor

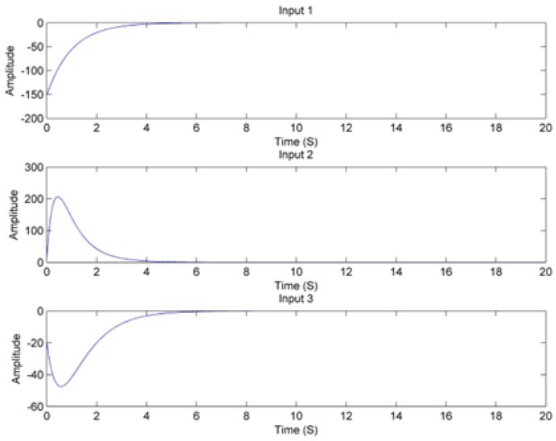

Fig. 8. Hybrid control inputs of the Lorentz attractor

In Fig. 7 the state variables of the Lorentz attractor are shown, where as it is noticed all the variables reach the origin proving that the system is stabilized by the proposed control law. With this example is corroborated numerically the theoretical results presented in the previous sections, so fuzzy type-2 and the passivity based hybrid technique is a suitable control strategy for different kinds of chaotic systems and not only for the Lorentz attractor analyzed in this article. In Fig. 8 the hybrid control input u for the Lorentz attractor are shown and as can be noticed the control effort of all inputs is significantly small, so the requirements of the controlled system are met.

DOI 10.1515/ama-2017-0015

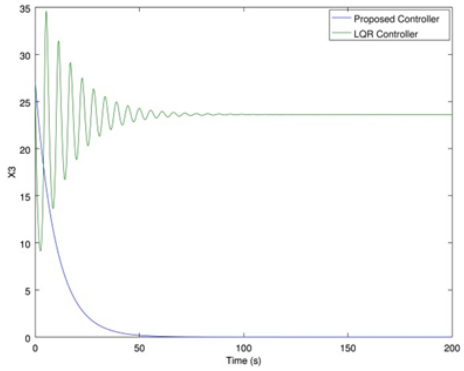

Fig. 9. Comparison between the proposed strategy and a linear quadratic regulator

In Fig. 9. a comparison between the proposed strategy and a linear quadratic regulator is shown and as can be noticed the response of the variable x_3 with the LQR strategy shows an oscillatory behaviour even when it stabilizes in other equilibrium point in comparison with the proposed control strategy, so the state variable response with the proposed approach is superior than the LQR strategy.

5.2. 5.2 Example 2: Proposed Hybrid Controller for the 4D Hyper-Chaotic System

In this subsection a numerical example implementing the hybrid controller to stabilizes the 4D hyper-chaotic system (2) is shown with initial conditions $X(0) = [-8 \quad 8\,27 \quad 0]^T$. In Fig. 10 the system response is shown, where as it is noticed all the variables reach the origin corroborating the theoretical results obtained in the previous sections. The hybrid fuzzy type-2 and passivity based control strategy is effective for the stabilization of any kind of hyper-chaotic systems of any dimension and not only the 4D hyper - chaotic system studied in this article.

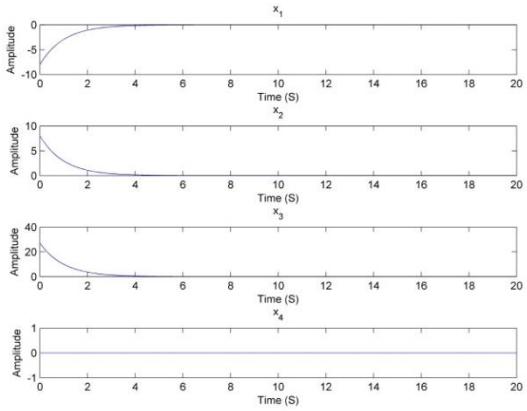

Fig. 10. State variables response of the 4D hyper-chaotic system

In Fig. 11 the hybrid control inputs of the 4D hyper-chaotic system are shown where as it is noticed the control effort for all the inputs is considerably small in order to stabilize the studied 4D hyper-chaotic system.

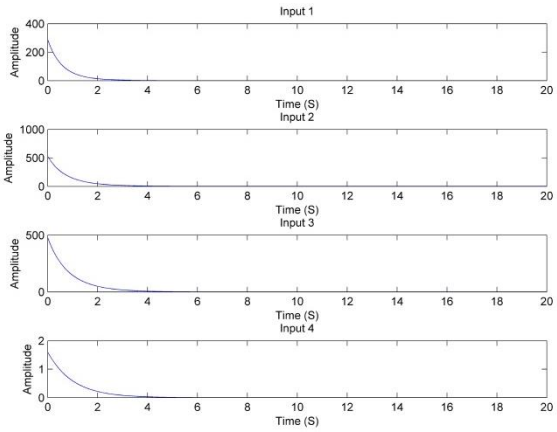

Fig. 11. Hybrid control inputs of the 4D hyper-chaotic system

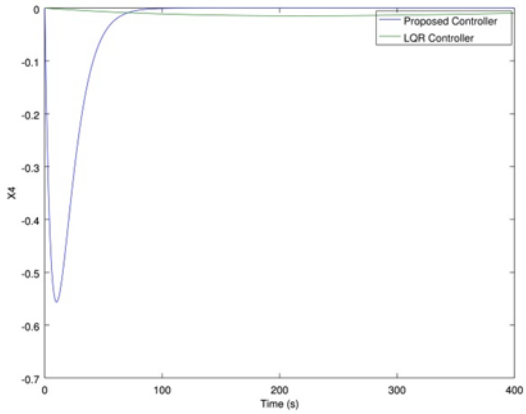

Fig. 12. Comparison between the proposed strategy and a linear quadratic regulator

Finally, in Fig. 12. a comparative analysis of the variable x_4 is shown where as can be noticed the response of this variable with the proposed control strategy in comparison with the LQR strategy is superior considering that this variable reaches the equilibrium point with no error instead of the convergence error of the variable response yielded by the LQR strategy.

6. DISCUSSION

According to the theoretical results obtained in this paper, it is proved that a hybrid fuzzy type-2 and passivity based control strategy is effective for the synchronization of chaotic and hyper-chaotic systems of different kinds. Due to the effectiveness of fuzzy type-2 controllers to deal with uncertainties and the capability of passivity based controllers to deal with the energy properties of nonlinear systems, a novel control strategy for chaotic and hyper-chaotic systems is developed to stabilize these kinds of systems independently of the initial conditions. Even when in this paper only 3D chaotic and 4D hyper-chaotic systems are considered, the proposed control strategy can be implemented for these kinds of systems of any dimension. The fuzzy type-2 membership functions and rules of this controller component can be easily obtained either by the expert knowledge or by any parameter adjustment methodology, such as genetic algorithms and particle swarm optimization, for example. The passivity based controller part is obtained by selecting an appropriate storage function in order to obtain the appropriate control law for the two kinds of

DOI 10.1515/ama-2017-0015

systems analyzed in this study. The passivity based and the fuzzy type-2 controller components are designed independently, due to the inference properties of fuzzy type-2 controller so the stability of chaotic and hyper-chaotic systems of any dimension are assured.

7. CONCLUSION

In this paper a hybrid fuzzy-type 2 and passivity based controller for the stabilization of chaotic and hyper-chaotic system is shown. Even when the two analyzed systems are a chaotic Lorentz attractor and a hyper-chaotic 4D systems, the proposed control strategy can be implemented satisfactorily in some kinds of chaotic and hyper-chaotic systems of any dimension. This study begins with the analysis of a chaotic Lorentz attractor and a hyper-chaotic 4D system, in which their stability properties such as eigenvalues and Lyapunov exponents are analyzed along with their bifurcation diagrams to find when both systems are in stability, chaotic or hyper-chaotic behaviour respectively. Then, a general fuzzy type-2 and passivity based controller approach for some kinds of chaotic and hyper-chaotic systems of any dimension is presented that can be used in several kinds of systems and not only the analyzed ones in this article.

The proposed control strategy is developed by an independent design of the two components of the controller, the MIMO fuzzy type-2 component and passivity-based component. The MIMO fuzzy type-2 controller part is designed considering the expert knowledge and exploiting the advantages of fuzzy type-2 systems such as noise rejection and the capability to deal with uncertainties and finally, the passivity based controller component is designed considering the energy properties of the two studied systems. Passivity based control is implemented due to its effectiveness and suitability to stabilize different kinds of nonlinear systems, and when it is implemented along with a fuzzy type-2 controller the performance of the controlled systems are improved including other advantages such as noise and disturbance rejection.

REFERENCES

1. **Castillo O., Melin P.** (2008), *Type-2 Fuzzy Logic: Theory and Applications*, Springer Verlag, Germany.
2. **Castillo O., Melin P.** (2014), A review on interval type-2 fuzzy logic applications in intelligent control, *Inf. Sciences*, 279, 615-631.
3. **Castillo O., Rico, D.** (2006), Intelligent control of dynamic systems using type-2 fuzzy logic and stasbility issues, *International Mathematical Forum*, 1(28), 1371-1382.
4. **Chen Z.-M., Djidjeli K., Price W.** (2006), Computing Lyapunov exponents based on the solution expression of the variational system, *Applied Mathematics and Computation*, 174(2), 982- 996.
5. **Dadras S., Momeni H.** (2013), Passivity-based fractional-order integral sliding-mode control design for uncertain fractional order nonlinear systems, *Mechatronics*, 23(7), 880-887.
6. **Dieci L., Vleck E.S.V.** (1995), Computation of a few Lyapunov exponents for continuous and discrete dynamical systems, *Applied Numerical Mathematics*, 17(3), 275-291.
7. **Effati S., Saberi-Nadjafi J., Saberi Nik H.** (2014), Optimal and adaptive control for a kind of 3D chaotic and 4D hyper- chaotic systems, *Applied Mathematical Modelling*, 38(2), 759-774.
8. **Fayek H., Elamvazuthi I., Perumal N., Venkatesh B.** (2014), A controller based on optimal type-2 fuzzy logic: Systematic design, optimization and real-time implementation, *ISA Transactions*, 53(5),1583-1591.
9. **Haddad W.M., Chellaboina V.** (2008), *Nonlinear dynamical systems and control a Lyapunov-based approach*, Princeton University Press, New Jersey, USA.
10. **Hagras, H.** (2004). A hierarchical type-2 fuzzy logic control architecture for autonomous mobile robots. Fuzzy Systems, IEEE Transactions on, Vol. 12, No. 4, 524-539.
11. **He D., Xu J., Chen Y., Tan, N.** (1999). A simple method for the computation of the conditional Lyapunov exponents, *Communications in Nonlinear Science and Numerical Simulation*, 4(2), 113-117.
12. **Kang H., Vachtsevanos G.** (1992), Adaptive fuzzy logic control, *Fuzzy Systems*, IEEE International Conference, 407-414.
13. **Karnik N., Mendel J., Liang Q.** (1999), Type-2 fuzzy logic systems, *Fuzzy Systems*, IEEE Transactions, 7(6), 643-658.
14. **Liu S., Sun J., Geng Z.** (2013), Passivity-based finite-time attitude control problem, *Control Conference (ASCC)*, 1-6.
15. **Martino F., Sessa S.** (2014), Type-2 interval fuzzy rule based systems in spatial analysis, *Information Sciences*, 279, 199-212.
16. **Mendel J.** (2005), On a 50 percent savings in the computation of the centroid of a symmetrical interval type-2 fuzzy set, *Information Sciences*, 172(3-4), 417-430.
17. **Mendel J.** (2007a), Advances in type-2 fuzzy sets and systems, *Information Sciences*, 177(1), 84-110.
18. **Mendel J.** (2007b), Type-2 fuzzy sets and systems: An overview, *Computational Intelligence Magazine*, IEEE, 2(1), 20-29.
19. **Mendel J., Wu H.** (2007), New results about the centroid of an interval type-2 fuzzy set, including the centroid of a fuzzy granule, *Information Sciences*, 177(2), 360-377.
20. **Morales-Mata I., Tang Y., Lopez M., Santillan S.** (2008), A design procedure of fuzzy PD control for mechanical systems, *Control and Decision Conference*, China, 5325-5330.
21. **Ontanon-Garcia L., Campos-Canton E.** (2013, Preservation of a two-wing Lorenz-like attractor with stable equilibria, *Journal of the Franklin Institute*, 350(10), 2867-2880.
22. **Protasov V., Jungers R. (2013),** Lower and upper bounds for the largest Lyapunov exponent of matrices, *Linear Algebra and its Applications*, 438 (11), 4448- 4468.
23. **Richter H.** (2003), Controlling chaos in maps with multiple strange attractors, *International Journal of Bifurcation and Chaos in Applied Sciences and Engineering*, 13(10), 3037-3051.
24. **Singh M., Gupta J.** (2007), A new algorithm basetype-2 fuzzy controller for diabetic patient, *Int. J. Biomedical Engineering and Technology*, 1(1), 19-40.
25. **Turksen I.** (1999), Type I and type II fuzzy system modeling, *Fuzzy Sets and Systems*, 106(1), 11-34.
26. **Wang Y.-F., Yu Z.-G.** (2011), A type-2 fuzzy method for identification of disease-related genes on microarrays, *International Journal of Bioscience, Biochemistry and Bioinformatics*, 1(1), 73-78.
27. **Yonemoto K., Yanagawa T.** (2007), Estimating the Lyapunov exponent from chaotic time series with dynamic noise, *Statistical Methodology*, 4(4), 461-480.
28. **Zhou P., Huang K.** (2014), A new 4-D non-equilibrium fractional-order chaotic system and its circuit implementation, *Communications in Nonlinear Science and Numerical Simulation*, 19(6), 2005-2011.
29. **Zhou S.-M., Garibaldi J., John R., Chiclana F.** (2009), On constructing parsimonious type-2 fuzzy logic systems via influential rule selection, *Fuzzy Systems*, IEEE Transactions, 17(3), 654–667.
30. **Zhu B., Huo W.** (2013), Passivity-based adaptive trajectory linearization control for a model-scaled unmanned helicopter, *Control Conference* (CCC), Chinese, 2879-2884.

Acknowledgment: This work was partially supported by the Spanish Ministry of Economy and Competitiveness under Grant DPI2015-64170-R/FEDER

DOI 10.1515/ama-2017-0016

BIAS DRIFT ESTIMATION FOR MEMS GYROSCOPE USED IN INERTIAL NAVIGATION

Radosław CECHOWICZ*

*Department of Automation, Faculty of Mechanical Engineering, Lublin University of Technology,
ul. Nadbystrzycka 36, 20-618 Lublin, Poland

r.cechowicz@pollub.pl

received 8 May 2016, revised 10 May 2017, accepted 15 May 2017

Abstract: MEMS gyroscopes can provide useful information for dead-reckoning navigation systems if suitable error compensation algorithm is applied. If there is information from other sources available, usually the Kalman filter is used for this task. This work focuses on improving the performance of the sensor if no other information is available and the integration error should be kept low during periods of still (no movement) operation. A filtering algorithm is proposed to follow bias change during sensor operation to reduce integration error and extend time between successive sensor calibrations. The advantage of the proposed solution is its low computational complexity which allows implementing it directly in the micro-controller of controlling the MEMS gyroscope. An intelligent sensor can be build this way, suitable for use in control systems for mobile platforms. Presented results of a simple experiment show the improvement of the angle estimation. During the 12 hours experiment with a common MEMS sensor and no thermal compensation, the maximum orientation angle error was below 8 degrees.

Key words: MEMS Gyroscope, Inertial Navigation, Mobile Platform, Bias Estimation, Angle Of Orientation, Filtering, Gauss Distribution

1. INTRODUCTION

One of the barriers to the development of mobile platforms designed to work in industrial halls and public buildings are the difficulties in identifying the position of the platform (in relation to the other elements of the environment/building). In the AGV systems operating in warehouses, this problem is usually solved by installing hardware (fixed) routes or way-points. Depending on the chosen technology, these paths can be marked with contrasting paint, magnetic stripe, inductive wires, or by surface modifications (guiding canals, kerbs, etc.). Orientation in space can then be kept by reading or counting route markings — for example bar codes, QR codes, RFID tokens, magnetic strips, etc. In some systems, the position of the moving object, in relation to fixed or passive beacons, can be determined by triangulation (Ijaz et al., 2013; Mautz, 2009). Selected industrial control systems for autonomous vehicles have been documented for example in Ganesharajah et al. (1988).

Such navigation systems share a common problem — the limited flexibility of the path forces users to follow fixed routes (or go over fixed way-points). In consequence, some space is reserved for the exclusive use of the transport system. Any change of the route can only be done by installing new markings and reserving new space for the AGV system (Herrero-Perez et al., 2014). Since all routes have to be marked, the infrastructure must cover the entire area where the automatic transport system is used.

If the autonomy of transport system users (mobile platforms) were increased by (partial or total) detaching them from permanently marked routes, it would allow:

- to increase the flexibility of the system allowing adjusting the transport routes to the dynamic change of the environment (e.g. the emergence of obstacles, temporary route closure, etc.).
- to reduce the number of fixed way-points decreasing the cost of the infrastructure.

Autonomous mobile platforms must be equipped with a navigation system that provides the ability to move independently in areas where the observation of way-points is not possible. There, the on-board controller must navigate using the data from the local sensors (dead-reckoning).

Partial autonomy of the mobile platform can be achieved using the existing technologies. For example, in Lee and Yang (2012) a Hall sensor was used to measure deviations from the trajectory while passing over magnetic way-points. Similarly, using QR codes and a camera mounted on the moving platform, the deviation from the track is measured in Kiva robots (Guizzo, 2008; Mountz, 2005). Local control system operating in these robots identifies the properties of the platform (like yaw factor) on the basis of measurements from multiple on-board sensors and the observation of fixed reference points. As a result, robots can move autonomously through the distance between reference points.

Authors of the article (Acosta Calderon et al., 2015) proposed a solution that allowed removing all hardware way-points. In this system, the platform "learns" the route at the time of the first run (which is done in manual control mode) by saving data from the on-board sensors. After that, the platform can follow the same route autonomously, using the previously collected data. To change the route, it is necessary to either guide the robot through the new path, or to download an existing map from the robot that had already followed it.

Similar solution, using data from encoders and from the laser scanner, is described in Herrero_Perez et al. (2013). The advantage of the solutions of this kind is that the platform is able to perform some operations without reference to the fixed infrastructure points. Thus, platform route can be easily adopted to the

DOI 10.1515/ama-2017-0016

current configuration of machines, pallets and obstacles in the hall.

Dead-reckoning navigation systems have been known and used for many years in maritime navigation, aviation and military. It can also be used to support the automotive GPS systems in areas where the signal is disrupted or unavailable (Enberg, 2015; Fang et al., 2005). Dead-reckoning is possible on the basis of data from inertial sensors – accelerometers and gyroscopes. Successful applications, make use mainly of high-quality gyroscopes, with low random noise and high durability. However, cheaper micro-electromechanical (MEMS) devices are increasingly popular. In Enberg (2015) it was shown that useful navigational information can be obtained by combining inertial sensors and incremental encoders.

Inertial sensors are used for navigating within buildings. One of the reported (Harle, 2013; Yuan and Chen, 2014; Zhang et al., 2013) applications is the use of an accelerometer and a gyroscope from the mobile phone to determine the position of the man inside the building. Position is calculated here by measuring the length and direction of steps. Detection of steps allows splitting the signal from sensors to small pieces, each a few seconds long (corresponding to a single step). This allows eliminating errors caused by the instability of inertial sensors and greatly improves the measurement. This works properly even with low-grade sensors (Scarlett, 2007). The system allows navigating in 3D, so it is possible to determine where and on which floor the owner of the phone is currently located (Fuchs et al., 2011), and use this information in a personalized guide or security system. A similar method was used in Gersdorf and Freese (2013), to estimate the position of a wheelchair using the signal from inertial sensors mounted on one of the wheels. The achieved accuracy of the measurement allowed practical use of the system. A similar system, described in Hedberg and Hammar (2015), was used to track the position of the train on the route between the stations.

2. RESEARCH PROBLEM

The problem shown here is a part of the larger project aiming to develop a hybrid navigation system for industrial mobile platforms working in a dynamic environment (typically inside a hall). Typical route of the mobile platform will consist of straight sections connected by arcs of small radius. The platform, equipped with a collision-preventing control system, will use dead-reckoning to navigate between scattered reference points. The reference points installed in the hall, will provide the way to accurately determine the position and orientation of the platform according to the fixed coordinate system. However, this will be possible only in a few selected areas. Inside the hall, the platform will move on a smooth, levelled surface, but it will have the ability to leave the hall and go on an outside lot where the surface will not be smooth (e.g. paved with cobbles).

A micro-electromechanical gyroscope mounted on the platform will be one of the elements of the navigation system. It will be used to measure the angle of rotation during turns, and to detect changes in the orientation of the platform caused by external factors (slip, user/operator actions, collisions with stationary or moving objects, etc.). The gyroscope system should be able to properly estimate the orientation of the platform between successive corrections made in the areas where the reference points were accessible for measurement. The time between successive adjustments is not fixed and can vary from a few seconds to several hours, depending on the type of task to be performed by the platform.

Because of the planned operating mode, the significant feature of the gyroscopic system should be the ability to maintain small orientation errors during longer stops outside the correction areas. It would allow to decrease the density of fixed position measurement points and enable the platform to go outside the platform to go outside the area of normal operation.

The research described in the article was conducted on a test rig consisting of a SCARA robot placed on a fixed platform.

2.1. Test Rig

The research described in the article was conducted on a test rig consisting of a SCARA robot placed on a fixed platform. MEMS sensor (gyroscope) was attached to the robot arm, as shown in Fig. 1 The robot arm was chosen instead of a mobile platform as it allowed to obtain accurate measurements of the actual angle of orientation and simulate driving on an arc of specified radius with precisely controlled angular velocity. The robot arm orientation was monitored during the tests with the rate of 10 measurements per second.

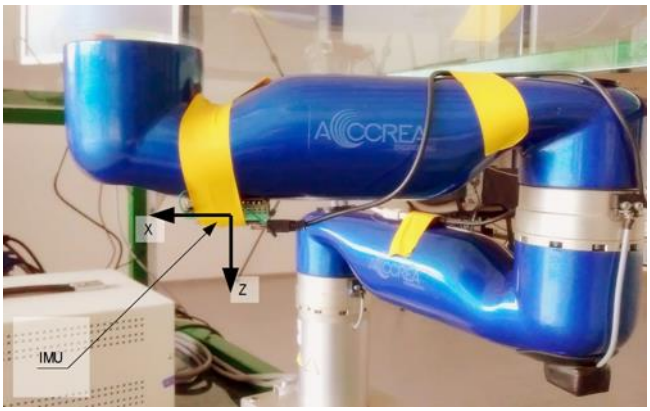

Fig. 1. The test rig with a gyroscopic sensor

2.2. The Gyroscope

The L3GD20H (ST Microelectronics) micro-electromechanical gyroscope was used during the tests. It is intended to be used in augmented reality, automation, robotics and navigation. The package comprises three gyroscopes measuring the rotational speed about axes of the Cartesian system. The basic technical data of the gyroscope are shown in Tab. 1.

Tab. 1. Basic technical data of the MEMS gyro (Fuchs et al., 2011)

Gyro range	+/-245dps	Resolution	0.00875dps/LSB
Zero rate bias	+/-25dps (@2000dps)	Rate noise density	0.011dps/$Hz^{1/2}$
Angle Random Walk	0.66$^{O}/h^{1/2}$	Digital output data rate	378.8Hz
Temperature sensitivity change	2%	Temp. zero rate change	+/-0.04dps/^{O}C

Data from all three axes will be used in the navigation system.

DOI 10.1515/ama-2017-0016

For the measurement of the angle of orientation of the platform moving on a horizontal surface, the most important information will come from the Z axis, perpendicular to the plane of movement. Further, in this article, the results connected to rotation about Z axis are presented.

2.3. Evaluation of the quality of the gyro sensor

The standard method for assessing the quality of the gyro is the Allan test (Institute of Electrical and Electronics Engineers, 2004). The test shall be carried out in a static state — gyroscope remains stationary for the duration of the test. Analysis of the recorded data allows determining natural variability of the sensor and evaluating the stability of the signal. The Allan variance method is used to compare the quality of the gyroscopes and to assess the nature of the signal disturbances. The methodology of the test is documented in Part C of the IEEE951 standard (Allan, 1966). Methods of testing and evaluation of oscillatory gyroscopes (MEMS) have been described in [24]], in the IEEE 1431 standard (Thielman et al., 2002), and in the IEC 62047-20.

The result of the Allan test for the Z axis gyro tested is shown in Fig. 2. The chart shows that the main source of noise in the range of sampling times from 0.01s to 100s is the angle random walk (ARW), which is approximately 0.011°/s/Hz$^{1/2}$. Stability of the bias for the axis Z is 3.58°/h. Based on these results, the gyroscope can be included in the class of industrial equipment. However, there is a spread of quality in MEMS gyroscopes. Even the units from the same housing can have different properties. For example, axes X and Y from the chip used in the tests had shown the ARW about 0.1dps/Hz$^{1/2}$. Measurements made on other units of the same type also gave different results.

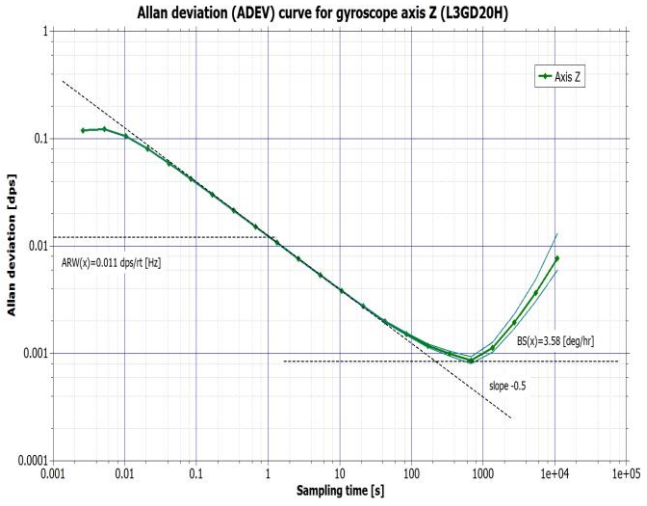

Fig. 2. Allan variance curve for the Z axis gyro L3GD20H

The instability of the bias and the angle random walk are the two main sources of gyroscope error. Both factors are random, and their effect usually limits the practical application of individual sensors to applications that do not require observation time (measurements) longer than a few seconds. Random processes occurring in MEMS gyroscopes limit their ability to detect low rotational speeds and make it difficult for the control systems to correctly interpret the signal under static conditions.

Identification of error sources and development of a model of the sensor may be one of the methods to achieve a system suitable for the practical use in navigation. The method is used mainly for high-end sensors, whose parameters are stable over time. In the case of MEMS, it is possible to develop a model (Enberg, 2015), but, as shown in Barett (2014), it does not always lead to a significant reduction in measurement error.

The mechanical properties of MEMS sensors can also be an important factor affecting the accuracy (Weinberg, 2011) of measurements. The measurements from a sensor with weak mechanical properties (e.g. with a tendency to resonate) exposed to vibrations may show much greater error than predicted in technical data sheets.

Improvement in accuracy can be obtained using the technique of associating data from several sensors (sensor fusion). Among the solutions described in the literature, the following can be cited: measuring the rotational speed by means of appropriately arranged accelerometers (Chatterjee et al., 2015), averaging measurement of several gyroscopes forming a matrix (Jiang et al., 2013), using the information about the state of the object to find the most likely estimate (Herrero-Perez et al., 2013; Romaniuk and Gosiewski, 2014).

Another method to improve the accuracy of the gyroscope may be tracking of the actual value of the bias. Since bias instability is one of main factors contributing to gyroscope error, finding a way to estimate it could improve the quality of angle estimation.. One of such approaches, using extended Kalman filter, is shown in Hyyti and Visala (2015).

2.4. Characteristics of the gyroscope signal

For an ideal gyro sensor, angular velocity w(t) of the platform at the moment t is proportional to the signal x(t) from the sensor after subtracting the bias $x_b(t)$:

$$\omega(t) = R\big(x(t) - x_b(t)\big) \tag{1}$$

where: R – coefficient of proportionality.

The expected value of the bias x_b is specified in the technical data (ZeroRateBias).

Tab. 2. Descriptive statistics for the gyro signal (sample length 6s)

Parameter	Measurement(X)	Parameter	Measurement(X)
Minimum value	-100	**Average x_{sr}**	**-52**
First quartile	-58	**Std. Deviation σ**	**11**
Median	-51	Skewness	0
Third quartile	-44	Kurtosis	4
Maximum value	-9		

The actual MEMS gyro signal is random. If the platform is stationary, and the recording time does not exceed a few dozen seconds, the signal from the MEMS gyro sensor can be approximated with a Gaussian distribution with the central value $x_{śr}$ and the deviation σ. The descriptive statistics of the 6s sample of the stationary gyroscope signal is shown in Tab. 2. Fig. 3 shows the histogram of this signal and the Gaussian distribution with parameters $w_{śr}$ and σ from Tab. 2. The random nature of the signal can

DOI 10.1515/ama-2017-0016

also be shown with the probability plot (Fig. 4) and the result of the Allan analysis (Fig. 2).

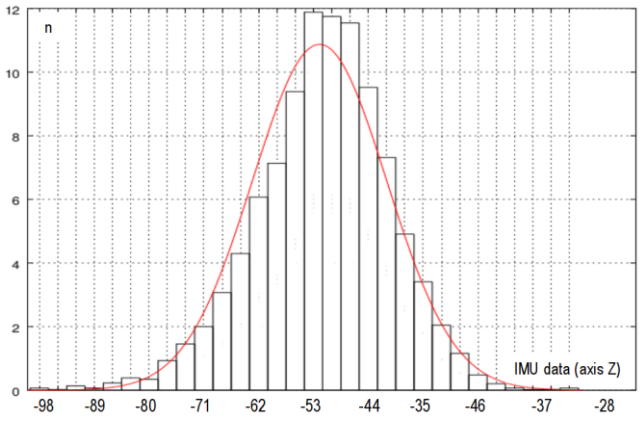

Fig. 3. A histogram signal from the Z axis gyro and a normal distribution with the parameters calculated from the measurements (Tab. 2)

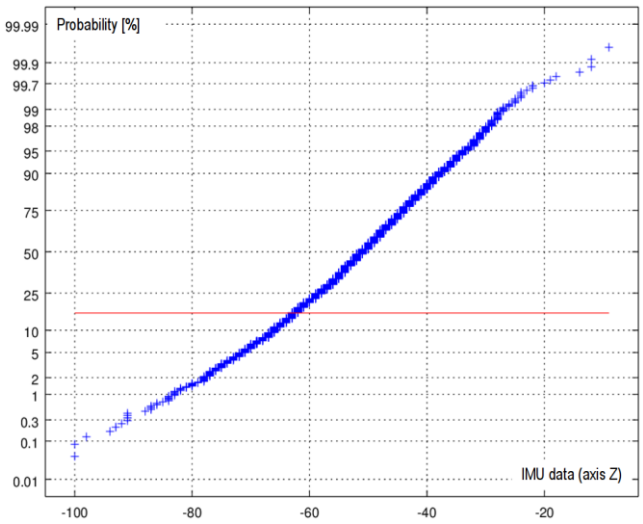

Fig. 4. Probability plot for the signal from the gyro Z-axis

The length of sampling time over which the central value of the Gaussian distribution can be computed, can be determined from the Allan variance curve. For the tested sensor that sampling time is from 0.1s to tens of seconds, since in this range the error from bias instability is not yet decisive.

The noise to signal ratio determines the accuracy of the rotational speed measurement. For the test sensor, the noise amplitude (6σ = 66) is only 0.2% of the measurement range. In applications where the rotational speed rather than orientation is measured (e.g. gesture detection), this accuracy is usually sufficient and this error can be ignored.

The average rotational speed of the platform during the period Δt_o can be determined from the formula:

$$\omega_{śr}(\Delta t_o) = R\left(x_{śr}(\Delta t_o) - x_b(\Delta t_o)\right) \tag{2}$$

If the platform remained still during this time that is if $\omega_{śr}(\Delta t_o) = 0$, then:

$$x_b(\Delta t_o) = x_{śr}(\Delta t_o) \tag{3}$$

The value of bias can therefore be found by computing the mean value of signal $x(t)$ at the time when the platform remains stationary. The maximum averaging time is limited by the bias instability and the working conditions of the navigation system (length and frequency of stops).

In Fig. 5 the signal from the gyro is divided into uniform segments of 3 seconds. Since the actual sampling frequency was 384Hz, there were 1,150 samples in each segment. Then, descriptive statistics was calculated for each segment, as in Tab. 2. On Fig. 5, there are shown: the average value in each segment, the standard deviation, the first and third quartile. Points which are outside the three quartile range (outliers) are marked with circles.

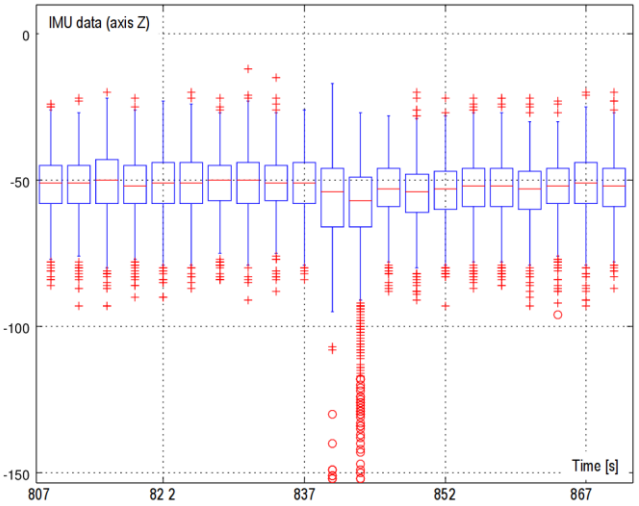

Fig. 5. Change of the gyro signal while in motion

In the middle of the time shown in Fig. 5 (the time from 840 to 846 seconds) the platform with a sensor made rotation of the angle Θ=220°, which lasted about 3 seconds. Two data segments which contain the rotation data are easy to distinguish from the rest. They have a significantly higher dispersion (range) and a slightly shifted average. The range of the segments is increased because the rotational speed of the platform, and the signal from the gyroscope changed proportionally. The range of the segments recorded during the constant speed motion will also be slightly larger than the stationary range due to unevenness of speed and an increased level of noise while driving (vibration, uneven ground etc.). The range of segments can therefore be used as a criterion for the selection of episodes in which the platform remained stationary.

The length of the segment (averaging time) will be primarily chosen with regard to technical reasons. Increasing the length of the segment up to several dozens of seconds, improves the sensitivity of the range criterion – it will then be possible to detect even small changes in the gyro signal (and low rotational speeds). However, this also extends the time required to register at least one segment representing pure stationary state, which may limit the usefulness of the system.

Bias (x_b) changes with time. This is the cause of the so-called "flow" or "drift" of the gyro readings which in some applications makes it necessary to periodically calibrate the gyro. The phenomenon of drift causes also a sharp increase in the orientation angle error, which is calculated by integrating the gyro signal over time. Since the MEMS gyroscopes exhibit relatively large drift they are usually not suitable for direct use in navigation.

Allan graph (Fig. 2) shows that the bias instability rate of the test sensor is dω_o=3.58°/h. In addition, temperature error of the

DOI 10.1515/ama-2017-0016

sensor may reach $d\omega_T$= + /- 0.005dps /^{O}C = + / - 18O/h/^{O}C. Even in stable operating conditions (temperature stabilization to 1^{O}C, no mechanical vibrations) it could mean that the orientation angle error after 1 hour observation will be greater than 20^O.

2.5. Estimation of the bias change

Let us suppose that at the moment t1 the angle of orientation of the platform was Θ_1.The angle of orientation of the platform Θ_n at the moment t_n is calculated by integrating the speed signal:

$$\Theta_n = \Theta_1 + \frac{1}{f_s}\sum_{i=1}^{n}\omega_z(t_i)\Theta_n = \Theta_1 + \frac{R}{f_s}\sum_{i=1}^{n}x(t_i) - x_b(t_i) \quad (4)$$

where: f_s – sampling rate (here 384Hz)

To determine the correct angle, it is necessary to know the value of the bias x_b.

Observing the signal of stationary gyroscope, one can notice that the speed of bias change is slow (at a rate of ten degrees per hour) compared to the change caused by rotation of a typical mobile platform (a few degrees per second). These two processes can be distinguished from each other by observing a signal from the sensor. To make this possible in a statistical sense, an assumption should be made that the nature of the distribution and the standard deviation of the signal generated by the stationary sensor remains unchanged over time (the natural process distribution does not change). Only the central value of the distribution x_{Wed} changes over time during the operation of the sensor.

Tracking the central value $x_{śr}$ (bias) changes is easy when the platform remains stationary. The problem is to find the correct value of bias when the platform is moving. As it is difficult to determine bias value while the platform is rotating, all segments recorded during the motion should be discarded using the range criterion.

In the experiment described below the following criterion was used to discard segments recorded during platform movement:

$$Rx < 7\sigma_{śr} \quad (5)$$

where: Rx – range of the segment, $\sigma_{śr}\sigma_{śr}$ – average standard deviation of the segments recorded in stationary conditions.

To detect slow changes in the average value (bias) and separate them from noise, a further selection step was proposed, wherein the average values of segments were compared against the moving average of some preceding segments. At this stage, all the segments with averages outside the typical area of variability were discarded. Typical area of variability of normal distribution is:

$$\Delta x = [x_{śr} - \sigma, x_{śr} + \sigma] \quad (6)$$

So, all the segments with average outside the limits were discarded:

$$x_{śr}(t_i) > \frac{1}{n}\sum_{i-n}^{i}x_{śr}(t_k) - \sigma_{śr}$$
$$x_{śr}(t_i) < \frac{1}{n}\sum_{i-n}^{i}x_{śr}(t_k) + \sigma_{śr} \quad (7)$$

where: $x_{śr}(t_i)$ $\sigma_{śr}$ mean value of the segment, n $\sigma_{śr}$ number of previously recorded segments to be used for the moving average. During the experiment, the value of *n* was chosen arbitrary.

2.6. Obtained results

Fig. 6 and Fig. 7 show the results of the experiment involving the measurement of the orientation angle of the platform rotating about 0.2 radians every 6 minutes. The experiment lasted 12 hours and its purpose was to check the stability of the MEMS gyroscope and to measure the orientation error. The platform was moving automatically, according to a pre-programmed sequence. The actual angle of orientation was measured with incremental encoders (with accuracy 0.01^O).

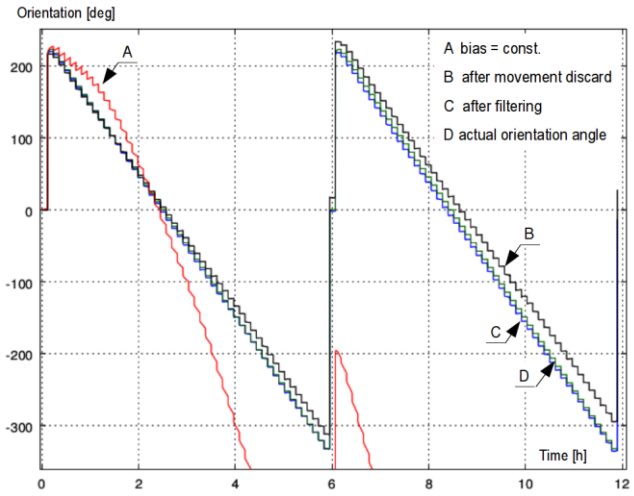

Fig. 6. The result of the experiment described in section 2.6

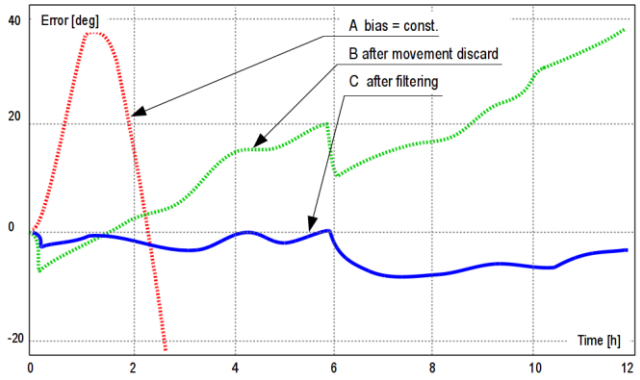

Fig. 7. Comparison of the angle of orientation errors

The angle of orientation has been determined by three different methods:

A – the bias xp appointed at the beginning of the experiment, remained unchanged for the rest of the time.

B – the bias was determined throughout the experiment, from segments remaining after the application of the criterion (6)

C – the bias was determined from the segments that met criteria (5) and (7).

The actual angle of orientation of the platform is marked in Fig. 6 with the letter D.

Orientation angle errors are shown in Fig. 7. Orientation error was obtained according to the formula:

$$E(t_i) = \Theta_a(t_i) - \Theta_x(t_i) \quad (8)$$

where: $E(t)$ – orientation error, $\Theta_a(t_i)$ – the actual orientation

DOI 10.1515/ama-2017-0016

angle of the platform at time t, $\theta_x(t_i)$ – orientation angle is determined from the signal of the gyroscope

In the case of the method A, the orientation error exceeded 20^O after a few minutes. Then, the absolute value of the angle grew at a rate of about 40^O per hour. The change of the direction of the error accumulation was due to thermal phenomena - the temperature of the gyro stabilized after about 4 hours after the experiment was started (the MEMS unit was mounted directly on a PCB, without any heat shield)

Using the range criterion (5) for segment selection and determining the offset value dynamically at standstill helped to reduce the rate error to about 5^O per hour. Due to the insufficient sensitivity of this method, the error is growing rapidly during the movements performed at low speed (mainly at final stages of the platform movement).

An additional selection criterion using the typical area of variability of the signal (7) allowed reducing the average rate of change of error to less than 1^O per hour. This method still has too low sensitivity to be able to detect low-speed movement but the improvement in performance is clearly visible.

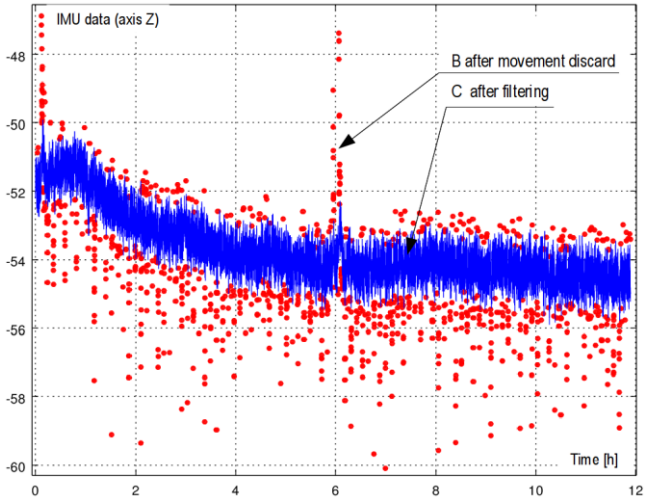

Fig. 8. Estimated bias value over time. The points rejected in the second selection phase are marked with red dots

Fig. 8 shows the estimated bias value during the experiment. Red dots mark the points that passed the first criterion (5). The blue line marks the points that additionally passed the criterion (7).

It is apparent (in Fig. 8) that the change of bias is not linear. The sensor temperature is one of the factors that greatly affect the measurement. It is difficult to identify and quantize the share of other factors.

3. CONCLUSION

The advantage of the described algorithm is its low computational complexity which allows implementing it directly in the micro-controller that provides communication with the MEMS gyroscope. An intelligent sensor can be build this way, suitable for use in control systems for mobile platforms, or other objects which do not rotate continuously.

During the experiment the thermal compensation of the gyroscope was not used. The method presented allows detecting any shifts of bias in the gyro signal - including those caused by the temperature change.

Two gyro sensors of the same type were used. In both cases, similar results were obtained.

A disadvantage of the proposed method is poor detection of low speed rotations. As a result, the sensor is not suitable for detecting deviation from the straight path or slow changes of the orientation of the platform. These must be detected by other methods.

An important limitation of the proposed method the necessity to stop the platform regularly in order to estimate the average value of the standstill signal and compute the current bias value. However, the typical work pattern of a warehouse robot or industrial AGV contains frequent stops for loading/unloading and maintenance operations so this should not be a problem.

Gyroscopes and all dead-reckoning systems work in incremental mode which is prone to error build-up over time. To extend the time between successive calibrations of the sensor, either a better sensor must be fitted or the measurement procedure must be improved.

Despite the drawbacks, the proposed method allows increasing the accuracy of the MEMS gyro sufficiently enough to use it as a secondary device for navigation in short distances.

Further research will focus on better detection of stationary state, possibly delegating some computational workload to a more powerful processor in the navigation control system.

REFERENCES

1. **Acosta Calderon C.A., Mohan E.R., Ng B.S.** (2015), Development of a hospital mobile platform for logistics tasks, *Digital Communications and Networks*, 1 (2), 102-111.
2. **Allan D.W.** (1966), Statistics of atomic frequency standards, *Proceedings of the IEEE*, 54 (2), 221-230.
3. **Barrett J.M.** (2014), *Analyzing and Modeling Low-Cost MEMS IMUs for use in an Inertial Navigation System*, Worcester Polytechnic Institute.
4. **Chatterjee G., Latorre L., Mailly F., Nouet P., Hachelef N., Oueda C.** (2015), Smart-MEMS based inertial measurement units: gyro-free approach to improve the grade, *Microsystem Technologies*, 1-10
5. **Enberg D.** (2015), Performance Evaluation of Short Time Dead Reckoning for Navigation of an Autonomous Vehicle, Department of Electrical Engineering, Linköpings universitet
6. **Fang L., Antsaklis P.J., Montestruque L.A., McMickell M.B., Lemmon M., Sun Y., Fang H., Koutroulis I., Haenggi M., Xie M., Xie X.** (2005) Design of a wireless assisted pedestrian dead reckoning system - the NavMote experience, *IEEE Trans Instrum Meas,* 54, 2342-2358.
7. **Ferraina M.** (2015), L3GD20H: 3-axis digital output gyroscope, STMicroelectronics, DocID026442 Rev 2
8. **Fuchs C., Aschenbruck N., Martini P., Wieneke M** (2011), Indoor tracking for mission critical scenarios: A survey, *Pervasive and Mobile Computing*, 7 (1), 1-15.
9. **Ganesharajah T., Hall N.G., Sriskandarajah C.** (1988), Design and operational issues in AGV-served manufacturing systems, *Annals of Operations Research*, 76 (0), 109-154.
10. **Gersdorf B., Freese U.** (2013), A Kalman Filter for Odometry using a Wheel Mounted Inertial Sensor, *ICINCO*, 1, 388-395.
11. **Guizzo E.** (2008), Three Engineers, Hundreds of Robots, One Warehouse, *IEEE Spectrum*, 45(7), 26-34.
12. **Harle R.** (2013), A Survey of Indoor Inertial Positioning Systems for Pedestrians, *IEEE Communications Surveys & Tutorials*, 15(3), 1281-1293.
13. **Hedberg E., Hammar M.** (2015), Train Localization and Speed Estimation Using On-Board Inertial and Magnetic Sensors, Department of Electrical Engineering, Linköpings universitet

DOI 10.1515/ama-2017-0016

14. **Herrero-Perez D., Jose J., Martinez-Barbera H.** (2013), An Accurate and Robust Flexible Guidance System for Indoor Industrial Environments, *International Journal of Advanced Robotic Systems*, 10 (1), 1-9
15. **Hyyti H., Visala A.** (2015), A DCM Based Attitude Estimation Algorithm for Low-Cost MEMS IMUs, *International Journal of Navigation & Observation*, 2015, 1–18.
16. **Ijaz F., Yang H.K., Ahmad A.W., Lee C.** (2013), Indoor positioning: A review of indoor ultrasonic positioning systems, *Advanced Communication Technology (ICACT), 2013 15th International Conference*, 1146-1150.
17. **Institute of Electrical and Electronics Engineers** (2004), *IEEE standard specification format guide and test procedure for coriolis vibratory gyros*, Institute of Electrical and Electronics Engineers, New York.
18. **Jiang C., Xue L., Chang H., Yuan W.** (2012), Signal Processing of MEMS Gyroscope Arrays to Improve Accuracy Using a 1st Order Markov for Rate Signal Modeling, *Sensors*, 12(12), 172-1737.
19. **Lee S.-Y., Yang H.-W.** (2012), Navigation of automated guided vehicles using magnet spot guidance method, *Robotics and Computer-Integrated Manufacturing*, 28(3), 425-436.
20. **Mautz R.** (2009), Overview of current indoor positioning systems, *Geodesy and Cartography*, 35(1), 18-22.
21. **Mountz M.C.** (2005), Material handling system and method using mobile autonomous inventory trays and peer-to-peer communications, US/6950722
22. **Romaniuk S. Gosiewski Z.** (2014), Kalman Filter Realization for Orientation and Position Estimation on Dedicated Processor, *Acta Mechanica et Automatica*, 8(2), 88-94
23. **Scarlett J.** (2007), Enhancing the performance of pedometers using a single accelerometer, *Application Note, Analog Devices*, AN-900
24. **STMicroelectronics** (2013), *MEMS motion sensor: three-axis digital output gyroscope L3GD20H Datasheet*.
25. **Thielman L.O., Bennett S., Barker C.H., Ash M.E.** (2002), Proposed IEEE Coriolis Vibratory Gyro standard and other inertial sensor standards, *Position Location and Navigation Symposium, 2002 IEEE*, 351-358.
26. **Weinberg H.** (2011), Gyro mechanical performance: The most important parameter, *Technical Article* MS-2158, Analog Devices
27. **Yuan Q., Chen I.-M.** (2014), Localization and velocity tracking of human via 3 IMU sensors, *Sensors & Actuators: A. Physical*, 212, 25-33.
28. **Zhang R., Bannoura A., Hoflinger F., Reindl L.M., Schindelhauer C.** (2013), Indoor localization using a smart phone, *Sensors Applications Symposium (SAS), 2013 IEEE*, 38–42.

DE GRUYTER
OPEN

DOI 10.1515/ama-2017-0017 acta mechanica et automatica, vol.11 no.2 (2017)

FRICTIONAL HEATING WITH TIME-DEPENDENT SPECIFIC POWER OF FRICTION

Katarzyna TOPCZEWSKA*

*Faculty of Mechanical Engineering, Department of Mechanics and Applied Computer Science, Bialystok University of Technology, ul. Wiejska 45C, Bialystok 15–351, Poland

k.topczewska@doktoranci.pb.edu.pl

received 25 October 2016, revised 11 May 2017, accepted 15 May 2017

Abstract: In this paper analytical solutions of the thermal problems of friction were received. The appropriate boundary-value problems of heat conduction were formulated and solved for a homogeneous semi–space (a brake disc) heated on its free surface by frictional heat fluxes with different and time-dependent intensities. Solutions were obtained in dimensionless form using Duhamel's theorem. Based on received solutions, evolution and spatial distribution of the dimensionless temperature were analyzed using numerical methods. The numerical results allowed to determine influence of the time distribution of friction power on the spatio-temporal temperature distribution in brake disc.

Key words: Brake Disc, Frictional Heating, Temperature, Time-Dependent Power of Friction

1. INTRODUCTION

Frictional characteristics and wear in an disc-pad contact area are changing significantly depending on the way of absorbed heat energy by a braking system. In some cases the major part of braking work is accomplished in the initial stage of braking, in other cases work is more evenly distributed in time. Essential influence on value and evolution of the temperature has the nature of change with time the specific power of friction. Classification of the time courses of specific power of friction during single braking was proposed in monograph (Chichinadze, 1967). Table 5.3 on page 78 in this study contains eleven different functions, which describe change of the specific power of friction with braking time. Analysis of the influence of the each time course on the temperature were conducted based on, received by author solution to the one-dimensional thermal problem of friction for semi-space. However, these solutions were found with simplifying assumptions, which refer to interior points of the half-space on the axis perpendicular to the outer surface. It was assumed that, the temperature is proportional to the braking time and the temperature increments and also the average volumetric temperature are equal. The studies reviews of accurate (without mentioned above simplifications) solutions to the one-dimensional thermal problems of friction are in monographs (Jewtuszenko et al., 2014, Kuciej, 2012). They demonstrate that the vast majority of the received accurate solutions usually concern only two elementary cases from the above mentioned table. In first of them, specific power of friction in the braking process has constant value, in second it decreases linearly from maximum value in the initial moment to zero in the standstill. The second time course of specific power of friction is realizable during braking with constant deceleration and an immediate increase of pressure to nominal value in the initial time moment. Influence of the time of the contact pressure increase to nominal value on the temperature distribution was investigated in the article (Topczewska, 2016).

In this study the following simplification was adopted: a brake disc was replaced by homogeneous semi-space and the friction process of contacting bodies was replaced by heating process on outer surface by heat flux with given intensity (Evtushenko et al., 2007, Matysiak et al., 2007, Yevtushenko et al., 2005–2007, 2009–2012, 2014). Assuming one-dimensional direction of heat conduction is correct for high values of the Peclet number (for high velocity of braking). Taking into account mentioned above assumptions, analytical solutions to the one-dimensional thermal problems of friction for three time courses of specific power of friction (VI, VIII and XI positions in table 5.3 in monograph (Chichinadze, 1967)) were determined analytically. They reflect braking modes until the vehicle standstill.

2. STATEMENT OF THE PROBLEM

A considered semi–space orientation is given relative to a Cartesian frame of reference Oxyz with origin placed on the free surface (z-axis is vertical to this plane). The half-space $\mathrm{z} \geq 0$ is heated on its outer surface $\mathrm{z} = 0$ by heat flux with time-dependent $0 < \mathrm{t} < \mathrm{t_s}$ intensity $\mathrm{q_i(t)} = \mathrm{q_0 q_i^*(t)}, \mathrm{i} = 1,2,3$ (Fig. 1). Intensity of heat fluxes is proportional to the specific power of friction (Ling, 1973). Therefore, omitting constant proportional factor, the so-called heat partition ratio, the following three dimensionless time courses of friction power (Chichinadze, 1967):

$$q_1^*(t) = 3\left(1 - \frac{t}{t_s}\right)^2,\ q_2^*(t) = 6\frac{t}{t_s}\left(1 - \frac{t}{t_s}\right),$$
$$q_3^*(t) = 6\left(\sqrt{\frac{t}{t_s}} - \frac{t}{t_s}\right), \qquad 0 \leq t \leq t_s. \tag{1}$$

were considered.

Functions (1) are selected such that, the following braking work density:

DOI 10.1515/ama-2017-0017

$$w_i(t) = \int_0^t q_i(s)ds,\ 0 \le t \le t_s, i = 1,2,3, \quad (2)$$

in moment of standstill is constant and equal to $\mathrm{w_i(t_s)} = \mathrm{q_0 t_s}$. Graphs of dimensionless braking work density evolutions $\mathrm{w_i^*(t)} = \mathrm{w_i(t)/(q_0 t_s)}$ were presented in Fig. 2.

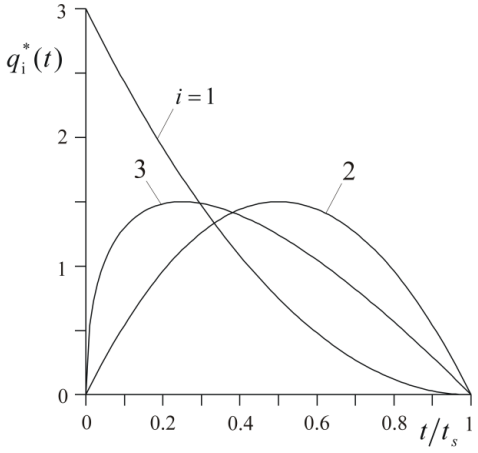

Fig. 1. The time courses of the dimensionless specific power of friction $q_i^*(t),\ i = 1,2,3$ (Abramowitz and Stegun, 1972)

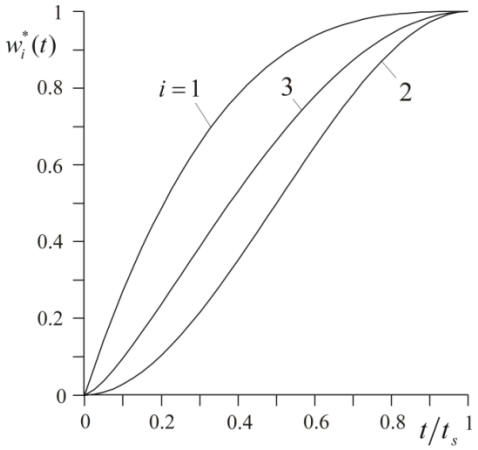

Fig. 2. The time courses of the total dimensionless braking work density $w_i^*(t), i = 1,2,3$ (Carlslaw and Jaeger, 1959)

Distributions of the one-dimensional transient dimensionless temperature fields $\mathrm{T_i^*(\zeta, t)},\ \mathrm{i} = 1,2,3$ in semi-space were found from solution to the following boundary-value problem of heat conduction, formulated in dimensionless form:

$$\frac{\partial^2 T_i^*(\zeta,\tau)}{\partial \zeta^2} = \frac{\partial T_i^*(\zeta,\tau)}{\partial \tau}, \zeta \ge 0, 0 \le \tau \le \tau_s. \quad (3)$$

$$\left.\frac{\partial T_i^*(\zeta,\tau)}{\partial \zeta}\right|_{\zeta=0} = -\,q_i^*(\tau),\ i = 1,2,3, 0 \le \tau \le \tau_s, \quad (4)$$

$$T_i^*(\zeta,\tau) \to 0, \zeta \to \infty, 0 \le \tau \le \tau_s, \quad (5)$$

$$T_i^*(\zeta,0) = 0, \zeta \ge 0, \quad (6)$$

where

$$\zeta = \frac{z}{a}, \tau = \frac{kt}{a^2}, \tau_s = \frac{kt_s}{a^2}, T_0 = \frac{q_0 a}{K}, T_i^* = \frac{T_i - T_a}{T_0}, \quad (7)$$

$\mathrm{a} = \sqrt{3\mathrm{kt_s}}$ is effective depth of the heat penetration inside brake disc (Chichinadze, et al., 1979), $\mathrm{T_a}$ is initial temperature, K, k are thermal conductivity and thermal diffusivity, respectively.

3. SOLUTION OF THE PROBLEM

Solutions to the boundary-value problem (3)–(6) were found based on Duhamel's theorem (Ozisik,1993):

$$T_i^*(\zeta,\tau) = \int_0^t q_i^*(s)\frac{\partial}{\partial \tau}T^{*(0)}(\zeta,\tau - s)ds,\ \zeta \ge 0, 0 \le \tau \le \tau_s, \quad (8)$$

where (Carslaw H. S. et al. 1959):

$$T^{*(0)}(\zeta,\tau) = 2\sqrt{\tau}\,\mathrm{ierfc}\left(\frac{\zeta}{2\sqrt{\tau}}\right), \zeta \ge 0, 0 \le \tau \le \tau_s, \quad (9)$$

is solution to the problem (3)–(6) with constant in time $q^*(\tau) = 1$ intensity of heat flux in boundary condition (4).

Taking into account value of the following derivative of the complementary error function (Abramowitz M. et al. 1972):

$$\frac{\partial}{\partial x}\mathrm{erfc}(x) = -\frac{2x}{\sqrt{\pi}}e^{-x^2}, \quad (10)$$

the following partial derivative was counted:

$$\frac{\partial}{\partial \tau}\left[2\sqrt{\tau - s}\ \mathrm{ierfc}\left(\frac{\zeta}{2\sqrt{\tau - s}}\right)\right] = \frac{e^{-\left(\frac{\zeta}{2\sqrt{\tau-s}}\right)^2}}{\sqrt{\pi(\tau - s)}}. \quad (11)$$

Substituting relation (9) and derivative (11) to the formula (8), we received:

$$T_1^*(\zeta,\tau) = 3\int_0^\tau \left(1 - \frac{s}{\tau_s}\right)^2 \frac{e^{-\left(\frac{\zeta}{2\sqrt{\tau-s}}\right)^2}}{\sqrt{\pi(\tau - s)}}ds, \zeta \ge 0, 0 \le \tau \le \tau_s, \quad (12)$$

$$T_2^*(\zeta,\tau) = 6\int_0^\tau \left[\frac{s}{\tau_s} - \left(\frac{s}{\tau_s}\right)^2\right] \frac{e^{-\left(\frac{\zeta}{2\sqrt{\tau-s}}\right)^2}}{\sqrt{\pi(\tau - s)}}ds, \zeta \ge 0, 0 \le \tau \le \tau_s, \quad (13)$$

$$T_3^*(\zeta,\tau) = 6\int_0^\tau \left(\sqrt{\frac{s}{\tau_s}} - \frac{s}{\tau_s}\right) \frac{e^{-\left(\frac{\zeta}{2\sqrt{\tau-s}}\right)^2}}{\sqrt{\pi(\tau - s)}}ds, \zeta \ge 0, 0 \le \tau \le \tau_s. \quad (14)$$

Above equations (12)–(14) were written as difference integrals:

$$T_1^*(\zeta,\tau) = 3[I_0(\zeta,\tau) - I_2(\zeta,\tau)], \zeta \ge 0, 0 \le \tau \le \tau_s, \quad (15)$$

$$T_2^*(\zeta,\tau) = 6[I_1(\zeta,\tau) - I_2(\zeta,\tau)], \zeta \ge 0, 0 \le \tau \le \tau_s, \quad (16)$$

$$T_3^*(\zeta,\tau) = 6\left[I_{1/2}(\zeta,\tau) - I_1(\zeta,\tau)\right], \zeta \ge 0, 0 \le \tau \le \tau_s, \quad (17)$$

where

$$I_0(\zeta,\tau) = \frac{1}{\sqrt{\pi}}\int_0^\tau \frac{1}{\sqrt{\tau - s}} e^{-\left(\frac{\zeta}{2\sqrt{\tau-s}}\right)^2} ds, \quad (18)$$

$$I_1(\zeta,\tau) = \frac{2}{\tau_s\sqrt{\pi}}\int_0^\tau \frac{s}{\sqrt{\tau - s}} e^{-\left(\frac{\zeta}{2\sqrt{\tau-s}}\right)^2} ds, \quad (19)$$

$$I_2(\zeta,\tau) = \frac{1}{\tau_s^2\sqrt{\pi}}\int_0^\tau \frac{s^2}{\sqrt{\tau - s}} e^{-\left(\frac{\zeta}{2\sqrt{\tau-s}}\right)^2} ds, \quad (20)$$

$$I_{1/2}(\zeta,\tau) = \frac{1}{\sqrt{\tau_s\pi}}\int_0^\tau \sqrt{\frac{s}{\tau - s}} e^{-\left(\frac{\zeta}{2\sqrt{\tau-s}}\right)^2} ds. \quad (21)$$

Using substitution $x = 1/\sqrt{\tau - s}$, the integrals (18)–(21) were designated:

$$I_0(\zeta,\tau) = \frac{2}{\sqrt{\pi}}L_2(\zeta,\tau), \quad (22)$$

$$I_1(\zeta,\tau) = \frac{2}{\tau_s\sqrt{\pi}}[\tau L_2(\zeta,\tau) - L_4(\zeta,\tau)], \quad (23)$$

$$I_2(\zeta,\tau) = \frac{2}{\tau_s^2\sqrt{\pi}}[\tau^2 L_2(\zeta,\tau) - 2\tau L_4(\zeta,\tau) + L_6(\zeta,\tau)], \quad (24)$$

where

$$L_k(\zeta,\tau)=\int_{\frac{1}{\sqrt{\tau}}}^{\infty} e^{-\left(\frac{\zeta}{2}\right)^2 x^2}\frac{dx}{x^k}, k=2,4,6. \quad (25)$$

Based on recurrence relation (Prudnikov et al., 1986):

$$\int \frac{e^{-(ax)^2}}{x^n}dx=-\frac{e^{-(ax)^2}}{(n-1)x^{n-1}}-\frac{2a^2}{n-1}\int\frac{e^{-(ax)^2}}{x^{n-2}}dx,\ a>0,$$

$$n=2,3,\ldots, \quad (26)$$

and the following solution (Prudnikov et al., 1986):

$$L_2(\zeta,\tau)=\sqrt{\pi\tau}\,\mathrm{ierfc}\left(\frac{\zeta}{2\sqrt{\tau}}\right), \quad (27)$$

we achieved:

$$L_4(\zeta,\tau)=\frac{\tau\sqrt{\pi\tau}}{3}\left\{\left[1-2\left(\frac{\zeta}{2\sqrt{\tau}}\right)^2\right]\mathrm{ierfc}\left(\frac{\zeta}{2\sqrt{\tau}}\right)+\frac{\zeta}{2\sqrt{\tau}}\mathrm{erfc}\left(\frac{\zeta}{2\sqrt{\tau}}\right)\right\}, \quad (28)$$

$$L_6(\zeta,\tau)=\frac{\tau^2\sqrt{\pi\tau}}{5}\left\langle\left\{1-\frac{2}{3}\left(\frac{\zeta}{2\sqrt{\tau}}\right)^2\left[1-2\left(\frac{\zeta}{2\sqrt{\tau}}\right)^2\right]\right\}\mathrm{ierfc}\left(\frac{\zeta}{2\sqrt{\tau}}\right)+\right.$$
$$\left.+\frac{\zeta}{2\sqrt{\tau}}\mathrm{erfc}\left(\frac{\zeta}{2\sqrt{\tau}}\right)\left[1-\frac{2}{3}\left(\frac{\zeta}{2\sqrt{\tau}}\right)^2\right]\right\rangle. \quad (29)$$

Taking into account results (27)–(29) in equations (22)–(24), we obtain:

$$I_0(\zeta,\tau)=2\sqrt{\tau}\,\mathrm{ierfc}\left(\frac{\zeta}{2\sqrt{\tau}}\right), \quad (30)$$

$$I_1(\zeta,\tau)=\frac{2\tau\sqrt{\tau}}{3\tau_s}\left\{2\left[1+\left(\frac{\zeta}{2\sqrt{\tau}}\right)^2\right]\mathrm{ierfc}\left(\frac{\zeta}{2\sqrt{\tau}}\right)+\frac{\zeta}{2\sqrt{\tau}}\mathrm{erfc}\left(\frac{\zeta}{2\sqrt{\tau}}\right)\right\}, \quad (31)$$

$$I_2(\zeta,\tau)=\frac{2\sqrt{\tau}}{15}\left(\frac{\tau}{\tau_s}\right)^2\left\{\left[8+18\left(\frac{\zeta}{2\sqrt{\tau}}\right)^2+4\left(\frac{\zeta}{2\sqrt{\tau}}\right)^4\right]\mathrm{ierfc}\left(\frac{\zeta}{2\sqrt{\tau}}\right)-\right.$$
$$\left.-\frac{\zeta}{2\sqrt{\tau}}\mathrm{erfc}\left(\frac{\zeta}{2\sqrt{\tau}}\right)\right\}. \quad (32)$$

Subsequently integral (21) will be counted. Using the same substitution $x=1/\sqrt{\tau-s}$, we have:

$$I_{1/2}(\zeta,\tau)=\sqrt{\frac{\tau}{\tau_s\pi}}\,J(\zeta,\tau), \quad (33)$$

where

$$J(\zeta,\tau)=\int_{\frac{1}{\sqrt{\tau}}}^{\infty}\sqrt{x-\frac{1}{\tau}}\,e^{-\left(\frac{\zeta}{2}\right)^2 x}\frac{dx}{x^2}. \quad (34)$$

Integrating (34) by parts, we have:

$$J(\zeta,\tau)=\frac{1}{2}J_1(\zeta,\tau)-\frac{\zeta^2}{4}J_2(\zeta,\tau), \quad (35)$$

where

$$J_1(\zeta,\tau)=\int_{\frac{1}{\sqrt{\tau}}}^{\infty}\frac{1}{\sqrt{x-\tau^{-1}}}e^{-\left(\frac{\zeta}{2}\right)^2 x}\frac{dx}{x}, \quad (36)$$

$$J_2(\zeta,\tau)=\int_{\frac{1}{\sqrt{\tau}}}^{\infty}\sqrt{x-\tau^{-1}}\,e^{-\left(\frac{\zeta}{2}\right)^2 x}\frac{dx}{x}. \quad (37)$$

Based on the following formula (Prudnikov et al., 1998):

$$\int_u^{\infty}\frac{(x-u)^{\nu}e^{-\mu x}}{x}dx=u^{\nu}\Gamma(\nu+1)\Gamma(-\nu,u\mu),$$

$$u>0,\mathrm{Re}\nu>-1,\mathrm{Re}\mu>0, \quad (38)$$

functions (36) and (37) were written in the forms:

$$J_1(\zeta,\tau)=\sqrt{\tau}\,\Gamma\left(\frac{1}{2}\right)\Gamma\left(\frac{1}{2},\frac{\zeta^2}{4\tau}\right), \quad (39)$$

$$J_2(\zeta,\tau)=\frac{1}{\sqrt{\tau}}\Gamma\left(\frac{3}{2}\right)\Gamma\left(-\frac{1}{2},\frac{\zeta^2}{4\tau}\right). \quad (40)$$

Taking into account relation (Prudnikov et al., 1998):

$$\Gamma(\nu+1,z)=\nu\Gamma(\nu,z)+z^{\nu}e^{-z}, \quad (41)$$

we receive:

$$\Gamma\left(-\frac{1}{2},\frac{\zeta^2}{4\tau}\right)=2\sqrt{\pi}\left(\frac{\zeta}{2\sqrt{\tau}}\right)^{-1}\mathrm{ierfc}\left(\frac{\zeta}{2\sqrt{\tau}}\right). \quad (42)$$

In regard to the following (Prudnikov et al., 1998):

$$\Gamma\left(\frac{1}{2}\right)=\sqrt{\pi},\ \Gamma\left(\frac{3}{2}\right)=\frac{\sqrt{\pi}}{2},\ \Gamma\left(\frac{1}{2},\frac{\zeta^2}{4\tau}\right)=\sqrt{\pi}\mathrm{erfc}\left(\frac{\zeta}{2\sqrt{\tau}}\right), \quad (43)$$

and (42), we can write:

$$J_1(\zeta,\tau)=\pi\sqrt{\tau}\,\mathrm{erfc}\left(\frac{\zeta}{2\sqrt{\tau}}\right), \quad (44)$$

$$J_2(\zeta,\tau)=\frac{\pi}{\sqrt{\tau}}\left(\frac{\zeta}{2\sqrt{\tau}}\right)^{-1}\mathrm{ierfc}\left(\frac{\zeta}{2\sqrt{\tau}}\right). \quad (45)$$

Using solutions (44) and (45), we write (35) in form:

$$J(\zeta,\tau)=\frac{\pi\sqrt{\tau}}{2}\left[\mathrm{erfc}\left(\frac{\zeta}{2\sqrt{\tau}}\right)-2\left(\frac{\zeta}{2\sqrt{\tau}}\right)\mathrm{ierfc}\left(\frac{\zeta}{2\sqrt{\tau}}\right)\right], \quad (46)$$

Substituting above formula to equation (33), we receive:

$$I_{1/2}(\zeta,\tau)=\frac{\tau}{2}\sqrt{\frac{\pi}{\tau_s}}\left[\mathrm{erfc}\left(\frac{\zeta}{2\sqrt{\tau}}\right)-\frac{\zeta}{\sqrt{\tau}}\mathrm{ierfc}\left(\frac{\zeta}{2\sqrt{\tau}}\right)\right]. \quad (47)$$

Having regard relations (30)–(32) and (47) we determine searched temperature fields from (15)–(17):

$$T_1^*(\zeta,\tau)=2\sqrt{\tau}\left\langle\frac{1}{5}\left(\frac{\tau}{\tau_s}\right)^2\left[8+18\left(\frac{\zeta}{2\sqrt{\tau}}\right)^2+4\left(\frac{\zeta}{2\sqrt{\tau}}\right)^4\right]\mathrm{ierfc}\left(\frac{\zeta}{2\sqrt{\tau}}\right)-\right.$$
$$-\left[7+2\left(\frac{\zeta}{2\sqrt{\tau}}\right)^2\right]\frac{\zeta}{2\sqrt{\tau}}\mathrm{erfc}\left(\frac{\zeta}{2\sqrt{\tau}}\right)+3\mathrm{ierfc}\left(\frac{\zeta}{2\sqrt{\tau}}\right)-\frac{2\tau}{\tau_s}\left\{2\left[1+\right.\right.$$
$$\left.\left.+\left(\frac{\zeta}{2\sqrt{\tau}}\right)^2\right]\mathrm{ierfc}\left(\frac{\zeta}{2\sqrt{\tau}}\right)+\frac{\zeta}{2\sqrt{\tau}}\mathrm{erfc}\left(\frac{\zeta}{2\sqrt{\tau}}\right)\right\}\rangle\ \zeta\geq 0, 0\leq\tau\leq\tau_s, \quad (48)$$

$$T_2^*(\zeta,\tau)=4\sqrt{\tau}\left\langle\frac{\tau}{\tau_s}\left\{2\left[1+\left(\frac{\zeta}{2\sqrt{\tau}}\right)^2\right]\mathrm{ierfc}\left(\frac{\zeta}{2\sqrt{\tau}}\right)-\frac{\zeta}{2\sqrt{\tau}}\mathrm{erfc}\left(\frac{\zeta}{2\sqrt{\tau}}\right)\right\}-\right.$$
$$-\frac{1}{5}\left(\frac{\tau}{\tau_s}\right)^2\left[8+18\left(\frac{\zeta}{2\sqrt{\tau}}\right)^2+4\left(\frac{\zeta}{2\sqrt{\tau}}\right)^4\right]\mathrm{ierfc}\left(\frac{\zeta}{2\sqrt{\tau}}\right)-\left[7+\right.$$
$$\left.\left.2\left(\frac{\zeta}{2\sqrt{\tau}}\right)^2\right]\frac{\zeta}{2\sqrt{\tau}}\mathrm{erfc}\left(\frac{\zeta}{2\sqrt{\tau}}\right)\right\rangle,\zeta\geq 0, 0\leq\tau\leq\tau_s, \quad (49)$$

$$T_3^*(\zeta,\tau)=3\tau\sqrt{\frac{\pi}{\tau_s}}\left[\mathrm{erfc}\left(\frac{\zeta}{2\sqrt{\tau}}\right)-\frac{\zeta}{\sqrt{\tau}}\mathrm{ierfc}\left(\frac{\zeta}{2\sqrt{\tau}}\right)\right]-\frac{4\tau\sqrt{\tau}}{\tau_s}\left\{2\left[1+\right.\right.$$
$$\left.\left.\left(\frac{\zeta}{2\sqrt{\tau}}\right)^2\right]\mathrm{ierfc}\left(\frac{\zeta}{2\sqrt{\tau}}\right)-\frac{\zeta}{2\sqrt{\tau}}\mathrm{erfc}\left(\frac{\zeta}{2\sqrt{\tau}}\right)\right\},\zeta\geq 0, 0\leq\tau\leq\tau_s. \quad (50)$$

4. NUMERICAL ANALYSIS

Numerical analysis of the temperature distributions in a disc (semi-space) during single braking, for three different time courses of heat flux intensities, was conducted based on the found analytical solutions (48)–(50). The dimensionless input parameters used in calculations are: spatial coordinate ζ, time τ and braking time $\tau_s=1$, which are defined by formulas (7). According to equations (1) and (2) total amount of thermal energy absorbed by the disc during braking for considered intensities of heat flux is equal.

Evolutions of the dimensionless temperature on the friction surface and selected depths ζ inside semi-space for three changes with time of heat flux densities (Fig. 2), were shown in Fig. 3. The temperature distribution for intensity of heat flux $q_1^*(t)$, when its value is the largest on the initial stage of braking and decreases to zero with time, were presented in Fig. 3a. At the beginning of the braking temperature T_1^* on outer surface of semi-space $(\zeta=0)$ rapidly increases, to achieve maximum value $T_{1\max}^*=1.20$ in time $\tau/\tau_s=0.32$, and then decreases until the end of the process.

DOI 10.1515/ama-2017-0017

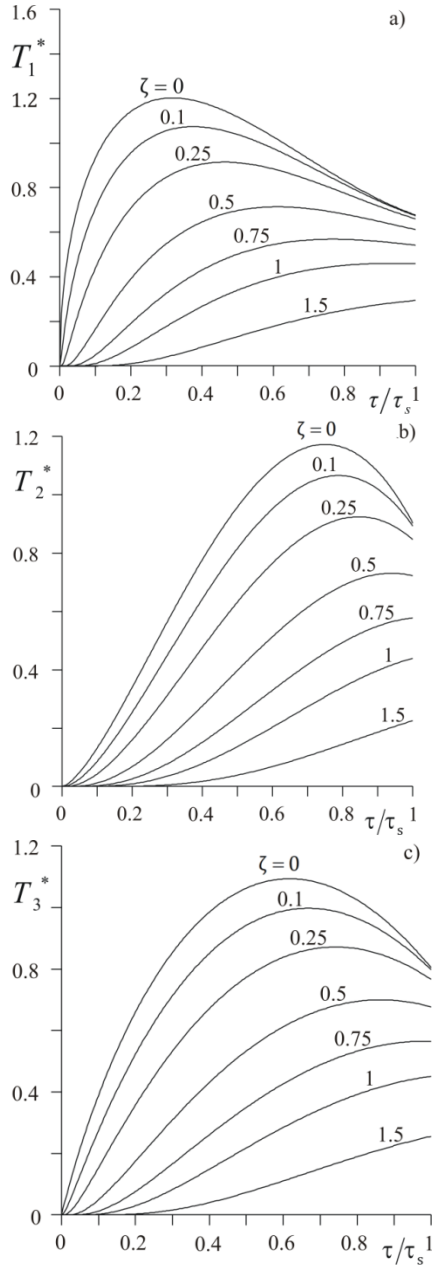

Fig. 3. Evolutions of the dimensionless temperatures a) T_1^*, b) T_2^*, c) T_3^* on few distances ζ from the friction surface

In the cases, when in initial stage of braking the heat flux intensity increase reaching maximum value in 25% ($\tau/\tau_s = 0.25$ for $q_3^*(t)$) or 50% ($\tau/\tau_s = 0.5$ for $q_2^*(t)$), of total braking time, reaching largest temperature value on the working surface also gets longer, and equals to, $\tau/\tau_s = 0.75$ for $T_{2max}^* = 1.17$ (Fig. 3b) and $\tau/\tau_s = 0.6$ for $T_{3max}^* = 1.09$ (Fig. 3c), respectively. In both cases after reaching maximum values, the temperature of the surface decreases to the standstill. The dimensionless temperature on the friction surface $\zeta = 0$ in the stop time moment $\tau/\tau_s = 1$ is higher in the case heating disc by heat flux intensity $q_2^*(t)$ (Fig. 3b) and $q_3^*(t)$ (Fig. 3c) compared with temperature value in brake disc heated by flux with intensity $q_1^*(t)$ (Fig. 3a). In the all considered cases, increasing distance ζ from the frictional surface (Fig. 3) the temperature value is getting lower and time to reach maximum increases. The monotonically temperature increase during the entire heating process with intensity $q_2^*(t)$ can be observed (Fig. 3b) on the distance $\zeta \geq 0.75$, and with $q_1^*(t)$ and $q_3^*(t)$ (Fig. 3a, 3c) under the effective depth of the heat penetration $\zeta \geq 1$.

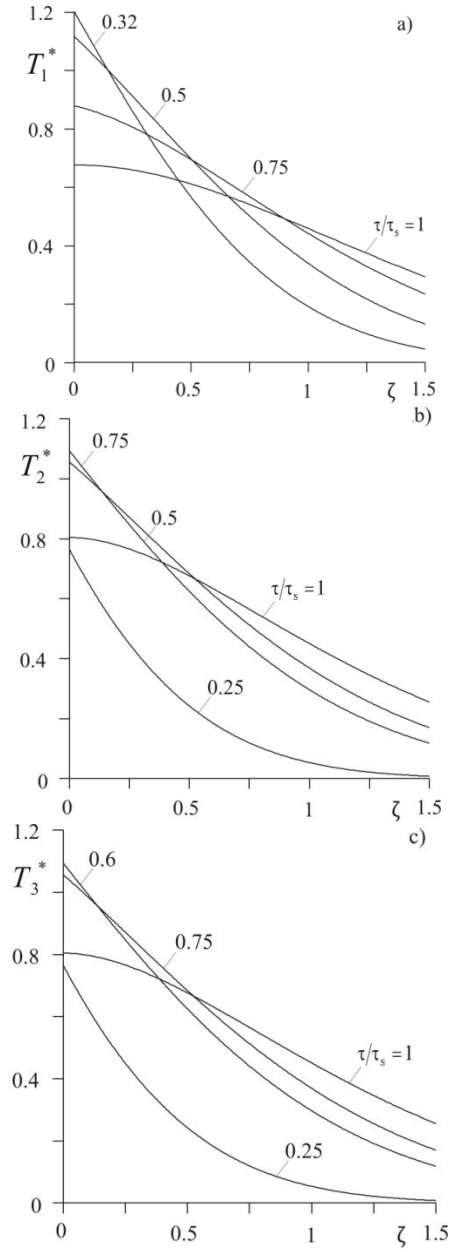

Fig. 4. Distribution of the dimensionless temperatures a) T_1^*, b) T_2^*, c) T_3^* inside disc at few different dimensionless time moments τ

The dimensionless temperature changes with depth ζ for different intensities of heat flux $q_i^*(t), i = 1,2,3$ in selected time moments τ, are shown in Fig. 4. In the all cases, the temperature monotonically decreases with increasing the distance ζ from heated surface. In the considered distance range $0 \leq \zeta \leq 1.5$, the largest gradients of the temperature inside the disc $\Delta T_1^* = 1.15$ (Fig. 4a), $\Delta T_2^* = 1.05$ (Fig. 4b) and $\Delta T_3^* = 0.98$ (Fig. 4c), occurs in the moments of reaching maximum temperature values on the friction surface $\zeta = 0$. The most uniform distributions of the temperature in disc are in standstill moment $\tau/\tau_s = 1$, temperatures on the working surface have lower values $T_1^* = 0.68$ (Fig. 4a), $T_2^* = 0.9$ (Fig. 4b) and $T_3^* = 0.8$ (Fig. 4c). Mentioned gradients reach minimum values $\Delta T_1^* = 0.38$ (Fig. 4a), $\Delta T_2^* = 0.64$ (Fig. 4b) and $\Delta T_3^* = 0.54$ (Fig. 4c) in the stop moment.

5. CONCLUSIONS

Analytical solutions to the heat conduction problems for semi-space heated on outer surface by heat flux with different time courses of intensity were determined. Numerical analysis of evolution and spatial distribution of the dimensionless temperature (along the distance from the friction surface) were carried out based on obtained solutions. In results the following conclusions were formulated:

- there is a strict relation between the time moment of reaching maximum values of dimensionless temperature on the heated surface and the time moment of maximum intensity occurrence of corresponding heat flux. In the considered cases, extreme temperature value is reached ca. 30% of braking time later than maximum of the heat flux intensity time function;
- maximum values of dimensional temperature on the friction surface of the disc, in all cases are similar. The largest difference between them is only 9% of this value. While, in these cases, maximum values of the friction power differ twofold;
- gradients of the dimensionless temperature inside the disc are the lowest in the standstill $\tau/\tau_s = 1$. The most intense cooling of the outer surface after reached maximum temperature, occurs in the first case $q_1^*(t)$, while the temperature achieve the largest maximum values.

Nomenclature: a – effective depth of heat penetration [m]; $\mathrm{erf(x)}$ – Gauss error function; $\mathrm{erfc(x)} = 1 - \mathrm{erf(x)}$ – complementary error function; $\mathrm{ierfc(x)} = \pi^{-1/2}\exp(-\mathrm{x}^2) - \mathrm{xerfc(x)}$ – integral of complementary error function; K – thermal conductivity [W K-1 m-1]; k – thermal diffusivity [m2 s-1]; q – intensity of the heat flux [W m-2]; T – temperature [K]; T^* – dimensionless temperature; $\mathrm{T_a}$ – initial temperature [K]; $\mathrm{T_0}$ –temperature scaling factor [K]; t – time [s]; $\mathrm{t_s}$– braking time [s]; w – braking work density [W m-2 s-1]; w^* – dimensionless braking work density; xyz – spatial coordinates [m]; $\Gamma(\mathrm{v},\mathrm{z})$ – gamma function; τ – dimensionless time (Fourier number); τ_s – dimensionless braking time; ζ – dimensionless depth.

REFERENCES

1. **Abramowitz M., Stegun I.A.** (1972), *Handbook of Mathematical Functions with Formulas, Graphs, and Tables*, National Bureau of Standards, Washington.
2. **Carlslaw H.S., Jaeger J. C.** (1959), *Conduction of Heat in Solids*, 2nd ed.Clarendon Press, Oxford.
3. **Chichinadze A.V.** (1967), *Estimation and investigation of external friction during braking*, Nauka, Moscow. – 231 p. (in Russian).
4. **Chichinadze A.V., Braun E.D., Ginsburg A.G., Ignat'eva Z.V.** (1979), *Calculation, Test and Selection of Frictional Couples*, Nauka, Moscow (in Russian).
5. **Evtushenko A., Kutsei, M.** (2007), Non-stationary frictional heat problem for plane-parallel layer—half-space system, *Journal of Friction and Wear*, 28(3), 246-259.
6. **Jewtuszenko O.** (red) (2014), *Analytical and numerical modelling of process of transient heat generation in friction components of brake systems*, Publisher of Technical University of Bialystok, Bialystok (in Polish).
7. **Kuciej M**. (2012), *Analytical models of transient frictional heating*, Publisher of Technical University of Bialystok, Bialystok (in Polish).
8. **Ling F.F.** (1973), *Surface Mechanics*, Wiley, New York.
9. **Matysiak S., Evtushenko O., Kuciej M.** (2007),Temperature field in the process of braking of a massive body with composite coating, *Materials Science*, 43(1), 62-69.
10. **Ozisik M.N**. (1993), *Heat conduction,* 2nd Ed. Wiley: New York.
11. **Prudnikov A. P., Brychkov Yu. A., Marichev O. I.** (1986), *Integrals and Series. Vol. 1: Elementary Functions*, Gordon and Breach: New York.
12. **Prudnikov A.P., Brychkov Yu.A., Marichev O. I.** (1998*), Integrals and Series. Vol. 2: Special Functions*, New York-London: Taylor & Francis.
13. **Topczewska K.** (2016), Temperature distribution in a brake disc with variable contact pressure*, Technical Issues*, 1, 90–95.
14. **Yevtushenko A. A., Kuciej M., Różniakowska M.** (2005), Thermal cleavage stresses in a piecewise homogeneous plate, *Materials Science,* 41 (5) 581-588.
15. **Yevtushenko A.A., Kuciej M.** (2006), Initiating of thermal cracking of materials by frictional heating, *J. Friction and Wear,* 27(2) 9-16.
16. **Yevtushenko A.A., Kuciej M.** (2009), Influence of convective cooling on the temperature in a frictionally heated strip and foundation, *International Communications in Heat and Mass Transfer*, 36(2), 129-136.
17. **Yevtushenko A.A., Kuciej M**. (2010), Two heat conduction problems with frictional heating during braking, *J. Theor. Appl. Mech.,* 48(2), 367–380.
18. **Yevtushenko A.A., Kuciej M., Yevtushenko O.O.** (2011), Temperature and thermal stresses in material of pad during braking, *Arch. Appl. Mech.,* 81(6), 715–726.
19. **Yevtushenko A.A., Kuciej M**. (2012), One-dimensional thermal problem of friction during braking: The history of development and actual state, *International Journal of Heat and Mass Transfer*, 55(15), 4148-4153.
20. **Yevtushenko A.A., Kuciej M., Yevtushenko O.** (2014), The asymptotic solutions of heat problem of friction for a three-element tribosystem with generalized boundary conditions on the surface of sliding, *International Journal of Heat and Mass Transfer*, 70, 128-136.
21. **Yevtushenko A.A., Rozniakowska M., Kuciej M.** (2007a), Transient temperature processes in composite strip and homogeneous foundation, *International Communications in Heat and Mass Transfer*, 34(9), 1108-1118.
22. **Yevtushenko A.A., Rozniakowska M., Kuciej M.** (2007b), Laser-induced thermal splitting in homogeneous body with coating. *Numerical Heat Transfer*, Part A: Applications, 52(4), 357-375.

This work is part of the project no. MB/WM/08/2017 which is carried out in the Faculty of Mechanical Engineering, Bialystok University of Technology.

DE GRUYTER
OPEN

DOI 10.1515/ama-2017-0018

APPLICATION OF FINITE ELEMENT METHOD FOR ANALYSIS OF NANOSTRUCTURES

Jozef BOCKO*, Pavol LENGVARSKÝ*

*Faculty of Mechanical Engineering, Department of Applied Mechanics and Mechanical Engineering,
Technical University of Košice, Letná 9, 042 00 Košice, Slovakia

jozef.bocko@tuke.sk, pavol.lengvarsky@tuke.sk

received 28 April 2016, revised 11 May 2017, accepted 15 May 2017

Abstract: The paper deals with application of the finite element method in modelling and simulation of nanostructures. The finite element model is based on beam elements with stiffness properties gained from the quantum mechanics and nonlinear spring elements with force-displacement relation are gained from Morse potential. Several basic mechanical properties of structures are computed by homogenization of nanostructure, e.g. Young's modulus, Poisson's ratio. The problems connecting with geometrical parameters of nanostructures are considered and their influences to resulting homogenized quantities are mentioned.

Key words: Beam Element, Spring Element, Young's Modulus, Poisson's Ratio

1. INTRODUCTION

The carbon structures attract the attention of researchers since the beginning of their investigation. Especially, electrical and mechanical properties of nanostructures have been widely investigated during last decade due to their interesting behaviour. The strength and stiffness characteristics of mechanical properties of nanostructures are much higher than those of steels. However, there is a problem with connection of carbon structure as a fibre with a steel matrix.

Nowadays, the analysis of nanostructure properties is based mostly on the following methods: molecular mechanics, molecular dynamics, continuum mechanics and experimental measurements. Tsai and Tu (2010) used molecular dynamics simulation for prediction of mechanical properties of graphene sheets. Continuum mechanics is well established for continuum theories of rods, beams, springs, shells, etc. (Li and Chou,2003; Meo and Rossi, 2006; Tserpes and Papanikos, 2005). The experimental measurements of mechanical properties of nanostructures are made in an atomic force microscope by nanoindentation (Lee et al., 2008).

The paper is devoted to investigation of Young's modulus and Poisson's ratio of nanostructure. These material characteristics are very important but still there are great uncertainties in their accurate determination. In the paper are investigated graphene sheets with different chiralities, widths, and lengths. The nanostructures are modelled using the MSM approach by either beam or spring elements. The carbon atoms are considered to be finite elements nodes and the interatomic interactions are represented by the structural elements (Li and Chou, 2003; Meo and Rossi, 2006; Hosseini and Moshrefzadeh, 2013).

2. GRAPHENE SHEET IN MOLECULAR MECHANICS

The graphene sheets can be regarded in molecular mechanics as large molecules consisting of carbon atoms and the atomic nuclei as material points. The motion of atomic nuclei is described by laws of force field. This field is expressed in the form of steric potential energy (Tserpes and Papanikos, 2005). The total steric potential energy (Saito et al., 1998; Thostenson et al., 2005) is a sum of energies due to valence or bonded interactions and non-bonded (van der Walls) interactions. It can be expressed by relation

$$U_{total} = \sum U_r + \sum U_\theta + \sum U_\phi + \sum U_\omega + \sum U_{vdw}, \qquad (1)$$

where $U_r, U_\theta, U_\phi, U_\omega, U_{vdw}$ are a bond stretching, a bond angle bending, a dihedral angle torsion, an improper (out of plane) torsion and a non-bonded van der Waals interaction, respectively (Mayo et al., 1990; Shokrieh and Rafiee, 2010; Tserpes and Papanikos, 2005).

2.1. Properties of beam element

The properties of beam element are related to the first four terms of equation (1). By adopting the simplest harmonic forms and merging dihedral angle torsion and out-of-plane torsion into a single equivalent term, we can write the following relations

$$U_r = \frac{1}{2}k_r(r - r_0)^2 = \frac{1}{2}k_r(\Delta r)^2, \qquad (2)$$

$$U_\theta = \frac{1}{2}k_\theta(\theta - \theta_0)^2 = \frac{1}{2}k_\theta(\Delta\theta)^2, \qquad (3)$$

$$U_\tau = U_\phi + U_\theta = \frac{1}{2}k_\tau(\Delta\phi)^2, \qquad (4)$$

where $k_r, k_\theta, k_\tau, \Delta r, \Delta\theta, \Delta\phi$ are the bond stretching force constant, bond angle bending force constant, torsional resistance, the

DOI 10.1515/ama-2017-0018

bond stretching increment, the bond angle variation and the angle variation of bond twisting, respectively (Brenner, 1990; Cornell et al., 1995; Rappe et al., 1992).

The elastic moduli of beam elements are evaluated from mechanical considerations – relations between the sectional stiffness parameters in structural mechanics and the force constants in molecular mechanics. In case the sections of beams representing carbon-carbon bonds, are assumed to be identical and circular, then the moments of inertia are $\mathrm{I_x} = \mathrm{I_y} = \mathrm{I}$. Three stiffness parameters EA, EI and GJ are obtained from this assumption and from linkage among the energy terms in molecular mechanics and continuum mechanics. It is possible write relations

$$U_A = \frac{1}{2}\int_0^L \frac{N^2}{EA} dL = \frac{1}{2}\frac{N^2 L}{EA} = \frac{1}{2}\frac{EA}{L}(\Delta L)^2, \quad (5)$$

$$U_M = \frac{1}{2}\int_0^L \frac{M^2}{EI} dL = \frac{2EI}{L}\alpha^2 = \frac{1}{2}\frac{EI}{L}(2\alpha)^2, \quad (6)$$

$$U_T = \frac{1}{2}\int_0^L \frac{T^2}{GJ} dL = \frac{1}{2}\frac{T^2 L}{GJ} = \frac{1}{2}\frac{GJ}{L}(\Delta\beta)^2, \quad (7)$$

where $\mathrm{U_A}$ is the strain energy of a uniform beam of length L subjected to axial force N, $\Delta\mathrm{L}$ is axial elongation, $\mathrm{U_M}$ is the strain energy of a uniform beam under bending moment M, α is the rotational angle at the ends of the beam, $\mathrm{U_T}$ is the strain energy of a uniform beam under tension T and $\Delta\beta$ is the relative rotation between the ends of the beam (Li and Chou, 2003; Tserpes and Papanikos, 2005).

Comparision of equations (2)-(4) and (5)-(7) leads to relations

$$\frac{EA}{L} = k_r, \frac{EI}{L} = k_\theta, \frac{GJ}{L} = k_\tau. \quad (8)$$

On the basis of these equations a beam element (Fig. 1) is created and its elastic properties for further computations are

$$d = 4\sqrt[4]{\frac{k_\theta}{k_r}}, E = \frac{{k_r}^2 L}{4\pi k_\theta}, G = \frac{{k_r}^2 k_\tau L}{8\pi k_\theta^2}, \quad (9)$$

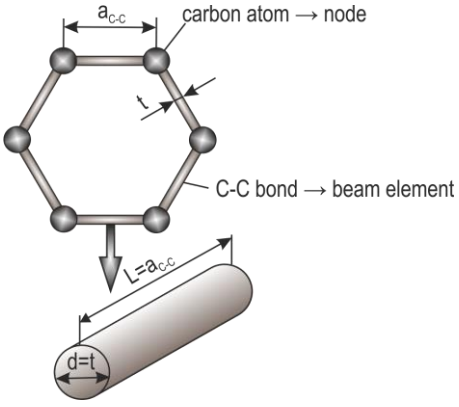

Fig. 1. Hexagon unit cell of graphene sheet with beam elements

where constants $\mathrm{k_r}, \mathrm{k_\theta}, \mathrm{k_\tau}, \mathrm{L}$ are $\mathrm{k_r} = 6.52 \times 10^{-7}\ \mathrm{Nnm^{-1}}$, $\mathrm{k_\theta} = 8.76 \times 10^{-10}\ \mathrm{N\,nm\,rad^{-1}}, \mathrm{k_\tau} = 2.78 \times 10^{-7}\ \mathrm{N\,n\,m\,rad^{-2}}$ and $\mathrm{L} = \mathrm{a_{C-C}} = 0.1421\ \mathrm{nm}$ (Marenić et al., 2013).

Accordingly, the quantities from equations (9) are calculated and we come to diameter $\mathrm{d} = 0.147\ \mathrm{nm}$, elastic modulus $\mathrm{E} = 5.4875\ \mathrm{TPa}$ and $\mathrm{G} = 0.871\ \mathrm{TPa}$ for beam elements.

2.2. Properties of spring elements

The properties of spring elements come from the Morse potential. The Morse potential is used for evaluation of interactions of C-C bond stretching and C-C-C bond angle bending. The Morse potential for C-C and C-C-C bonds is computed according to eqs. (10)-(11). All necessary parameters for computations are given in Tab. 1 (Machida, 1999; Rafiee and Heidarhaei, 2012).

$$u_r = D_e\left\{\left[1 - e^{-\beta(r-r_0)}\right]^2\right\}, \quad (10)$$

$$u_\theta = \frac{1}{2}k_\theta(\theta - \theta_0)^2[1 + k_{sextic}(\theta - \theta_0)^4]. \quad (11)$$

In this paper C-C and C-C-C bonds are modelled with nonlinear spring elements. The knowledge of force-displacement relationship for C-C bonds is necessary and this quantity is derived from the Morse potential using eq. (10) (Rafiee and Heidarhaei, 2012)

$$F(r - r_0) = 2\beta D_e\left[1 - e^{-\beta(r-r_0)}\right]e^{-\beta(r-r_0)}. \quad (12)$$

Function for C-C-C bonds is derived by using eq. (11) and the result is expressed by equation (Rafiee and Heidarhaei, 2012]

$$M(\theta - \theta_0) = k_\theta(\theta - \theta_0)[1 + 3k_{sextic}(\theta - \theta_0)^4]. \quad (13)$$

Tab. 1. Parameters for the Morse potential

parameter	value
D_e	$6.03105 \times 10^{-19}\ \mathrm{Nm}$
β	$2.6259 \times 10^{10}\ \mathrm{m^{-1}}$
r_0	$0.1421\ \mathrm{nm}$
k_θ	$0.9 \times 10^{-18}\ \mathrm{N}\frac{\mathrm{m}}{\mathrm{rad^2}}$
k_{sextic}	$0.754\ \mathrm{rad^4}$
θ_θ	$2.094\ \mathrm{rad}$

Every hexagon of graphene sheet is modelled by 12 nonlinear springs. Six outer springs represent bond stretching and six inner springs represent bond angle bending (Fig. 2). Bond angle torsion is not considered in the frame of this spring model.

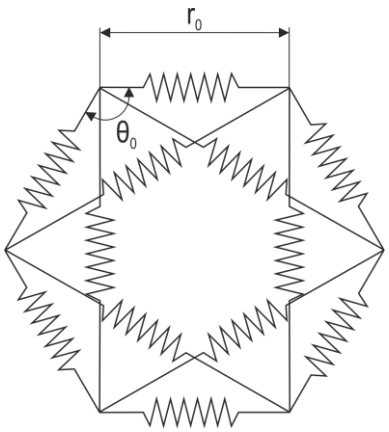

Fig. 2. Hexagon unit cell of graphene sheet with 12 nonlinear spring elements

The change of length of nonlinear spring of C-C-C bond leads to change of bond angle. This fact can be described by equation

DOI 10.1515/ama-2017-0018

$$\Delta\theta = \frac{2(\Delta R)}{r_0}, \tag{14}$$

where Δθ is variation of bond angle, r_0 is C-C bond length and ΔR is change of spring element length. Accordingly, force-displacement relationship in eq. (13) is rewritten into form of relation

$$F_{(R-R_0)} = \frac{4}{r_0^2} k_\theta (R - R_0)\left[1 + \frac{48}{r_0^4} k_{sextic} (R - R_0)^4\right]. \tag{15}$$

The nonlinear behaviour of this spring is shown in Fig. 3 and Fig. 4.

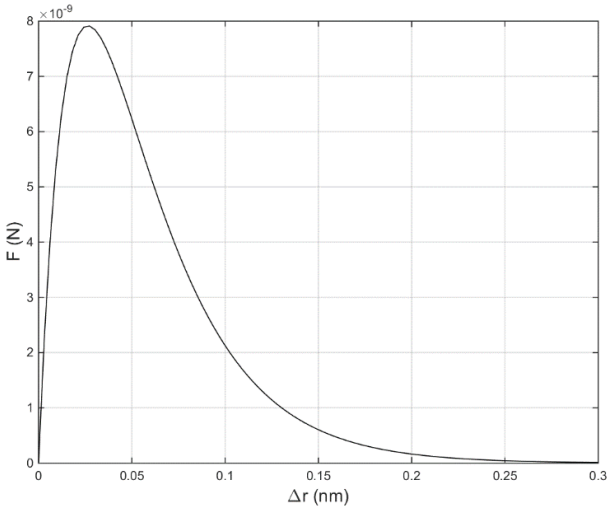

Fig. 3. Force-displation curve for nonlinear spring representing bond stretching

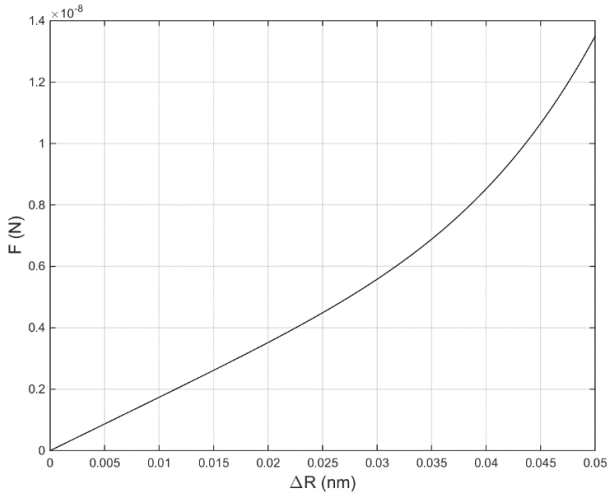

Fig. 4. Force-displation curve for nonlinear spring representing change of bond angle

3. NUMERICAL RESULTS

The numerical computations are accomplished by the finite element program Ansys. The structural response of the graphene sheets under axial loads is analyzed for both model types (Figs. 5-6). Carbon atoms are considered to be nodes in structure and the nodes are joined by beam elements or nonlinear spring elements. To simulate the uniaxial load, one side of the graphene sheet is restrained in all direction. The graphene sheets are stretched by applying an axial displacement on the opposite side. From these simulations the Young's modulus E, the Poisson's ratio μ of graphene sheets are obtained. The two graphene sheets with armchair chirality (6,6) and zigzag chirality (10,0) are modelled and analyzed. The width of the graphene sheet (6,6) and (10,0) is 2.5578 nm and 2.4612 nm, respectively. The length of the graphene sheets varied in interval 3 nm to 100 nm.

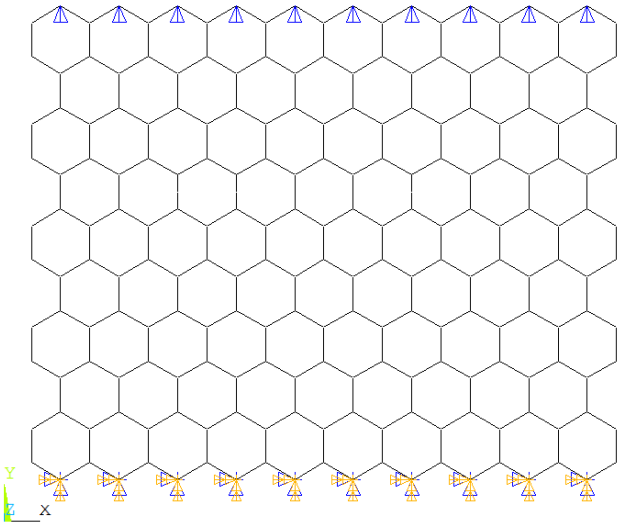

Fig. 5. Graphene sheet with beam elements and boundary conditions

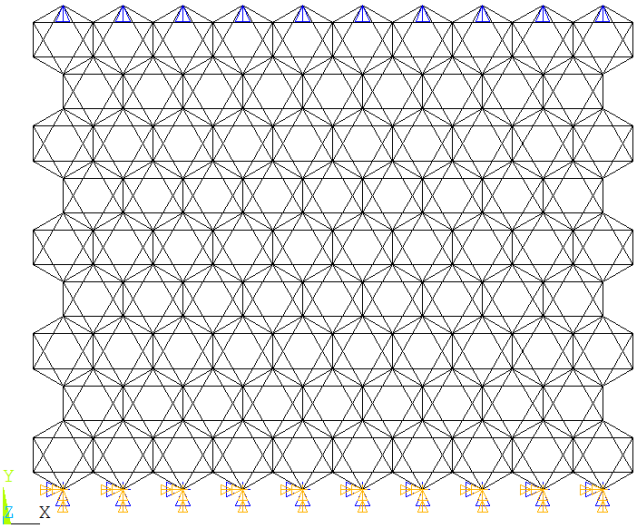

Fig. 6. Graphene sheet with nonlinear spring elements and boundary conditions

Young's moduls E is calculted from equation

$$E = \frac{\sigma}{\varepsilon} = \frac{F/Wt}{\Delta L/L}, \tag{16}$$

where F is reaction force, W is width, t is thickness, ΔL is elongation and L is length of graphene sheet. The thickness of graphene sheet is assumed to be 0.34 nm. Poisson's ratio is computed from equation

$$\mu = \frac{\Delta W/W}{\Delta L/L}, \tag{17}$$

where ΔW is constriction of graphene sheet.

DOI 10.1515/ama-2017-0018

All computed values of Young's moduls E and the Poisson's ratio μ are shown in Figs. 7-8.

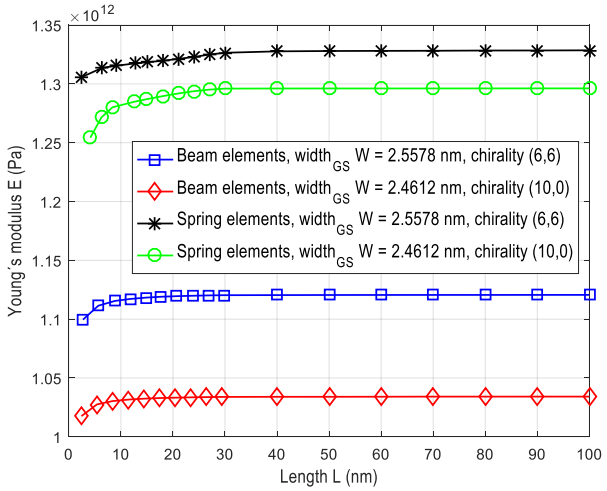

Fig. 7. Young's modulus of graphene sheet with diferent elements, length and width

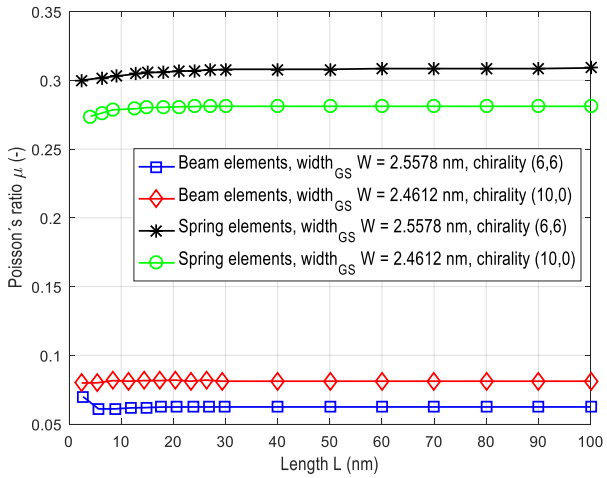

Fig. 8. Poisson's ratio of graphene sheet with diferent elements, length and width

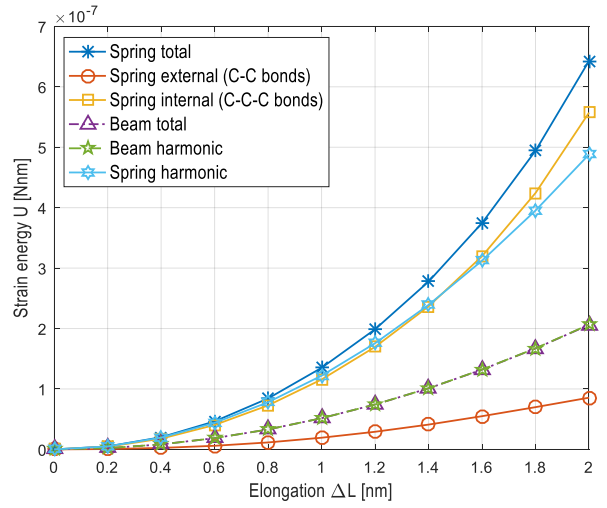

Fig. 9. Strain energy of graphene sheet with dimensions 2.4612 x 8.3858 nm subjected to axial tension obtained from beam and spring model

4. CONCLUSION

The Young's modulus E increases slightly with the size of the sheets and depends on the chirality. The beam and spring models give almost the same results for E with the obtained values being in good agreement with literature (Hartmann et al., 2013; Meo and Rossi, 2006; Rafiee and Heidarhaei, 2012; Scarapa et al., 2009; Tserpes and Papanikos, 2005). For the Poisson's ratio μ the beam and spring models give strongly different results. Depending on the chirality, values of μ between 0.08 and 0.06 are obtained for the beam model. For the spring model values of μ vary between 0.28 and 0.31 and accordingly there are no strong size and chirality dependencies for the same model. Although the beam and spring models give different results for μ all values are within the range reported in literature (Hartmann et al., 2013; Hemmasizadeh et al., 2008; Ru, 2000; Sakhaee-Pour, 2009; Tsai and Tu, 2010). It is assumed that different values of μ depend on the different representation of the bond angle bending in the beam and spring models. In order to see the influence of the bond angle bending, the total strain energy of the stretched graphene sheets is estimated for both models. The results from numerical computations are shown in Fig. 9. For the spring model the total strain energy can be split into a bond stretching and a bond angle contribution. It can be seen that the total strain energy of the spring model is much higher than the strain energy of the beam model, where stronger contribution comes from the bond angle bending deformations. This shows the bond angle bending is probably not correctly represented in the beam model. This may lead to the relatively small Poisson's ratio of this model and may cause further issues for loading cases where bond angle bending is important. By comparison between strain energy of the spring model and corresponding harmonic potentials it is also shown that graphene sheets work in linear elastic area up to a stretch of approximately 10 percent. Due to the assumptions made for the beam elements no non-linear behavior can be observed for this model. Hence, it is valid only for small deformations.

REFERENCES

1. **Brenner D.W.** (1990), Empirical potential for hydrocarbons for use in simulating the chemical vapor deposition of diamond films, *Physical Review B*, Vol. 42, 9458.
2. **Cornell W.D., Cieplak P., Bayly C.I.** (1995), A second generation force-field for the simulation of proteins, nucleic-acids, and organic-molecules, *Journal of American Chemical Society*, 117, 5179-5197.
3. **Hartmann M.A., Todt M., Rammerstorfer F.G., Fisher F.D., Paris O.** (2013), Elastic properties of graphene obtained by computational mechanical tests, *Europhysics Letters*, 103, 68004-p1-68004-p6.
4. **Hemmasizadeh A., Mahzoon M., Hadi E., Khandan R.** (2008), A method for developing the equivalent continuum model of a single layer graphene sheet, *Thin Solid Films*, 516, 7636-7640.
5. **Hosseini K.S.A., Moshrefzadeh S.H.** (2013), Mechanical properties of double-layered graphene sheets, *Computational Materials Science*, 69, 335-343.
6. **Lee C., Wei X., Kysar J.W., Hone J.** (2008), Measurement of the elastic properties and intrisic strength of monolayer graphene, *Science*, 321, 385-388.
7. **Li Ch., Chou T.W.** (2003), A structural mechanics approach for the analysis of carbon nanotube, *International Journal of Solids and Structures*, 40, 2487-2499.
8. **Machida K.** (1999), *Principles of Molecular Mechanics*, Kodansha and John Wiley & Sons Co-publication, Tokyo.

DOI 10.1515/ama-2017-0018

9. **Marenić E., Ibrahimbegovic A., Sorić J., Guidault P.A.** (2013), Homogenized elastic properties of graphene for small deformations, *Materials*, 6, 3764-3782.
10. **Mayo S.L., Olafson B.D., Goddard W.A.** (1990), Dreiding–a generic force-field for molecular simulations, *Journal of Physical Chemistry*, 94, 8897–8909.
11. **Meo M., Rossi M.** (2006), Prediction of Young's modulus of single wall carbon nanotubes by molecular-mechanics based finite element modelling, Composite Science and Technology, 66, 1597-1605.
12. **Rafiee R., Heidarhaei M.** (2012), Investigation of chirality and diameter effects on the Young's modulus of carbon nanotubes using non-linear potentials, *Composite Structures*, 94, 2460-2464.
13. **Rappe A.K., Casewit C.J., Colwell K.S.** (1992), A full periodic-table force-field for molecular mechanics and molecular dynamics simulations, *Journal of American Chemical Society*, 114, 10024-10035.
14. **Ru C.Q.** (2000), Effective bending stiffness of carbon nanotubes, *Physical Review B*, 62, 9973-9976.
15. **Saito S., Dresselhaus D., Dresselhaus M.S.** (1998), *Physical Properties of Carbon Nanotubes*, Imperical College Press, London.
16. **Sakhaee-Pour A.** (2009), Elastic properties of single-layered graphene sheet, *Solid State Communications*, 149, 91-95.
17. **Scarapa F., Adhikari S., Srikantha P.** (2009), Effective elastic mechanical properties of single layer graphene sheets, *Nanotechnology*, 20, 065709.
18. **Shokrieh M.M, Rafiee R.** (2010) Prediction of Young's modulus of graphene sheets and carbon nanotubes using nanoscale continuum mechanics approach, *Materials & Design*, 31, 790-795.
19. **Thostenson E.T., Chunyu L., Chou T.W.** (2005), Nanocomposites in context, *Composite Science and Technology*, 65, 491-516.
20. **Tsai J.L., Tu J.F.** (2010), Characterizing mechanical properties of graphite using molecular dynamics simulation, *Materials & Design*, 31, 194-199.
21. **Tserpes K.I., Papanikos P.** (2005), Finite element modelling of single-walled carbon nanotubes, *Composites Part B,* 36, 468-477.

This work was supported by grants from the Slovak Grant Agency VEGA no. 1/0731/16.

DE GRUYTER
OPEN

DOI 10.1515/ama-2017-0019 acta mechanica et automatica, vol.11 no.2 (2017)

DETERMINATION OF DISPERSION CURVES FOR COMPOSITE MATERIALS WITH THE USE OF STIFFNESS MATRIX METHOD

Marek BARSKI*, Piotr PAJĄK*

*Institute of Machine Design, Faculty of Mechanical Engineering, Cracow University of Technology,
al. Jana Pawła II 37, 31-864, Kraków, Poland

mbar@mech.pk.edu.pl, ppajak@mech.pk.edu.pl

received 10 October 2016, revised 11 May 2017, accepted 15 May 2017

Abstract: Elastic waves used in Structural Health Monitoring systems have strongly dispersive character. Therefore it is necessary to determine the appropriate dispersion curves in order to proper interpretation of a received dynamic response of an analyzed structure. The shape of dispersion curves as well as number of wave modes depends on mechanical properties of layers and frequency of an excited signal. In the current work, the relatively new approach is utilized, namely stiffness matrix method. In contrast to transfer matrix method or global matrix method, this algorithm is considered as numerically unconditionally stable and as effective as transfer matrix approach. However, it will be demonstrated that in the case of hybrid composites, where mechanical properties of particular layers differ significantly, obtaining results could be difficult. The theoretical relationships are presented for the composite plate of arbitrary stacking sequence and arbitrary direction of elastic waves propagation. As a numerical example, the dispersion curves are estimated for the lamina, which is made of carbon fibers and epoxy resin. It is assumed that elastic waves travel in the parallel, perpendicular and arbitrary direction to the fibers in lamina. Next, the dispersion curves are determined for the following laminate [0°, 90°, 0°, 90°, 0°, 90°, 0°, 90°] and hybrid [Al, 90°, 0°, 90°, 0°, 90°, 0°], where Al is the aluminum alloy PA38 and the rest of layers are made of carbon fibers and epoxy resin.

Key words: Structural Health Monitoring, Layered Composite Materials, Guided Waves, Dispersion Curves, Stiffness Matrix Method

1. INTRODUCTION

Nowadays layered composite materials are widely used in different structures. This is particularly evident in the aerospace industry. The main advantage of using composite materials is the fact that structures are substantially lighter in comparison with structures made of traditional isotropic materials, like steel or aluminum alloys. On the other hand, process of damage formation and evaluation in composite materials is much more complex. In order to detect the different kind of flaws (matrix cracking, fiber brakeage or delamination), sophisticated methods have to be applied. Some of them are based on an analysis of propagation of elastic waves, which travel through the investigated structure (Giurgiutiu, 2008). Generally, this kind of systems can be applied in two different configurations, namely pitch-catch and pulse-echo. First approach is based on the comparison of received signals for intact and interrogated structure. In the case when the signals are different, it means that inside the material there is a damage. It is worth stressing here that without the knowledge about an intact structure, the damage detection is impossible. This is the main disadvantage of this approach. The latter method is based on an analysis of received reflection of elastic waves from a flaw. Thus this approach can be utilized in the case when the dynamic response of an intact structure is unknown. However, elastic waves have strongly dispersive nature (Royer and Dieulesaint, 2000). Moreover, depending on the frequency of the excitation signal, the different number of wave modes are present. Therefore, for appropriate interpretation of a picked up dynamic response of the structure, the dispersion curves have to be determined. However, it could be a very difficult task in the case of composite structure. One of the first approach, known as the transfer matrix method was proposed by Thompson (1950). He introduced so called transfer matrix, which relates the displacement and stress at the top and bottom of the layer. The matrices for any number of isotropic layers could be coupled into one. This approach was further corrected by Haskell (1953). Originally, this approach is limited to the materials where all layers are made of isotropic materials. Nayfeh (1991;1995) extended this method to the case, where layers are made of anisotropic materials. The transfer matrix method is relatively simple and easy to use. The first computer applications based on this algorithm were developed in the sixties of the last century (Press et al., 1961; Randall, 1967). However, this method is numerically unstable in the case of relatively high frequencies as well as thicker layers. This problem is well known in literature as "fd problem" (Lowe, 1995). An alternative to the transfer matrix algorithm is the global matrix method proposed by Knopoff (1964). In this approach the dynamic properties of a whole composite material are described by single matrix (global matrix). The size of this matrix directly depends on the number of layers. Besides, the fd problem is still present in this formulation. Initially, this method was applied in the case of isotropic layers (Schwab 1970; Schmidt and Tango, 1986). Nowadays, the global matrix method is also applied in the case of composites, which consist of anisotropic layers (Pant et al., 2014). There is also available a commercial program DISPERSE (Pavlakovic and Lowe, 2003), which is based on this approach. The third analytical method of dispersion curves determination was proposed by Kausel (1986) and further developed by Wang and Rokhlin (2001; 2002a; 2002b). It is known as the stiffness matrix method. According to its authors, this method is numerically unconditionally stable. The mentioned above transfer matrix is replaced by a layer

DOI 10.1515/ama-2017-0019

stiffness matrix, which relates the stresses at the top and the bottom of the layer with the displacement at the top and bottom of the layer. Next, the global stiffness matrix for the whole composite material is obtained by the use of an effective, recursive algorithm. It is worth stressing here that the numerical stability is achieved by replacing the exponential terms from the diagonal of the stiffness matrix. Besides, this approach has the same dimension and is only slightly more computationally efficient in comparison with the transfer matrix method (Giurgiutiu, 2008). This approach is used by Kamal and Giurgiutiu (2014) in case of the multilayered anisotropic composites. The authors also verify the stiffness matrix method with the use of the transfer matrix method, program DISPRESE and the semi-analytical finite element method (Sorohan et al., 2011). It seems that nowadays the stiffness matrix method is the most effective analytical method, which enables the dispersion curves determination. However, in the case of composites, where there is a significant difference between the stiffness of the particular layer or there are strongly orthotropic layers, the numerical problems may be still present. Therefore, the main aim of this work is to estimate the dispersion curves for the composites, which consist of this kind of layer materials, namely fibers with epoxy resin (CFRP, Fibers T300, Matrix N5208) and aluminum alloy PA38. Moreover, the present work should be considered as the continuation of the previous studies (Barski and Pająk, 2016). In that paper the dispersion curves obtained for a single lamina and for a multilayered composite material with quasi - isotropic mechanical properties are presented. The computations were made for the glass fibers GFRP E-glass and epoxy resin.

2. THEORETICAL MODEL OF LAMB'S WAVES PROPAGATION IN MULTILAYERED MATERIALS

Let us consider the composite layered material, which is shown in Fig. 1. It is assumed that the analyzed medium consists of n orthotropic layers. Mechanical properties of each layer are described in local coordinate system (x'_1, x'_2, x'_3). It is worth stressing here that the origin of the local coordinate system is chosen to coincide with the top surface of the particular layer, what is shown in Fig 2. The thickness of k-th layer is equal to dk. The particular layers are stacked normal to the x_3 axis of the global coordinate system. Thus, the plane of each layer is parallel to the (x_1, x_2) one of the global coordinate system. The wave is allowed to travel on arbitrary incident angle θ, which is measured with respect to the direction normal to the (x_1, x_2) plane, and along any angle φ. The angle φ is shown in Fig. 2. The theoretical model is formulated according to the following assumptions (Giurgiutiu, 2008; Lowe, 1995; Pant et al., 2014):

1. All layers are perfectly bonded at their interfaces.
2. The wave propagates along the $x_1 - x_3$ direction of the global coordinate system. Hence, the mechanical properties of each layer, which are defined in the local coordinate system have to be transformed to the global coordinate system
3. In each monoclinic layer there are six partial waves, namely $(+P, -P)$, $(+SV, -SV)$ and $(+SH, -SH)$ representing quasi – longitudinal (symmetric), quasi shear vertical and quasi – shear horizontal waves, respectively. The waves with plus sign are arriving from above of the interface of particular layer and the waves with the minus sign are leaving the interface.
4. The Snell's law requires that all interacting particular waves must share the same frequency ω and spatial properties in x_1 direction at each interface. It results that in all equations, which describe the components of displacement and stress, there are the same circular frequency ω and k_1 component of the wave vector. The k_1 is the projection of the wave vector of the bulk wave onto the interface
5. The analyzed composite material is surrounded by vacuum. In other words, it is assumed that the traveling wave doesn't interact with the external environment. Hence, on the top and bottom surface of the composite material the following components of stress are equal to 0: $\sigma_{i,3}$ =0, i=1,2,3.

Most methods for solving the propagation of Lamb waves in an anisotropic medium are based on the partial wave technique. In this approach the superposition of the three upward and downward propagating waves are assumed. Taking under consideration the above assumptions, the formal solution for displacement can be proposed as follows (Hawwa, Nayfeh, 1995):

$$(u_1, u_2, u_3) = (U_1, U_2, U_3)e^{i\xi(x_1 \sin\theta + \alpha x_3 - ct)} \quad (1)$$

where u_j are the components of displacement, U_i are the amplitudes of u_j. ξ denotes the wave number, α is the unknown parameter (its value will be determined later) and c, t are the phase velocity and time, respectively. For the sake of simplicity, in the further discussion the θ angle is set to be equal to $\theta = 90°$.

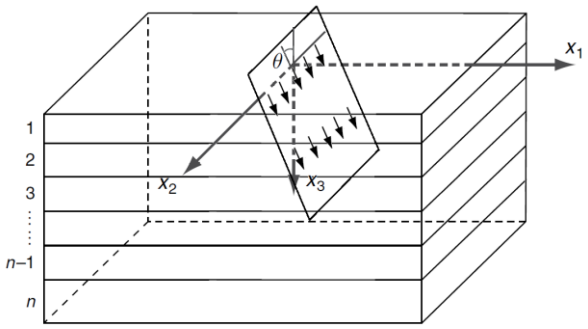

Fig. 1. Composite material with a plane wave propagating in $x_1 - x_3$ direction (Giurgiutiu, 2008)

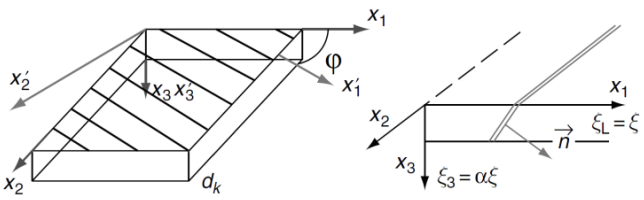

Fig. 2. The k-th layered of thickness d_k with local and global coordinate system (Giurgiutiu, 2008)

3. ELASTIC WAVES PROPAGATION IN SINGLE MONOCLINIC LAYER

According to Giurgiutiu (2008), it is assumed that the relationship between stress components and strain components in the case of single monoclinic layer of thickness d_k can be written as follows:

DOI 10.1515/ama-2017-0019

$$\begin{Bmatrix}\sigma_{11}\\ \sigma_{22}\\ \sigma_{33}\\ \sigma_{23}\\ \sigma_{13}\\ \sigma_{12}\end{Bmatrix}=\begin{bmatrix}C_{11} & C_{12} & C_{13} & 0 & 0 & C_{16}\\ C_{12} & C_{22} & C_{23} & 0 & 0 & C_{26}\\ C_{13} & C_{23} & C_{33} & 0 & 0 & C_{36}\\ 0 & 0 & 0 & C_{44} & C_{45} & 0\\ 0 & 0 & 0 & C_{45} & C_{55} & 0\\ C_{16} & C_{26} & C_{36} & 0 & 0 & C_{66}\end{bmatrix}\begin{Bmatrix}\varepsilon_{11}\\ \varepsilon_{22}\\ \varepsilon_{33}\\ \varepsilon_{23}\\ \varepsilon_{13}\\ \varepsilon_{12}\end{Bmatrix}. \tag{2}$$

Note that the above relation is defined in the global coordinate system (Fig. 1). Next, the linear relationships between the components of displacement and components of strain are given by:

$$\begin{aligned}&\varepsilon_{11}=\frac{\partial u_1}{\partial x_1},\quad \varepsilon_{22}=\frac{\partial u_2}{\partial x_2},\quad \varepsilon_{33}=\frac{\partial u_3}{\partial x_3}\\ &\varepsilon_{23}=\frac{\partial u_2}{\partial x_3}+\frac{\partial u_3}{\partial x_2},\quad \varepsilon_{13}=\frac{\partial u_1}{\partial x_3}+\frac{\partial u_3}{\partial x_1},\\ &\varepsilon_{12}=\frac{\partial u_1}{\partial x_2}+\frac{\partial u_2}{\partial x_1}\end{aligned} \tag{3}$$

Finally, the equations of motion take the following form:

$$\begin{aligned}&\frac{\partial\sigma_{11}}{\partial x_1}+\frac{\partial\sigma_{12}}{\partial x_2}+\frac{\partial\sigma_{13}}{\partial x_3}=\rho\frac{\partial^2 u_1}{\partial t^2},\\ &\frac{\partial\sigma_{21}}{\partial x_1}+\frac{\partial\sigma_{22}}{\partial x_2}+\frac{\partial\sigma_{23}}{\partial x_3}=\rho\frac{\partial^2 u_2}{\partial t^2},\\ &\frac{\partial\sigma_{13}}{\partial x_1}+\frac{\partial\sigma_{23}}{\partial x_2}+\frac{\partial\sigma_{33}}{\partial x_3}=\rho\frac{\partial^2 u_3}{\partial t^2}.\end{aligned} \tag{4}$$

Combining the equations (2), (3) and (4), the system of three coupled equations is obtained, namely:

$$\begin{aligned}&C_{11}\frac{\partial^2 u_1}{\partial {x_1}^2}+C_{66}\frac{\partial^2 u_1}{\partial {x_2}^2}+C_{55}\frac{\partial^2 u_1}{\partial {x_3}^2}+2C_{16}\frac{\partial^2 u_1}{\partial x_1\,\partial x_2}+C_{16}\frac{\partial^2 u_2}{\partial {x_1}^2}+C_{26}\frac{\partial^2 u_2}{\partial {x_2}^2}+C_{45}\frac{\partial^2 u_2}{\partial {x_3}^2}+(C_{12}+C_{66})\frac{\partial^2 u_2}{\partial x_1\,\partial x_2}+(C_{13}+C_{55})\frac{\partial^2 u_3}{\partial x_1\,\partial x_3}\\ &\qquad+(C_{36}+C_{45})\frac{\partial^2 u_3}{\partial x_2\,\partial x_3}=\rho\frac{\partial^2 u_1}{\partial t^2}\\ &C_{16}\frac{\partial^2 u_1}{\partial {x_1}^2}+C_{26}\frac{\partial^2 u_1}{\partial {x_2}^2}+C_{45}\frac{\partial^2 u_1}{\partial {x_3}^2}+(C_{12}+C_{66})\frac{\partial^2 u_1}{\partial x_1\,\partial x_2}+C_{66}\frac{\partial^2 u_2}{\partial {x_1}^2}+C_{22}\frac{\partial^2 u_2}{\partial {x_2}^2}+C_{44}\frac{\partial^2 u_2}{\partial {x_3}^2}+2C_{26}\frac{\partial^2 u_2}{\partial x_1\,\partial x_2}+(C_{36}+C_{45})\frac{\partial^2 u_3}{\partial x_1\,\partial x_3}\\ &\qquad+(C_{23}+C_{44})\frac{\partial^2 u_3}{\partial x_2\,\partial x_3}=\rho\frac{\partial^2 u_2}{\partial t^2}\\ &(C_{13}+C_{55})\frac{\partial^2 u_1}{\partial x_1\,\partial x_3}+(C_{36}+C_{45})\frac{\partial^2 u_1}{\partial x_2\,\partial x_3}+(C_{36}+C_{45})\frac{\partial^2 u_2}{\partial x_1\,\partial x_3}+(C_{23}+C_{44})\frac{\partial^2 u_2}{\partial x_2\,\partial x_3}+C_{55}\frac{\partial^2 u_3}{\partial {x_1}^2}+C_{44}\frac{\partial^2 u_3}{\partial {x_2}^2}+C_{33}\frac{\partial^2 u_3}{\partial {x_3}^2}\\ &\qquad+2C_{45}\frac{\partial^2 u_2}{\partial x_1\,\partial x_2}=\rho\frac{\partial^2 u_3}{\partial t^2}\end{aligned} \tag{5}$$

Substituting the relationship (1) into (5) the system of three linear equations is obtained, namely:

$$\begin{bmatrix}C_{11}-\rho c^2+C_{55}\alpha^2 & C_{16}+C_{45}\alpha^2 & (C_{13}+C_{55})\alpha\\ C_{16}+C_{45}\alpha^2 & C_{66}-\rho c^2+C_{44}\alpha^2 & (C_{36}+C_{45})\alpha\\ (C_{13}+C_{55})\alpha & (C_{36}+C_{45})\alpha & C_{55}-\rho c^2+C_{33}\alpha^2\end{bmatrix}\begin{Bmatrix}U_1\\ U_2\\ U_3\end{Bmatrix}=\begin{Bmatrix}0\\ 0\\ 0\end{Bmatrix} \tag{6}$$

In order to obtain the nontrivial solution of (6) the determinant of coefficient matrix has to be equal 0. It results in a sixth degree polynomial equation, namely:

$$A\alpha^6+B\alpha^4+C\alpha^2+D=0. \tag{7}$$

There are six real or complex roots of this equation, namely $\alpha_1 = -\alpha_2$, $\alpha_3 = -\alpha_4$ and $\alpha_5 = -\alpha_6$. Now, the components of displacement and stress can be written as follows:

$$(u_1,u_2,u_3)=\sum_{j=1}^{6}\left(1,V_j,W_j\right)U_{1j}e^{i\xi(x_1+\alpha_j x_3-ct)}, \tag{8}$$

$$(\sigma_{33},\sigma_{13},\sigma_{23})=\sum_{j=1}^{6}i\xi\left(D_{1j},D_{2j},D_{3j}\right)U_{1j}e^{i\xi(x_1+\alpha_j x_3-ct)} \tag{9}$$

where

$$\begin{aligned}&D_{1j}=C_{13}+C_{36}V_j+C_{33}W_j\alpha_j,\\ &D_{2j}=C_{55}\left(\alpha_j+W_j\right)+C_{45}V_j\alpha_j,\\ &D_{3j}=C_{45}\left(\alpha_j+W_j\right)+C_{44}V_j\alpha_j.\end{aligned} \tag{10}$$

$$\begin{aligned}&V_j=\frac{U_{2j}}{U_{1j}}=\frac{K_{13}(\alpha_j)K_{23}(\alpha_j)-K_{12}(\alpha_j)K_{33}(\alpha_j)}{K_{22}(\alpha_j)K_{33}(\alpha_j)-K_{23}(\alpha_j)K_{23}(\alpha_j)},\\ &W_j=\frac{U_{3j}}{U_{1j}}=\frac{K_{12}(\alpha_j)K_{23}(\alpha_j)-K_{13}(\alpha_j)K_{22}(\alpha_j)}{K_{22}(\alpha_j)K_{33}(\alpha_j)-K_{23}(\alpha_j)K_{23}(\alpha_j)}.\end{aligned} \tag{11}$$

The elements $K_{ik}(\alpha_j)$, $i,k = 1,2,3$ in Eq. (11) are the components of square matrix in relationship (6). Finally, relations (8), (9), (10) and (1) can be written in the matrix form:

$$\begin{Bmatrix}u_1\\ u_2\\ u_3\\ \sigma_{33}\\ \sigma_{13}\\ \sigma_{23}\end{Bmatrix}=\begin{bmatrix}1 & 1 & 1 & 1 & 1 & 1\\ V_1 & V_1 & V_3 & V_3 & V_5 & V_5\\ W_1 & -W_1 & W_3 & -W_3 & W_5 & -W_5\\ D_{11} & D_{11} & D_{13} & D_{13} & D_{15} & D_{15}\\ D_{21} & -D_{21} & D_{23} & -D_{23} & D_{25} & -D_{25}\\ D_{31} & -D_{31} & D_{33} & -D_{33} & D_{35} & -D_{35}\end{bmatrix}\begin{bmatrix}e^{i\xi\alpha_1 x_3} & 0 & 0 & 0 & 0 & 0\\ 0 & e^{i\xi\alpha_2 x_3} & 0 & 0 & 0 & 0\\ 0 & 0 & e^{i\xi\alpha_3 x_3} & 0 & 0 & 0\\ 0 & 0 & 0 & e^{i\xi\alpha_4 x_3} & 0 & 0\\ 0 & 0 & 0 & 0 & e^{i\xi\alpha_5 x_3} & 0\\ 0 & 0 & 0 & 0 & 0 & e^{i\xi\alpha_6 x_3}\end{bmatrix}\begin{Bmatrix}U_{11}e^{i\xi(x_1-ct)}\\ U_{12}e^{i\xi(x_1-ct)}\\ U_{13}e^{i\xi(x_1-ct)}\\ U_{14}e^{i\xi(x_1-ct)}\\ U_{15}e^{i\xi(x_1-ct)}\\ U_{16}e^{i\xi(x_1-ct)}\end{Bmatrix} \tag{12}$$

Marek Barski, Piotr Pająk DOI 10.1515/ama-2017-0019

4. STIFFNESS MATRIX METHOD

In order to avoid any numerical instabilities, which are the main disadvantages of the transfer matrix method, Kausel (1986), Wang and Rokhlin (2001) introduced the stiffness matrix method. Generally, SMM can be written as:

$$\begin{Bmatrix}\{\sigma\}_{k-1}\\ \{\sigma\}_k\end{Bmatrix} = [K]_k = [A]_k[B]_k{}^{-1} = \begin{bmatrix}[D]^- & [D]^+[H]^+\\ [D]^-[H]^- & [D]^+\end{bmatrix}\begin{bmatrix}[P_S]^- & [P_S]^+[H]^+\\ [P_S]^-[H]^- & [P_S]^+\end{bmatrix}^{-1}\begin{Bmatrix}\{u\}_{k-1}\\ \{u\}_k\end{Bmatrix} \tag{13}$$

where subscript *'k-1'* means the top surface of the *k-th* layer and subscript k means the bottom surface of the *k-th* layer. Matrices *[D]–, [D]+* contain the coefficients associated with stresses and matrices *[PS]–, [PS]+* represent the coefficients associated with displacements. These coefficients are described by relations (10) and (11). *[H]* denotes the diagonal matrix elements in equation (12). Finally, the matrices *[A]* and *[B]* take the following forms (Kamal and Giurgiutiu, 2014):

$$[A]_k = \begin{bmatrix} D_{11} & D_{13} & D_{15} & D_{11}e^{i\xi\alpha_1 d_k} & D_{13}e^{i\xi\alpha_3 d_k} & D_{15}e^{i\xi\alpha_5 d_k}\\ D_{21} & D_{23} & D_{25} & -D_{21}e^{i\xi\alpha_1 d_k} & -D_{23}e^{i\xi\alpha_2 d_k} & -D_{25}e^{i\xi\alpha_5 d_k}\\ D_{31} & D_{33} & D_{35} & -D_{31}e^{i\xi\alpha_1 d_k} & -D_{33}e^{i\xi\alpha_2 d_k} & -D_{35}e^{i\xi\alpha_5 d_k}\\ D_{11}e^{i\xi\alpha_1 d_k} & D_{13}e^{i\xi\alpha_3 d_k} & D_{15}e^{i\xi\alpha_5 d_k} & D_{11} & D_{13} & D_{15}\\ D_{21}e^{i\xi\alpha_1 d_k} & D_{23}e^{i\xi\alpha_3 d_k} & D_{25}e^{i\xi\alpha_5 d_k} & D_{21} & D_{23} & D_{25}\\ D_{31}e^{i\xi\alpha_1 d_k} & D_{33}e^{i\xi\alpha_3 d_k} & D_{35}e^{i\xi\alpha_5 d_k} & D_{31} & D_{33} & D_{35}\end{bmatrix} \tag{14}$$

$$[B]_k = \begin{bmatrix} 1 & 1 & 1 & e^{i\xi\alpha_1 d_k} & e^{i\xi\alpha_3 d_k} & e^{i\xi\alpha_5 d_k}\\ V_1 & V_3 & V_5 & V_1e^{i\xi\alpha_1 d_k} & V_3e^{i\xi\alpha_2 d_k} & V_5e^{i\xi\alpha_5 d_k}\\ W_1 & W_3 & W_5 & -W_1e^{i\xi\alpha_1 d_k} & -W_3e^{i\xi\alpha_2 d_k} & -W_5e^{i\xi\alpha_5 d_k}\\ e^{i\xi\alpha_1 d_k} & e^{i\xi\alpha_3 d_k} & e^{i\xi\alpha_5 d_k} & 1 & 1 & 1\\ V_1e^{i\xi\alpha_1 d_k} & V_3e^{i\xi\alpha_3 d_k} & V_5e^{i\xi\alpha_5 d_k} & V_1 & V_3 & V_5\\ W_1e^{i\xi\alpha_1 d_k} & W_3e^{i\xi\alpha_3 d_k} & W_5e^{i\xi\alpha_5 d_k} & -W_1 & -W_3 & -W_5\end{bmatrix} \tag{15}$$

In order to obtain the stiffness matrix for the whole composite material, an advanced recursive algorithm has to be applied (Rokhlin and Wang, 2002a). Let us consider two adjoining layers (1, 2), namely:

$$\begin{Bmatrix}\{\sigma\}_0\\ \{\sigma\}_1\end{Bmatrix} = \begin{bmatrix}[K]_{11}^A & [K]_{12}^A\\ [K]_{21}^A & [K]_{22}^A\end{bmatrix}\begin{Bmatrix}\{u\}_0\\ \{u\}_1\end{Bmatrix},\quad \begin{Bmatrix}\{\sigma\}_1\\ \{\sigma\}_2\end{Bmatrix} = \begin{bmatrix}[K]_{11}^B & [K]_{12}^B\\ [K]_{21}^B & [K]_{22}^B\end{bmatrix}\begin{Bmatrix}\{u\}_1\\ \{u\}_2\end{Bmatrix} \tag{16}$$

where subscripts denote the interfaces. By excluding *{σ}₁ and {u}₁* from the first relation and substituting in the second one, the matrix, which relates *{σ}₀ {u}₀* to *{σ}₂ {u}₂*, is obtained. This combined matrix is a stiffness matrix for these two bonded layers, namely:

$$\begin{Bmatrix}\{\sigma\}_0\\ \{\sigma\}_2\end{Bmatrix} = \begin{bmatrix}[K]_{11}^A + [K]_{12}^A([K]_{11}^B - [K]_{22}^A)^{-1}[K]_{21}^A & -[K]_{12}^A([K]_{11}^B - [K]_{22}^A)^{-1}[K]_{12}^B\\ [K]_{21}^B([K]_{11}^B - [K]_{22}^A)^{-1}[K]_{21}^A & [K]_{22}^B - [K]_{21}^B([K]_{11}^B - [K]_{22}^A)^{-1}[K]_{12}^B\end{bmatrix}\begin{Bmatrix}\{u\}_0\\ \{u\}_2\end{Bmatrix}. \tag{17}$$

Denoting the stiffness matrix obtained by $[K]^A$ and the stiffness matrix for the third layer by $[K]^B$, we can recursively apply the relation (17) to obtain the global stiffness matrix, which relates the stresses to the displacements for the top and bottom surface of the whole composite plate. The wave characteristic equation for the whole composite structure is obtained from the total stiffness matrix. Assuming that the components of stress on the top and bottom surface equal zero, in order to find the solution of (17), the determinant of the matrix 6x6 has to be computed.

5. NUMERICAL EXAMPLES

The dispersion curves are determined for thee different plates. The first plate consists of one layer, which is made of carbon fiber/epoxy resin, namely CFRP, Fibers T300, Matrix N5208. The total thickness of the plate is equal to d = 2 mm. The next plate consists of 8 layers with following stacking sequence [0°, 90°, 0°, 90°, 0°, 90°, 0°, 90°]. Each layer is made of identical material, namely carbon fiber/epoxy resin. The layers have also identical thickness d_k = 0.25 mm. Thus the total thickness of composite material is equal to d = 2 mm. The last plate is a hybrid composite, where the layers are as follows: [Al, 90°, 0°, 90°, 0°, 90°, 0°]. Al denotes aluminum alloy PA38 and the rest of layers are made of carbon fibers/epoxy resin. The thickness of aluminum alloy layer is equal to d_1=0.5mm. The rest layers have identical thickness d_k = 0.25 mm. The total thickness of the plate is also equal to d = 2 mm. The material properties of the aluminum alloy PA38 are: E = 69.5 GPa, ν = 0.33 and density ρ = 2700 kg/m³ and carbon fibers/epoxy resin lamina are: E_1 = 181 GPa, E_2 = 10.3 GPa, G_{12} = 7.17 GPa, ν_{12} = 0.28 and density ρ = 1.6 kg/m³. It is worth stressing here that the carbon layers are strongly orthotropic. It could cause some difficulties in numerical calculation. In order to find the solution of the studied problem an appropriate computer program is developed with the aid of SCILAB free software. In order to find the solution of the wave characteristic equation the bisection method is applied.

5.1. Single Lamina

In Fig. 3 there are shown the wave dispersion curves (phase and group velocities) obtained for a single lamina, where the waves propagate along the material principle direction x_1, φ = 0° (Fig. 1). In these figures the fundamental symmetric P_0, shear vertical SV_0 and shear horizontal SH_0 modes are highlighted.

DOI 10.1515/ama-2017-0019

Additionally, the four higher modes are present in the considered range of frequency. Unfortunately, the applied method does not allow the full identification of what kind of wave mods are. From the practical point of view the most important are the fundamental ones, namely P_0, SV_0, SH_0. The highest phase velocity is observed in the case of symmetric mod P_0, $c \approx 10660$ m/s. Moreover, its phase velocity is almost constant while the frequency is less then 500 kHz. For the greater frequency the significant change is observed. The SH_0 mod is constant in the whole studied range of frequency. To the contrary of the P_0 and SH_0 modes, the SV_0 one is strongly dispersive for the relatively small values of frequency. For frequency f = 400 kHz the phase velocity of this mode is also almost constant. It is worth noting that the all fundamental modes are convergent to the phase velocity equal to $c \approx$ 2000 m/s. Thus in the experiment for the sufficiently large frequency of the excited signal, the identification of these modes could be very difficult

In the Fig. 4 there are depicted the characteristic dispersion curves for the elastic waves, which travels in the direction which is perpendicular to the x_1 material principal direction, $\varphi = 90°$. Now the initial phase velocity of the P_0 symmetric fundamental mode is significantly smaller $c \approx 2540$ m/s due to the reduced stiffness of the lamina in this direction (E_2=10.5 GPa). The maximum value of the phase velocity in the case of the SV_0 mode is also reduced. The phase velocity of SH_0 mode is constant and identical as before. It is worth noting here that the number of higher modes is also changed. Now the seven higher modes are present in the considered range of frequency.

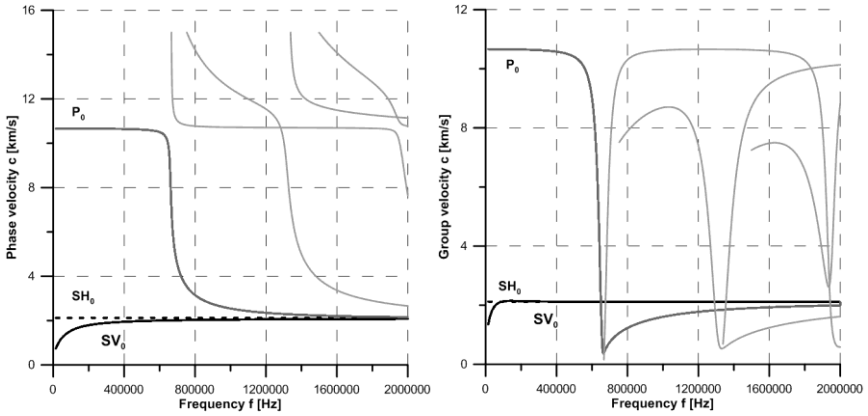

Fig. 3. Phase and group velocities. Single lamina, angle of waves propagation φ=0º

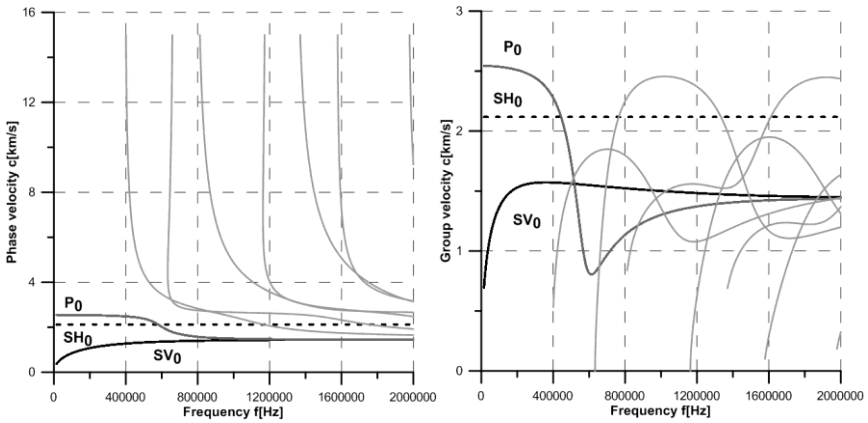

Fig. 4. Phase and group velocities. Single lamina, angle of waves propagation φ=90 º

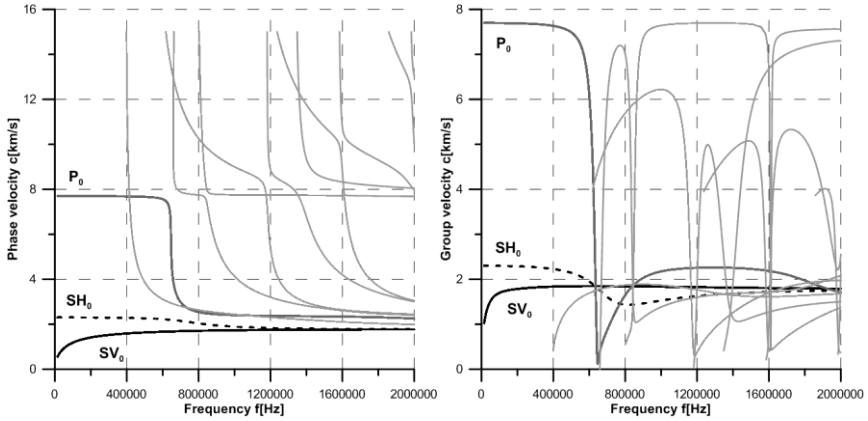

Fig. 5. Phase and group velocities. Single lamina, angle of waves propagation φ=45º

DOI 10.1515/ama-2017-0019

However quite different dispersion curves are obtained in the case of waves propagation angle φ = 45°, what is depicted in the Fig. 5. The initial (low frequency) phase velocity of the fundamental symmetric mode P_0 is equal to c ≈ 7700 m/s. Moreover, for frequency f ≈ 500 kHz as well as in the previous cases, the sudden change of the phase and group velocity is observed. The shear horizontal mode SH_0 is not constant any more. The slight variation is also observed. The initial SH_0 phase velocity is equal to c ≈ 2300 m/s. The shear vertical SV_0 is strongly dispersive for the low values of frequency. For the higher frequencies, great then f > 1.2 MHz the phase velocity of this mode is almost identical in comparison with SH_0 one. The most significant difference is observed in number of higher modes. Now ten higher modes are present. The first of them appears for the frequency equal to f ≈ 4 kHz. It is relatively low value of frequency in comparison with the previous cases. Finally, in Fig. 6 there are presented the relationships between the fundamental modes P_0, SH_0 and SV_0 and the waves propagation angle φ. These graphs are created for the fixed value of frequency f = 250 kHz. According to the authors of this work, the frequency equal to f = 250 kHz of the excitation signal is the most reasonable value from the practical point of view. The strongest dependency is observed in case of the symmetric mode P_0. The shear modes are not so sensitive on the wave propagation angle φ. It is worth noting that the SH_0 mode is almost insensitive on the angle φ. Moreover, the values of the phase and group velocities for assumed frequency are very similar.

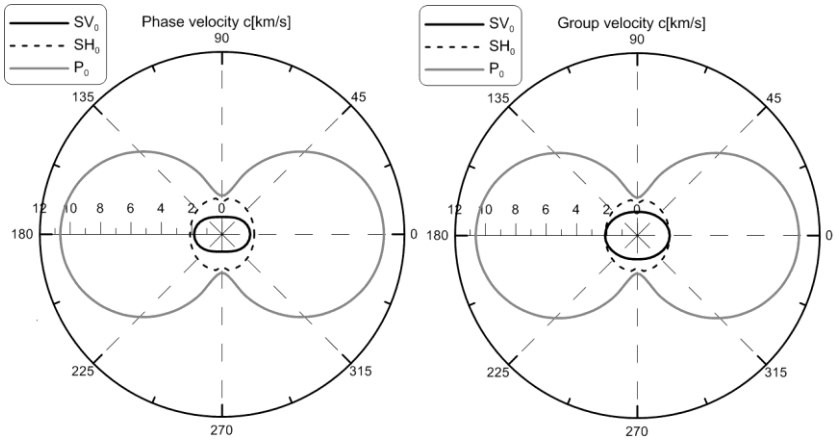

Fig. 6. Phase and group velocities with respect to angle of wave propagation. Fixed frequency f = 250 kHz.

5.2. Layered composite [0°, 90°, 0°, 90°, 0°, 90°, 0°, 90°]

In the case of the layered composite, when the waves propagation angle φ = 0°, the fundamental symmetric mode P_0 has initial phase velocity c = 7750 m/s. It is worth noting that this value is smaller in comparison with the initial phase velocity obtained in the case of single lamina. In contrast to the previously discussed cases, now this mode is slight dispersive in the initial range of frequency. For the frequency value f ≈ 500 kHz the sudden change is observed. Similar effect has been described in the case of a single lamina. For the frequency f > 1.2 MHz the mode P_0 is almost constant. The shear horizontal SH_0 mode is constant in the whole investigated range of frequency. Its phase velocity is equal to c = 2120 m/s. The shear vertical SV_0 mode is very similar to those, which are obtained for the single lamina. Additionally, seven higher modes are observed in the studied range of frequency. It should be stressed here that for the waves propagation angle φ = 90°, the obtained results are identical.

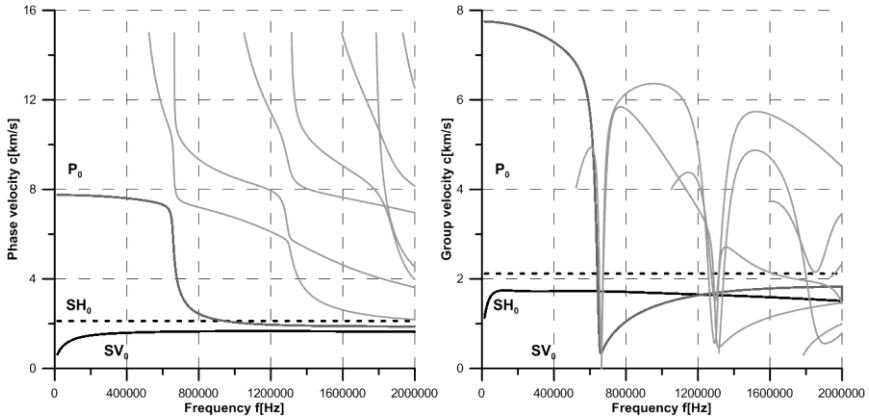

Fig. 7. Phase and group velocities. Layered composite [0°, 90°, 0°, 90°, 0°, 90°, 0°, 90°]. Angle of waves propagation φ = 0°, 90°

For the waves propagation angle φ = 45°, the obtained dispersion curves in the case of P_0 and SV_0 modes are similar to those, which are presented in the previous cases, what is depicted in Fig. 8. The initial phase velocity for P_0 mod is equal to c =

DOI 10.1515/ama-2017-0019

5950 m/s. However, behavior of the fundamental shear horizontal mode SH_0 is qualitatively different. It is rather similar to the P_0 mode. Additionally, its initial velocity c = 5400 m/s. For the frequency f > 1.2 MHz the sudden drop is visible, what remains the fundamental symmetric mode P_0 with frequency f > 500 kHz. It is also characteristic in the case of group velocities of modes P_0 and SH_0. The number of higher modes increases and now it is equal to eight. The shapes of the higher modes dispersion curves are also substantially different in comparison with those, which are presented in Fig. 7.

The phase and group velocities for the fixed frequency f = 250 kHz are presented in Fig. 9. It should be stressed here that the these graphs are also substantially different in comparison with those which are presented in Fig. 6. The shear vertical mode SV_0 seems to be insensitive on the waves propagation angle φ. The symmetric mode P_0 varies not significantly with respect to this parameter. However the phase and group velocity of the shear horizontal mode SH_0 strongly depends on the angle φ. For the values of the angle φ equal to 45°, 135°, 225° and 315° the discussed velocities have the highest values. The maximal value of the phase velocity is over two times larger in comparison with the minimal one.

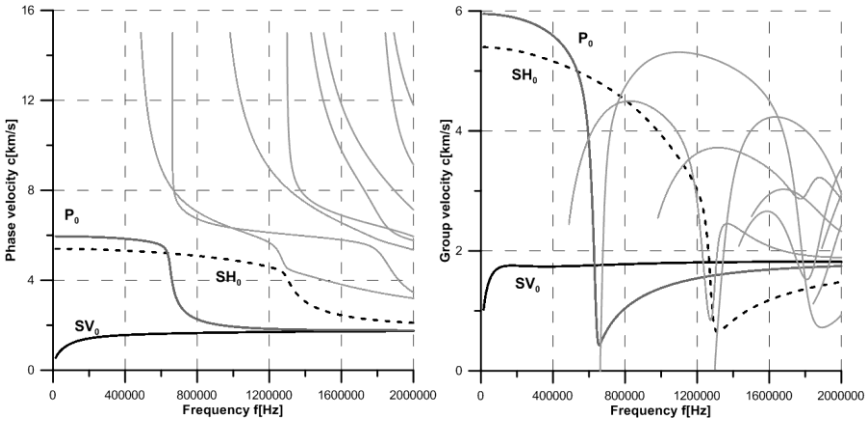

Fig. 8. Phase and group velocities. Layered composite [0°, 90°, 0°, 90°, 0°, 90°, 0°, 90°]. Angle of waves propagation φ = 45°

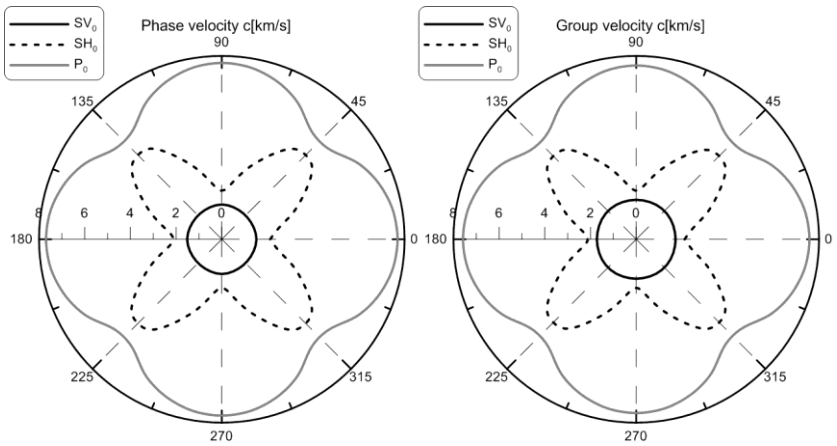

Fig. 9. Phase and group velocities with respect to angle of wave propagation. Fixed frequency f = 250 kHz. Layered composite [0°, 90°, 0°, 90°, 0°, 90°, 0°, 90°]

5.3. Hybrid composite [Al, 90°, 0°, 90°, 0°, 90°, 0°]

It should be stressed here that in the previously presented cases there has been no any numerical instabilities and the reliable numerical solution of the wave characteristic equation can be always obtained. Unfortunately, in the case of hybrid composite the dispersion curves are determined only for the waves propagation angle φ = 0°. In the case of the other values of φ the problems are met even in estimation of the fundamental modes SH_0 and P_0. According to the authors experience it could be caused by the fact that these modes are very close to each other and it is impossible to extract them. Additionally, there is a significant difference between the Young's modulus of the aluminum alloy and carbon fibers. This difference could cause some disturbances with propagation of elastic waves through the interface of aluminum layer and carbon fiber layer.

In Fig. 10 there is presented the dispersion curves. These curves are computed for the waves propagation angle φ = 0°. Generally, the obtained curves are similar to those which are presented above. The initial value of the phase velocity of the symmetric mode P_0 is equal to c = 6990 m/s. The shear horizontal mode SH_0 slightly varies with respect to the frequency. However, the group velocity of this mode for frequency equal to f = 1.48 MHz suddenly changes. The shear vertical mode SV_0 is very regular and it remains the curves, which are presented above. Besides, there are nine higher modes. To the contrary to previously presented cases, now it possible to identify the higher shear horizontal modes, namely from SH_1 to SH_4.

DOI 10.1515/ama-2017-0019

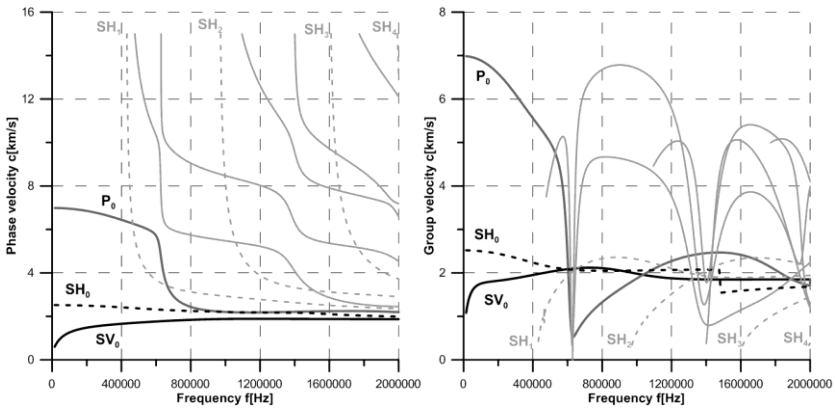

Fig. 10. Phase and group velocities. Hybrid composite [Al, 90°, 0°, 90°, 0°, 90°, 0°]. Angle of waves propagation φ = 0°

6. CONCLUSIONS

In the present work the dispersion curves are estimated for a different composite materials, namely: single lamina, multilayered composite with quasi - isotropic mechanical properties and hybrid composite material. In the case of single lamina and quasi - isotropic composite all layers are made of carbon fiber/epoxy resin. In the latter case, the investigated material consists of carbon fiber/epoxy resin and single layer, which is made of aluminum alloy Pa38. The main conclusion is that if the all layers of studied composite are made of identical material, the stiffness matrix approach in an effective tool for determining the dispersion curves. It is relatively simple and easy to use in comparison with other method, like transfer matrix method or global matrix method. However, if the composite contains the layers, which are made of different materials, the obtaining of dispersion curves could be very difficult or even impossible. According to the authors experience, this effect is caused by the significant difference between the mechanical properties of the layers (the values of Young's modulus). Generally, the shape and the number of elastic wave modes, which are present in the investigated range of frequency, strictly depends on the mechanical properties of the whole composite structure as well as on the waves propagation angle φ. For the angle φ different than 0° and 90°, the number of higher modes is the largest. Qualitatively, the behavior of the fundamental modes are similar in all investigated cases. For the low frequency the highest phase and group velocity has always the symmetric mode P_0.

REFERENCES

1. **Barski M., Pająk P.** (2016), An application of stiffness matrix method to determining of dispersion curves for arbitrary composite materials, *Journal of KONES Powertrain and Transport*, 23(1), 47-54.
2. **Giurgiutiu V.** (2008), *Structural Health Monitoring with Piezoelectric Wafer Active Sensors*, Elsevier.
3. **Haskell N.A**. (1953), Dispersion of surface waves on multilayer-media, *Bulletin of the Seismological Society of America*, 43, 17- 34.
4. **Hawwa M.A., Nayfeh H.A.** (1995), The general problem of thermoelastic waves in anisotropic periodically laminated composites, *Composite Engineering*, 5, 1499- 1517.
5. **Kamal A., Giurgiutiu V.** (2014), Stiffness Transfer Matrix Method (STMM) for Stable Dispersion Curves Solution in Anisotropic Composites, *Proc. of SPIE*, Vol. 9064.
6. **Kausel E.** (1986), Wave propagation in anisotropic layered media. *International Journal for Numerical Methods in Engineering,* 23, 1567-1578.
7. **Knopoff L.** (1964), A matrix method for elastic waves problems. *Bulletin of the Seismological Society of America*, 43, 431-438.
8. **Lowe J.S.M.** (1995), Techniques for Modeling Ultrasonic Waves in Multilayered Media, *IEEE Transactions on Ultrasonics, Ferroelectric and Frequency Control,* 42, 525-542.
9. **Nayfeh A.H.** (1991), The general problem of elastic wave propagation in multilayered anisotropic media, *Journal of the Acoustic. Society of America*, 89, 1521- 1531.
10. **Pant S., Laliberte J., Martinez M, Rocha B.** (2014), Derivation and experimental validation of Lamb wave equations for an n - layered anisotropic composite laminate, *Composite Structure*, 111, 566-579.
11. **Pavlakovic B., Lowe M.** (2003), *DISPERSE Manual*, Imperial College, London.
12. **Press F., Harkrider D., Seafeldt C.A.** (1961), A fast convenient program for computations of surface - wave dispersion curves in multilayered media, *Bulletin of the Seismological Society of America*, 51, 495- 502.
13. **Randall M.J.** (1967), Fast programs for layered half - space problems*, Bulletin of the Seismological Society of America*, 57, 1299-1316.
14. **Rokhlin S.I., Wang L.** (2002a), Stable recursive algorithm for elastic wave propagation in layered anisotropic media: Stiffness matrix method, *Journal of the Acoustic Society of America*, 112, 822-834.
15. **Rokhlin S.I., Wang L.** (2002b), Ultrasonic waves in layered anisotropic media: characterization of multidirectional composites, *International Journal of Solids & Structures,* 39, 5529- 5545.
16. **Royer D., Dieulesaint E.** (2000), *Elastic Waves in Solids*, Springer.
17. **Schmidt H., Tango G.** (1986), Efficient global matrix approach to the computation of synthetic seismograms, *Geophysical Journal of Royal Astronomical Society,* 84, 331- 359.
18. **Schwab F.A.** (1970), Surface - wave dispersion computations: Knopoff's method, *Bulletin of the Seismological Society of America*, 60, 1491- 1520.
19. **Sorohan S., Constantin N., Gavan M., Anghel V.** (2011), Extraction of dispersion curves for waves propagating in free complex waveguides by standard finite element codes, *Ultrasonics*, 51, 503-515.
20. **Thomson W. T.** (1950), Transmission of elastic waves through a stratified solid medium. *Journal of Applied Physics*, 21, 89-93.
21. **Wang L., Rokhlin S.I.** (2001), Stable reformulation of transfer matrix method for wave propagation in layered anisotropic media, *Ultrasonics*, 39, 413-424.

Acknowledgement: The research project has been financed by National Science Center of Poland pursuant to the decision No. DEC-2013/09/B/ST8/00178.

DE GRUYTER
OPEN

DOI 10.1515/ama-2017-0020 acta mechanica et automatica, vol.11 no.2 (2017)

FRICTION EVALUATION OF LASER TEXTURED TOOL STEEL SURFACES

Jana ŠUGÁROVÁ*, Peter ŠUGÁR*, Martin FRNČÍK*

*Slovak University of Technology, Faculty of Material Science and Technology, Institute of Production Technologies, J. Bottu 25, 917 24 Trnava, Slovakia

jana.sugarova@stuba.sk, peter.sugar@stuba.sk, martin.frncik@stuba.sk

received 2 November 2015, revised 12 May 2017, accepted 17 May 2017

Abstract: Surface textures can be defined as a regularly arranged micro-depressions or grooves with defined shape and dimensions. These textures, if they are manufactured by laser ablation process, contribute to a significant improvement of the tribological, optical or various biological properties. The aim of this paper is to analyze the influence of the surface textures prepared by laser surface texturing (LST) at the friction coefficient value measured on the tool (90MnCrV8 steel) – workpiece (S235JRG1 steel) interface. Planar frontal surfaces of compression platens have been covered by parabolic dimple-like depressions with different dimensions. The morphological analysis of such manufactured depressions has been performed by laser scanning microscopy. Influence of such created textures on the tribological properties of the contact pair has been analyzed by the ring compression test method in the terms of hydrodynamic lubrication regime. The experimental research shown that by applying of surface textures with defined shape and dimensions and using an appropriate liquid lubricant at the same time, the coefficient of contact friction can be reduced nearly to the half of its original value.

Key words: Laser Surface Texturing, Dimple-Like Depressions, Friction Coefficient, Lubrications, Ring – Test

1. INTRODUCTION

Steels are representative structural materials for most mechanical applications because of their high strength and toughness, good machinability and relatively low cost. Surface hardness and chemical composition of applied coating play a dominant role against wear under sliding conditions. The efficiency, reliability, and durability of mating mechanical components depend on friction occurring at the interface during the sliding (Gualtieri et al., 2009). The surface texture and geometry are the key factors which determine the functionality of the surface. The idea of using surface texturing for improving tribological performance is not a new development (Ibatan et al., 2015). A general classification on the methods to produce surface texture can be made as bottom to top and top to bottom (Demir et al., 2013). The methods involving bottom to top strategies are the ones, where the surface is usually deposited with chemical/physical process in the form of a coating or surface is generated layer by layer. The dimensional scale of the patterns can reach the nanometric level. On the other hand, top to bottom methods based on material removal from an initial surface are potentially more flexible. Top to bottom methods involve techniques such as grinding and honing (Jeng, 1996), chemical etching (Rech et al., 2002), electron ion etching (Zhu et al., 2003), electric-discharge machining (Aspinwall et al., 1996), laser beam machining (Etsion, 2005), micro-casting (Cannon and King, 2009) and micro-ball end milling (Yan et. al., 2010).

According to the Ibatan et al. (2015) LST is one of the most advanced techniques in producing of micro-dimple patterns for sliding contacts. The laser used is extremely fast, allowing short processing times. It provides high precision control of the size and shape, enabling the construction of optimized geometrical parameters and can be used for a wide range of materials including metals, ceramics and polymers. The texturing process involves focused pulsed laser to produce micro-dimple patterns surrounded by a solidified melt rim. Due to high energy involved with LST, material melting and vaporization occur, leading to heat affected zones (HAZ) on the solidified melt rim, and hence changing the local microstructures and mechanical properties. To minimize the microstructural changes and size of solidified melt rim, appropriate pulse energy and pulse frequency can be modified (Vilhena et al., 2009). Lasers commonly used on LST are CO2 and Nd:YAG (Schaeffer, 2012). Currently, laser systems applied in production of surface textures operates with pulse duration at the femtosecond level (Stašić, 2011).

The use of a laser beam allows direct writing of the texture patterns, use of masks (Ortabasi et al., 1997), or diffractive optics (Huang et al., 2010) to generate patterns on the surface. Direct writing with the laser beam is the most flexible among the listed, since the same optical chain can be manipulated to work on different materials and patterns. A single tool for flexible machining conditions which can be adapted to different applications is an attractive solution for industrial use (Demir et al., 2013).

Surface texturing can be obtained by protrusions or dimples. Dimple configuration is more popular, especially in elasto-hydrodynamic and boundary lubrication regimes. For protruded surface texturing, contact area between the surface and the protruded geometry is much larger in comparison with dimpled surface, resulting in higher average contact pressure and higher wear rates (Ibatan et al., 2015). The aim of micro-texturing is either to increase or to decrease friction (Braun et al., 2014). Textures, like channels or crossed channels are reported to do both, increase (Zum Gahr et al., 2009; Wahl et al., 2012) or decrease (Costa and Hutchings, 2009) friction, depending on the tribological conditions. Furthermore, for textures like dimples the effect to reduce friction is reported, especially under hydrodynamic lubrication conditions (Etsion, et al., 1999; Etsion, 2005). Four mechanisms are postulated in the literature, which might lead to the reduction in friction and wear by micro-dimples: (i) the trapping of wear debris (Varen-

DOI 10.1515/ama-2017-0020

berg et al., 2002), (ii) changes in the contact angle (Ma et al., 2013), (iii) the storage of lubricant (Lu and Khonsari, 2007) and (iv) a micro-hydrodynamic pressure build-up (Scaraggi, 2012).

The geometry and dimensions of surface texture vary in shapes and sizes from a few microns to hundreds of microns. Typical texture shapes (protruded and recessed) involved are circular, square, triangle, and hexagon, but different patterns of microgrooves are also studied (Ibatan et al., 2015). Circular dimple-like depressions are still the most commonly used geometrical pattern due to their easy fabrication and low cost (Yan et al., 2010). There are three major parameters involved with surface texturing, such as dimple shape, dimple depth and dimple density (Ma and Zhu, 2011; Ronen et. al., 2001). By considering all the geometric parameters, texture shapes are optimized to achieve the optimum shapes which will provide the best tribological performance in terms of minimum friction and maximum load carrying capacity (Sheen and Khonsari, 2015; Qiu et al., 2013). It has been found that the optimum geometry for each shape is not identical but similar, and the regular shape such as ellipse with round or curved edge is shown to reduce the friction and increase load carrying capacity significantly as compared to other shapes (Ibatan et al., 2015). Fig. 1 demonstrates important geometries of a surface texture and regular texture shapes currently studied by researchers. Except the above mentioned parameters, geometries such as bottom shape profile, orientation of surface texture to sliding direction, and cellular arrangement of surface texture are counted in key texture parameters too. It is emphasized that surface texturing may have negative effects on the tribological performance of a sliding couple if the surface texture is not optimized (Mourier et al., 2006).

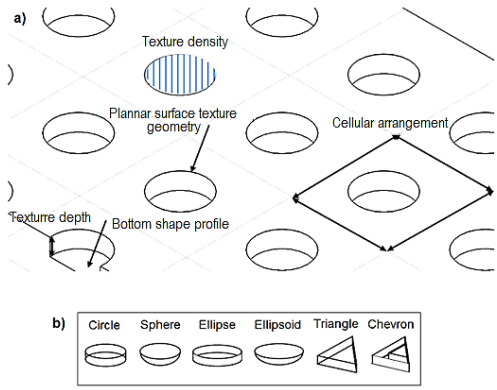

Fig. 1. Surface texture geometry; (a) key geometrical parameters of a surface texture, (b) shapes of dimples (Ibatan et al., 2015)

The applications of LST encompass the ones requiring improved tribological (Etsion, 2005), biomedical (Samad-Zadeh et al., 2011), and optical (Iyengar et al., 2011) properties; as well as control of surface wetting (Bizi-Bandoki et al., 2011), and improvement of adhesion joint strength (Man et al., 2010). Various pulsed laser systems operating in different pulse regimes with wavelengths varying from IR to UV are employed for different texturing applications (Schaeffer, 2012).

2. EXPERIMENTAL SETUP

The aim of this paper is to analyze the influence of the surface textures prepared by LST on the friction coefficient value, which was measured at the tool – workpiece interface. Contact pair consists of a pair of compression platens (upper and lower one); among them the test sample is axially compressed. Frontal areas of each compression platen have been covered by a texture of defined shape and dimensions. There were used a four pairs of compression platens in the experiment; their frontal areas were modified by regularly arranged micro-dimples:

(**A**) dimples with a diameter of 100 μm and a depth of 10 μm produced by hatching machining strategy,

(**B**) dimple diameter of 100 μm and the depth of 10 μm produced by caving machining strategy,

(**C**) dimple diameter of 100 μm and the depth of 40 μm produced by hatching machining strategy and

(**D**) dimple diameter of 100 μm and the depth of 40 μm produced by caving machining strategy.

Surface density of the studied textures makes approximately 6%. Each texture consists of dimple-like depressions with a diameter of a 100 μm. Depressions are situated at the corners of the regular hexagon with a side length of 400 μm. One depression is placed into the center of this formation, as demonstrates Fig. 2a. Fig. 2b illustrates an ideal profile of depression of both studied depth (10 μm and 40 μm).

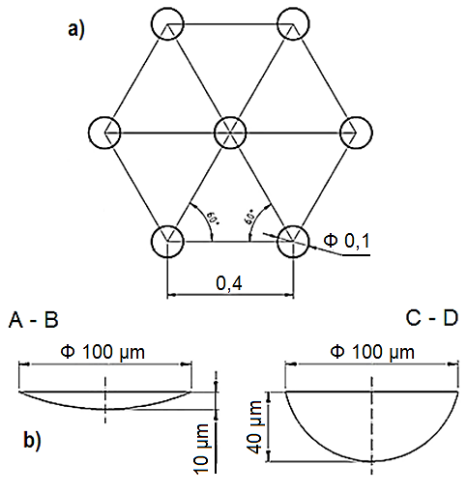

Fig. 2. Studied textures; (a) deployment of depressions in the basic formation; (b) ideal profile of studied depressions

Compression platens were manufactured of 90MnCrV8 steel according to EN ISO 4957, since this type of material is widely applied in production of blank metal forming tools. Chemical composition of this tool steel is specified in Tab. 1. Hardening of manufactured tools to desired hardness of 53 – 55 HRC had gone before the production of defined textures on the frontal areas of these tools. Subsequently, the frontal areas were grinded to obtain a surface roughness (Ra) of 0.4 μm, then textured by laser beam.

To manufacture surface textures on the frontal areas of compression plates a 5-axis high precision laser machining centre LASERTEC 80 Shape has been used. This machine is equipped with a pulsed fiber Nd:YAG laser with a wavelength of 1064 nm. Tab. 2 contains a description of the laser beam parameters used to produce the surface textures. These parameters had been optimized in order to a depth of cut of 1 μm per a layer was achieved.

DOI 10.1515/ama-2017-0020

Tab. 1. Chemical composition of tool steel (Preciz, 2012)

C [wt %]	Si [wt %]	Mn [wt %]	P max [wt %]	S max [wt %]	Cr [wt %]	V [wt %]
0.85 -0.95	0.10 - 0.40	1.90 - 2.10	0.030	0.030	0.20 -0.50	0.05 -0.15

Tab. 2. Parameters of laser beam utilized to production of micro-dimples

Parameter	Value
Power *P* (W)	10.075
Scanning speed v_s (mm/s)	1200
Repetition rate (kHz)	60
Pulse duration t_p (ns)	120

Fig. 3 demonstrates the result of laser beam machining process – tool for compression test whose frontal area is covered by texture D. Total textured area makes 256 mm2 (a square with a side length of 16 mm).

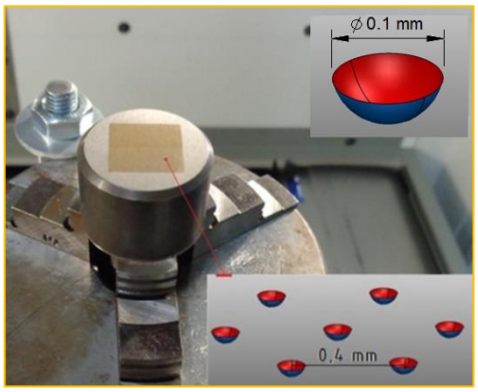

Fig. 3. Tool for compression test with frontal area covered by texture D

In order to determine the real shape and dimensions of such manufactured surface depressions a morphological analysis has been performed. This analysis of chosen depression of each surface texture's type has been performed using a laser confocal microscope Zeiss LSM 700 (with resolution of 0.12 μm). Fig. 4 shows a real 3D shapes and dimensions of analyzed dimples of each studied texture, which were manufactured by two different machining strategies.

The same figure shows that around the edge of each depression a rim of solidified melt was created. This rim is a typical element of the structures manufactured by laser beam in a material ablation processes. More or less, this negative effect can be minimalized by optimizing the parameters of laser beam with a subsequent polishing of textured surfaces.

To determine the friction coefficient of the contact pair a ring compression test was performed. During this test a ring-shaped test sample is axially compressed among the pair of compression platens; test samples were manufactured of S235JRG1 steel (EN 10027-1). Chosen steels represent and simulate the contact materials (forming tool and the formed component) of the real specific metal forming process. Tab. 3 documents the chemical composition of material of test samples. This test is based on the assumption that the friction coefficient is constant at the whole contact surface and the deformation of the test ring is homogeneous. During this compression, the hole diameter of the test sample can be reduced, remain without a change or even increased (depending on the size of the friction coefficient). When the test sample is compressed in frictionless conditions, the hole diameter increases proportionally with the increase of the outer diameter. With the friction growth the increase of hole diameter is hampered and at a certain size of radial pressure this diameter can be reduced (Plančak, 2012). The ratio of outer diameter to the hole diameter to the height of test sample D *: d : h* is equal to 6 : 3 : 2. The dimensions of test samples are typically 12 mm : 6 mm : 4 mm according to this ratio. Frontal areas of test samples were non-textured; what is more, these surfaces had been grinded to obtain a required surface roughness (Ra) of 0.4 μm. It is important to preserve approximately an equal compression of test sample *ΔH* during the test; its value should be in the interval from 0.2 to 0.5 mm.

Tab. 3. Chemical composition of test samples (CZ Ferro-Steel, 2011)

C max [wt %]	Mn [wt %]	Si [wt %]	P max [wt %]	S max [wt %]	N max wt %]	Al [wt %]
0.17	-	-	0.045	0.045	0.007	-

Tab. 4. Physical and chemical properties of applied liquid lubricants

Variocut C 462	
A high performance and heavy-metal free neat cutting oil.	
Physical and chemical properties	
Appearance	yellow liquid
Viscosity at 40 °C (mm^2/s)	22 (according DIN 51 562)
Density 15 °C (kg/m^3)	908 (DIN 51 757)
Flash point (°C)	164 (ISO 2592)
Iloform FST 4	
A medium viscosity, neat forming oil containing high levels of advanced lubricity and extreme pressure additives. It is free of chlorine and heavy metals (such as Barium).	
Physical and chemical properties	
Appearance	dark brown liquid
Viscosity at 40 °C (mm^2/s)	120 (according to DIN 51 562)
Density at 20 °C (kg/m^3)	< 1000 (DIN 51 757)
Flash point (°C)	144 (ISO 2592)

Friction coefficient evolution was recorded in a hydrodynamic lubrication regime; two types of liquid lubricants were used to ensure this “full lubrication” configuration at the contact interface: a mineral VarioCut C462 oil and Iloform FST4 oil, physical and chemical properties of applied lubricants are depicted in Tab. 4. Both non-textured and textured compression platens were tested for comparison.

DOI 10.1515/ama-2017-0020

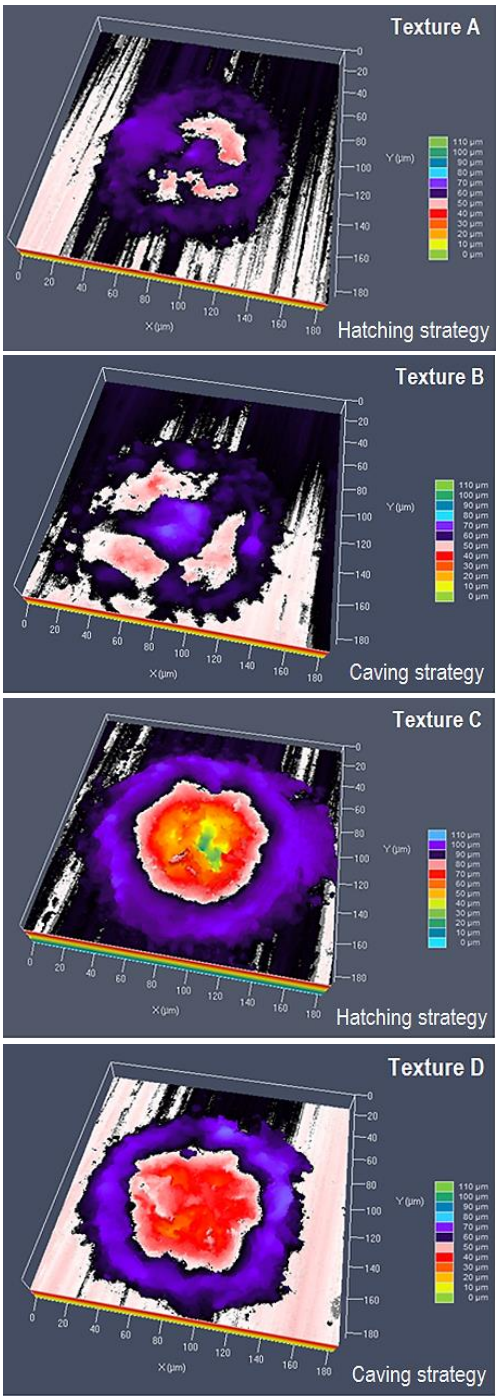

Fig. 4. Real 3D shapes of chosen depression of each studied surface textures

3. RESULTS AND DISCUSSION

Single friction coefficients obtained through a ring compression test, measured in various combination of surface texture with/without a lubricant, are specified in Tab. 5. Two test samples (8 test samples compressions) have been used for analysis of each combination of input parameters from Tab. 5. Reference value (shown in red) is represented by experiment no. 13; contact surfaces were non-textured in lubrication-free friction regime, friction coefficient f_{13} got at 0.275±0.015 value. This value is in accordance with the Engineering ToolBox (2014); where the friction coefficient attains value from 0.25 to 0.8 for a steel – steel contact pair.

Tab. 5. Design of experiment and obtained friction coefficients

Experiment	Texture	Lubricant	Coefficient of friction (-)
1.	A	-	0.18 ± 0.013
2.		Variocut C462	0.18 ± 0.005
3.		Iloform FST 4	0.21 ± 0.010
4.	B	-	0.26 ± 0.010
5.		Variocut C462	0.22 ± 0.005
6.		Iloform FST 4	0.22 ± 0.012
7.	C	-	0.26 ± 0.013
8.		Variocut C462	0.23 ± 0.014
9.		Iloform FST 4	0.18 ± 0.001
10.	D	-	0.25 ± 0.010
11.		Variocut C462	0.16 ± 0.009
12.		Iloform FST 4	0.15 ± 0.001
13.	-	-	0.275 ± 0.015

Friction coefficients values are depicted in Fig. 5 in relation to the reference value. In all executed experiments friction coefficients reached a lower value than the reference value (if the values of standard deviations are neglected). There are an individual friction conditions distinguished by a color in this figure (grey shades for lubricant-free regime, green shades for Variocut C 462 and blue shades for Iloform FST 4). The influence of defined surface textures on the friction coefficient value in lubrication-free regime is meaningless in the experiments no. 4 (friction reduction of only 5.5 %), no. 7 (friction reduction of only 5.5 %) and no. 10 (friction reduction of 9.1 %), because the friction coefficient values in these experiments are similar to the reference value. It means, these defined surface textures do not contribute to reducing the friction coefficient at the analyzed tool - workpiece interface in the lubrication-free regime. The exception has been observed in the experiment no. 1, when applied surface texture contributed to the reduction of friction, friction coefficient value decreased to f_1 = 0.18 (35 % friction reduction compared to the reference value).

Horizontally hatched columns in Fig. 5 demonstrate the friction coefficient values obtained in the experiments where the Variocut C462 lubricant has been used to ensure the hydrodynamic friction regime. The largest reduction of friction has been observed in the experiment no. 11 (Texture D + Variocut C462) with the friction coefficient value of 0.16 (42 % friction reduction). Friction reduction has been successfully observed in other experiments too – experiment no. 2 with the friction coefficient value f_2 = 0.18 (35 % friction reduction), which is substantially the same value as in the experiment no. 1 (surface texture A in lubrication-free regime, f_1 = 0.18); which means, applied liquid lubricant does not contribute to reducing of friction, reducing of friction coefficient is probably achieved by applying of surface Texture A. In experiment no. 5 friction coefficient of 0.22 has been measured and in experiment no. 8 the friction coefficient 0.233 has been observed (friction reduction of 20 %, resp. of 16.4 %).

Double diagonally hatched columns in Fig. 5 depict the friction coefficient values obtained in the experiments where the Iloform FST4 lubricant has been used. During the ring compression test execution an undesirable phenomenon was observed – there was

DOI 10.1515/ama-2017-0020

a high adhesion of test sample to the upper compression platen. This phenomenon came into existence as a result of high lubricant viscosity (see Tab. 4). A combination of surface Texture D with liquid lubricant Iloform FST 4 in experiment no. 12 achieved the lowest friction coefficient value (f_{12} = 0.15) of all performed experiments (46 % friction reduction).

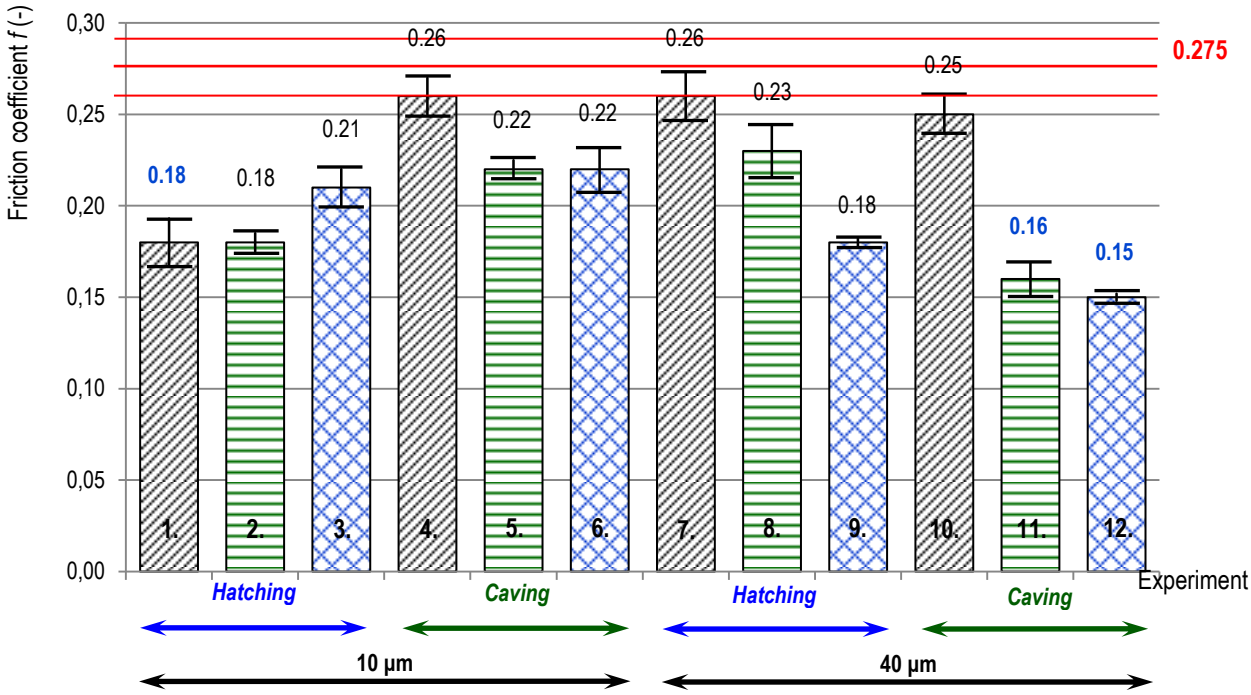

Fig. 5. Graphical comparison of obtained friction coefficients in a relation to the reference value

Tab. 6. Friction coefficient values relative to the defined surface texture and applied liquid lubricant

	Texture A	Texture B	Texture C	Texture D	Reference sample	Friction reduction
No lubricant	**0.18**	0.26	0.26	0.25	0.275	*35 %*
Variocut C462	0.18	0.22	0.23	**0.16**		*42 %*
Iloform FST4	0.21	0.22	0.18	**0.15**		*46 %*

The machining strategy is an important factor that significantly affects the desired shape and dimensional accuracy of produced surface dimple-like depressions. The influence of machining strategy on the tribological properties of contact surfaces (friction coefficient in particular) is observed for both types of textures and all tribological regimes. If a shape and dimensional accuracy of Texture C (hatching strategy) and Texture D (caving strategy) is compared, we can see that hatching machining strategy contributed to the production of shape and dimensionally more accurate depressions than in caving strategy, but the better tribological behaviour has been observed in Texture D (when both lubricants were applied). The reason is that by caving machining strategy a more favorable dimple diameter to the dimple height ratio d_p/h_p was achieved (in this case the value of the ratio is circa 0.18), whereas the value of the ratio is circa 0.32 for Texture C. The optimal value of the ratio can be found in the interval from 0.1 to 0.2, according to Ronen et al. (2001).

Tab. 6 demonstrates the friction coefficient values relative to the reference value when various surface textures and lubricants were applied to modify the tribological conditions of contact surfaces. There are also marked the lowest friction coefficient values which were measured in single friction conditions.

4. CONCLUSION

According to Tang et al. (2013) surface texturing is a widely used approach to improve the load capacity, the wear resistance, and the friction coefficient of tribological mechanical components. Laser surface texturing with a parabolic dimple-like depressions with depths of 10 µm and 40 µm and diameter of 100 µm and a textured area of 6 % has been applied to 90MnCrV8 steel frontal area in order to analyze the influence on the friction coefficient measured at the tool – workpiece interface. Laser texturing has been performed using a pulsed fiber Nd:YAG laser with pulse duration of 120 ns. Two different machining strategies were applied in production of surface textures in order to find which strategy produces shape and dimensional more precise micro-dimples. The morphological characterization of ablated surfaces has been performed using laser confocal microscopy technique. Tribological tests have been performed in hydrodynamic lubrication configuration, where two different types of liquid lubricants were applied at room temperature.

Results confirmed the influence of machining strategy on the geometrical parameters of produced dimples and the impact on friction behavior of the surface. Also significant improvement of friction behavior under lubricate conditions has been observed. Textured contact surface modified by Iloform FST4 lubricant showed better friction behavior than reference surface. Reference value corresponding to a non-treated surface was established at 0.275±0.015. Friction coefficient was in this case reduced to 0.15 value (the best friction coefficient reduction of 46 %), which

DOI 10.1515/ama-2017-0020

means, that by applying of surface textures with defined shape and dimensions and using an appropriate liquid lubricant at the same time, the coefficient of contact friction can be reduced nearly to the half of its original value. The surface texturing is important in reducing friction and wear. The generation of hydrodynamic pressure, the function of micro-trap for wear debris, and the micro-reservoirs for lubricant retention are the main mechanisms responsible for reducing the friction and wear in this method of surface treatment.

Presented results give answer on the questions regarding the influence of laser texture machining parameters and lubrication of laser textured surfaces on the friction behavior. In the experiments only planar surfaces have been evaluated. More complicated situation arises in the case where a complex shaped surface is used.

REFERENCES

1. **Aspinwall D.K., Wise M.L.H., Stout K.J. et al.** (1996), Electrical discharge texturing, *Int. Journal of Machine Tools & Manufacture*, 32(1-2), 183-193.
2. **Bizi-Bandoki P., Benayoun S., Valette S. et al.** (2011), Modifications of roughness and wettability properties of metals induced by femtosecond laser treatment, *Applied Surface Science*, 257(12), 5213-5218.
3. **Braun D., Greiner Ch., Schneider J. et al.** (2014), Efficiency of laser surface texturing in the reduction of friction under mixed lubrication, *Tribology international,* 77*,* 142-147.
4. **Cannon A.H., King W.P.** (2009), Casting metal microstructures from a flexible and reusable mold, *Journal of Micromechanics and Microengineering,* 19, 1-6.
5. **Costa H.L., Hutchings I.M.** (2009), Effects of die surface patterning on lubrication in strip drawing, *Journal of Materials Processing Technology,* 209(3), 1175-1180.
6. **CZ Ferro-Steel** (2011), *ČSN 11373 – non-alloy steel for construction purposes (*http://www.czferrosteel.cz/pdf/tyce-11373.pdf)
7. **Demir A.G., Maressa P., Previtali B.** (2013), Fibre laser texturing for surface functionalization, *Physics Procedia,* 41, 759-768.
8. **Etsion I.** (2005), State of the art in laser surface texturing, *Journal of Tribology*, 127(1), 248-253.
9. **Etsion I., Kligerman Y., Halperin G.** (1999), Analytical and experimental investigation of laser-textured mechanical seal faces, *Tribology Transactions*, 42(3), 511-516.
10. **Gualtieri E., Borghi A., Calabri L. et al.** (2009), Increasing nanohardness and reducing friction of nitride steel by laser surface texturing, *Tribology International,* 42(5), 699-705.
11. **Huang J., Beckemper S., Gillner A. et al.** (2010), Tunable surface texturing by polarization-controlled three-beam interference, *Journal of Micromechanics and Microengineering*, 20(9), p. 095004.
12. **Ibatan T., Uddin M.S. and Chowdbury M.A.K.** (2015), Recent development on surface texturing in enhancing tribological performance of bearing sliders, *Surface & coatings Technology*, 272, 102-120.
13. **Iyengar V.V., Nayak B.K., Gupta M.C.** (2011), Ultralow reflectance metal surfaces by ultrafast laser texturing, *Applied Optics*, 49(31), 5983-5988.
14. **Jeng Y-R**. (1996), Impact of Plateaued Surfaces on Tribological Performance, *Tribology Transactions*, 39(2), 354-361.
15. **Lu X., Khonsari M.M.** (2007), An experimental investigation of dimple effect on the Stribeck curve of journal bearings, *Tribology Letters*, 27(2), 169-176.
16. **Ma Ch., Bai S., Peng X. et al.** (2013), Improving hydrophobicity of laser textured SiC surface with micro-square convexes, *Applied Surface Science*, 266(1), 51-56.
17. **Ma Ch., Zhu H.** (2011), An optimum design model for textured surface with elliptical-shape dimples under hydrodynamic lubrication, *Tribology International*, 44(9), 987-995.
18. **Man H.C., Chiu K.Y., Guo X.** (2010), Laser surface micro-drilling and texturing of metals for improvement of adhesion joint strength, *Applied Surface Science*, 256(10), 3166-3169.
19. **Mourier L., Mazuyer D., Lubrecht A.A. et al.** (2006), Transient increase of film thickness in micro-textured EHL contacts, *Tribology International,* 39(12), 1745-1756.
20. **Ortabasi U., Meier D.L., Easoz J.R. et al.** (1997), Excimer micromachining for texturing silicon solar cells, *Lasers As Tools For Manufacturing II*, SPIE Press, 54-64.
21. **Plančak M., Kostka P., Schrek A.** (2012), *Dictionary of metal forming,* Nakladateľstvo STU, Bratislava.
22. **Preciz** (2012), *1.2842 (90MnCrV8, 19 312 / 19 313),* http://www.preciz.cz/sluzby-hlavni/material-normal/1.2842)
23. **Qiu M., Minson B., Raeymaekers B.** (2013), The effect of texture shape on the friction coefficient and stiffness of gas-lubricated parallel slider bearings, *Tribology International*, 67, 278-288.
24. **Rech B., Kluth O., Repmann T. et al.** (2002), New materials and deposition techniques for highly efficient silicon thin film solar cells, *Solar Energy Materials and Solar Cells*, 74(1-4), 439-447.
25. **Ronen A., Etsion I., Kligerman Y.** (2001), Friction-reducing surface-texturing in reciprocating automotive components, *Tribology Transactions*, 44(3), 359-366.
26. **Samad-Zadeh A., Harsono M., Belikov A. et al.** (2011), The influence of laser-textured dentinal surface on bond strength, *Dental Materials*, 27(10), 1038-1044.
27. **Scaraggi M.** (2012), Textured surface hydrodynamic lubrication: Discussion, *Tribology Letters*, 48(3), 375-391.
28. **Schaeffer R.D.** (2012), *Fundamentals of laser micromachining,* CRC Press. London.
29. **Shen C. and Khonsari M.M.** (2015), Numerical optimization of texture shape for parallel surfaces under unidirectional and bidirectional sliding, *Tribology International,* 82, 1-11.
30. **Stašić J., Gaković B., Perrie W. et al.** (2011), Surface texturing of the carbon steel AISI 1045 using femtosecond laser in single pulse and scanning regime, *Applied Surface Science,* 258(1), 290-296.
31. **Tang W., Zhou Y., Zhu H. et al.** (2013), The effect of surface texturing on reducing the friction and wear of steel under lubricated sliding contact, *Applied surface science*, 273, 199-204.
32. **Engineering ToolBox** (2014), *Friction and coefficients of friction, (*http://www.engineeringtoolbox.com/friction-coefficients-d_778.html)
33. **Varenberg M., Halperin G., Etsion I.** (2002), Different aspects of the role of wear debris in fretting wear, *Wear*, 252(11-12), 902-910.
34. **Vilhena L.M., Sedlaček M., Podgornik B. et al.** (2009), Surface texturing by pulsed Nd:YAG laser, *Tribology International,* 42(10), 1496-1504.
35. **Wahl R., Schneider J., Gumbsch P.** (2012), Influence of the real geometry of the protrusions in microtextured surfaces on frictional behaviour, *Tribology Letters*, 47(3), 447-453.
36. **Yan J., Zhang Z., Kuriyagawa T. et al.** (2010), Fabricating microstructured surface by using single-crystalline diamond endmill, *Int. Journal of Advanced Manufacturing Technology,* 51, 957-964.
37. **Zhu X.P., Lei M.K., Ma T.C.** (2003), Surface morphology of titanium irradiated by high-intensity pulsed ion beam*, Nuclear Instruments & Methods in Physics Research Section B: Beam Interactions with Materials and Atoms*, 211(1), 69-79.
38. **Zum Gahr K.H., Wahl R., Wauthier K.** (2009), Experimental study of the effect of microtexturing on oil lubricated ceramic/steel friction pairs, *Wear*, 267(5-8), 1241-1251.

Acknowledgement: This work was supported by the research project, entitled: Innovative methods of sheet metal forming tools surfaces improvement - R&D (Manunet 2014/11283); and VEGA project: Laser surface texturing technology research for an optimizing of tribological conditions in the sheet metal forming processes (0669/15).

DE GRUYTER
OPEN

DOI 10.1515/ama-2017-0021 acta mechanica et automatica, vol.11 no.2 (2017)

THE CALIBRATION PROCESS AND METROLOGICAL ANALYSIS OF A TRANSDUCER USED TO MEASURE TWO PHYSICAL QUANTITIES

Adam IDŹKOWSKI*, Jerzy GOŁĘBIOWSKI*, Wojciech WALENDZIUK*

*Faculty of Electrical Engineering, Bialystok University of Technology, ul. Wiejska 45D, 15-351 Bialystok, Poland

a.idzkowski@pb.edu.pl, j.golebiowski@pb.edu.pl, w.walendziuk@pb.edu.pl

received 10 October 2016, revised 17 May 2017, accepted 19 May 2017

Abstract: This article presents a way of calibration of an unconventional two-current circuit, named 2J+2R, which consists of two current sources and two referential resistors connected to the circuit mass. This bridge was used to measure the beam deflection and the temperature increase simultaneously with the use of a pair of metal strain gauges. This paper contains theoretical and corrected (after calibration) processing characteristics of the measurement circuit. Calibration coefficients of both inputs, responsible for measurement of the measured values in the places where the strain gauges are attached, were calculated. Moreover, the standard combined and expanded uncertainties of both calibration coefficients were calculated and an uncertainty budget was made.

Key words: Measurement Systems, Calibration, Measurement Uncertainty, Strain Gauges, Temperature

1. INTRODUCTION

This article contains a description of a circuit used to measure the increase of two physical quantities simultaneously, e.g. the increase of a cantilever beam deflection and the increase of temperature. A double-output system of a two-current bridge (2J+2R) was applied. The output voltages of this direct current bridge are functions of differences and sums of the resistance increases of two foil strain gauges attached to a cantilever beam. Such circuit can be an alternative for system solutions in the case when deflection and temperature need to be recorded in the same point of the measured element (Idzkowski et al., 2015; Cappa et al., 2001; Paker, 1993). Also other solutions can be treated as differential measurement circuits, e.g. a classic double bridge (Pedersen et al., 2005) or an impedance unbalanced bridge (Musiol et al., 2010).

All devices of this type need to be calibrated. The process of calibration can be conducted with the use of special equipment, e.g. additional resistors regulated in the bridge circuit (Surya et al., 2011), or through a microprocessor circuit which corrects numerically the function dependence between the output signal and the measured quantity.

In this article, a programming way (using a microprocessor circuit) of calibration is described. The aim of the device is to record continuously the changes of the beam deflections caused by the micrometer screw in a certain temperature range. The values of deflection and temperature changes are calculated on the basis of the calibration coefficients during data recording and given online on the computer screen. In order to determine the corrected values of the deflection and temperature changes, the values of output voltages obtained during calibration of the measurement device (for min. and max. deflection at constant temperature) and the voltage values measured online are needed.

Converting the output voltages into the measured values demanded determining the uncertainty. Therefore, the analysis of standard uncertainties (Joint Committee of Guides in Metrology, 2008) of calibration coefficients for both measure values was carried out.

2. SENSORS AND A MEASUREMENT SYSTEM OF A DOUBLE-OUTPUT TRANSDUCER OF THE RESISTANCE AND VOLTAGE INCREASES OF SUM AND DIFFERENCE

In order to conduct research concerning an unconventional circuit for simultaneous measurement of two physical quantities, a set of two foil strain gauges TF-3/120 (TENMEX, 2016) was used. The strain gauges have a linear characteristics average relative resistance increase ε_W in the function of the small of the beam deflection X and its initial value $X_{\min}$

$$\varepsilon_W = a_d(X - X_{\min}) + b_d, \tag{1}$$

where: a_d – coefficient of the characteristics slope (in the analyzed case, the free word b_d, responsible for the offset error ($b_d = 0$)), was rejected.

The relative temperature increase of resistance ε_T for the strain gauges depends linearly on the difference of the temperature T and its minimum value $T_{\min}$ (VISHAY Precision Group, 2007)

$$\varepsilon_T = \alpha(T - T_{\min}). \tag{2}$$

Formula (2) contains the temperature coefficient of resistance α [1/°C]. It represents the sum of two components: thermal expansion of the strain gauge mesh material (constantan) and the difference of the thermal expansion coefficients of the strain gauges and the material of the surface. The difference is multiplied by the deflection sensitivity coefficient of the strain gauges (VISHAY Precision Group, 2007).

The set of two strain gauges, mentioned above, was connected to an unconventional two-current bridge 2J+2R (Fig. 1) and

Adam Idźkowski, Jerzy Gołębiowski, Wojciech Walendziuk DOI 10.1515/ama-2017-0021

a data acquisition mode (Fig. 2). The worked out measurement system allows to determine directly the values of the difference $\varepsilon_1 - \varepsilon_2$ and the sum $\varepsilon_1 + \varepsilon_2$ of the resistance relative increases R_1 and R_2. The equations in the function of the output voltages, assuming that $\varepsilon_1+\varepsilon_2 \ll 1$, are presented below.

$$\varepsilon_W = \frac{(\varepsilon_1-\varepsilon_2)W}{2} = \frac{2\,(U_{ABW}-U_{ABWmin})}{\bar{J}R_0}, \tag{3}$$

$$\varepsilon_T = \frac{(\varepsilon_1+\varepsilon_2)W}{2} = \frac{3(U_{DCW}-U_{DCW\min})}{\bar{J}R_0}, \tag{4}$$

where: $U_{ABW}=WU_{AB}$, $U_{DCW}=WU_{DC}$, $U_{ABW\min}=WU_{AB\min}$, $U_{DCW\min}=WU_{DC\min}$, W - voltage amplification coefficient of the amplifiers, $\bar{J}=\frac{J_1+J_2}{2}$ – current mean average of both current sources (LT3092) supplying the circuit, $R_{r1}=R_{r2}=R_0$. Equations (3) and (4) can be obtained by solving the system of equations for the circuit, presented in Fig. 1, with the nodal analysis, where $U_{AB}=V_A-V_B$, $U_{DC}=V_D-V_C$.

It is worth stressing that the current $\bar{J}$, which is the mean average of the currents of both sources, was determined by measuring the voltage decrease $\overline{U}_{RJ1}$, $\overline{U}_{RJ2}$ on R_{J1} and R_{J2} resistances. It can be therefore assumed that

$$\bar{J}=0.5\left(\frac{\overline{U}_{RJ1}}{R_{J1}}+\frac{\overline{U}_{RJ2}}{R_{J2}}\right). \tag{5}$$

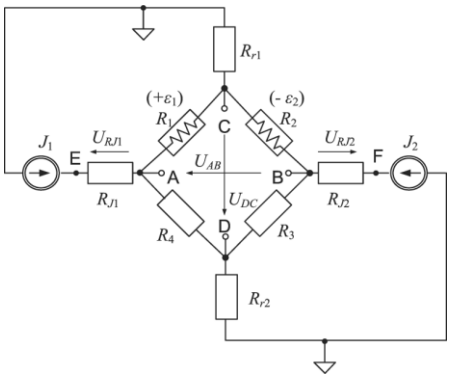

Fig. 1. Two-current bridge (2J+2R)

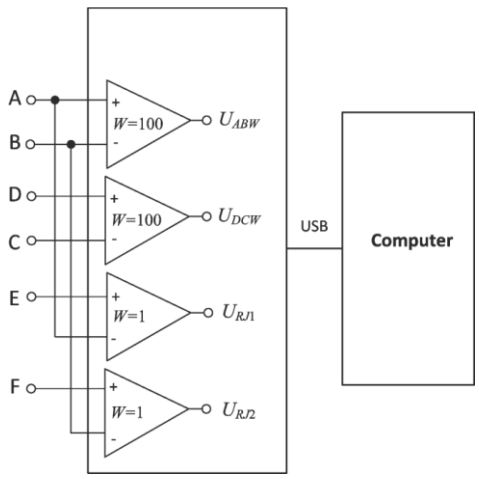

Fig. 2. LabJack data acquisition module with AD623A amplifiers of *W* amplification

It results from equations (3) and (4) that after attaching a strain gauge R_1 on the upper and the strain gauge R_2 on the lower surface of the beam, the voltage being the function of the beam deflection change can be obtained on one output of the system, and the voltage being function of the temperature change – on the opposite output.

3. CHARACTERISTICS OF THE STRAIN GAUGE DEFLECTION AND TEMPERATURE CHANGES IN THE FUNCTION OF THE 2J+2R BRIDGE OUTPUT VOLTAGES

Equations (1) and (2) were applied in formulas (3) and (4) respectively. The measured values of deflection change ΔX_m and temperature change ΔT_m can be then defined on the basis of average values of the bridge output voltages $\overline{U}_{ABW}$, $\overline{U}_{DCW}$, $\overline{U}_{ABW\min}$, $\overline{U}_{DCW\min}$ and current $\bar{J}$

$$X-X_{\min}=\Delta X_m=\frac{2}{\bar{J}R_0 a_d}(\overline{U}_{ABW}-\overline{U}_{ABW\min})=c_1(\overline{U}_{ABW}-\overline{U}_{ABW\min}), \tag{6}$$

$$T-T_{\min}=\Delta T_m=\frac{3}{\bar{J}R_0\alpha}(\overline{U}_{DCW}-\overline{U}_{DCW\min})=e_1(\overline{U}_{DCW}-\overline{U}_{DCW\min}), \tag{7}$$

where: $c_1=\frac{2}{\bar{J}R_0 a_d}$, $e_1=\frac{3}{\bar{J}R_0\alpha}$.

In the real circuit, the slope characteristics needs to be corrected. This was done through introducing k_1 and k_2 multipliers, which are further called calibration coefficients. The corrected values of the deflection changes ΔX_p and the temperature changes ΔT_p are products of calibration coefficients and the measured values ΔX_m and ΔT_m, defined by formulas (6) and (7)

$$\Delta X_p = k_1 \Delta X_m, \tag{8}$$

$$\Delta T_p = k_2 \Delta T_m. \tag{9}$$

The way of determining multipliers k_1 and k_2 is discussed in the following section.

4. COEFFICIENTS OF CALIBRATION AND VOLTAGE SENSITIVITY TO THE BEAM DEFLECTION AND TEMPERATURE INCREASES

After substituting (6) into (8), the corrected value of the deflection change was obtained

$$\Delta X_p = k_1 c_1(\overline{U}_{ABW}-\overline{U}_{ABW\min}). \tag{10}$$

The graphic interpretation of equation (10) is presented in Fig. 3.

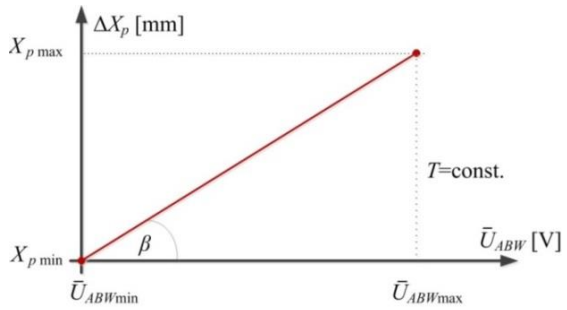

Fig. 3. The corrected characteristics of the beam deflection at constant temperature

Minimum and maximum $\overline{U}_{ABW\max}$, $\overline{U}_{ABW\min}$ values are determined through measurements. Due to the rules of calibration,

DOI 10.1515/ama-2017-0021

unknown corrected values $X_{p\max}$, $X_{p\min}$ were substituted by $X_{\min}$ and $X_{\max}$ reference values (Fig. 3). As it is known, the slope coefficient (10) is also the tangent of the slope angle.

$$k_1 c_1 = \tan\beta = \frac{X_{\max} - X_{\min}}{\bar{U}_{ABW\,\max} - \bar{U}_{ABW\,\min}}. \tag{11}$$

After taking c_1 (as in (6)) into account, the coefficient of measurement calibration of deflection change at constant temperature was determined

$$k_1 = \frac{X_{\max} - X_{\min}}{\bar{U}_{ABW\,\max} - \bar{U}_{ABW\,\min}} \frac{\bar{J} R_0 a_d}{2} = \frac{\Delta X}{\Delta \bar{U}_{ABW}} \frac{\bar{J} R_0 a_d}{2}. \tag{12}$$

The voltage sensitivity U_{ABW} for 1 mm of the beam deflection results from formula (10)

$$S_{XU} = \frac{1}{k_1 c_1} = \frac{\Delta \bar{U}_{ABW}}{\Delta X}. \tag{13}$$

After substituting (7) into (9), similarly, the coefficient of measurement calibration of temperature change at constant beam deflection was obtained

$$k_2 = \frac{T_{\max} - T_{\min}}{\bar{U}_{DCW\,\max} - \bar{U}_{DCW\,\min}} \frac{\bar{J} R_0 \alpha}{3} = \frac{\Delta T}{\Delta \bar{U}_{DCW}} \frac{\bar{J} R_0 \alpha}{3}. \tag{14}$$

where: $T_{\max}$ and $T_{\min}$ are reference values. The coefficient of voltage sensitivity to temperature change of 1 K equals

$$S_{TU} = \frac{\Delta \bar{U}_{DCW}}{\Delta T}. \tag{15}$$

4.1. Experimental Determining of the Temperature and Beam Deflection Increases and the K1 And K2 Calibration Coefficients

The measured values ΔX_m and ΔT_m were determined on the basis of U_{ABW}, $U_{ABW\min}$, U_{DCW}, $U_{DCW\min}$, U_{Rf1}, U_{Rf2} voltage records from the 2J+2R bridge circuit with the use of the lab Jack UE-9Pro data acquisition system, in the way presented in Fig. 2. Two strain gauges attached on the upper and lower surfaces of the beam (as presented in Fig. 4) were included into the bridge circuit with the use of a screen wire.

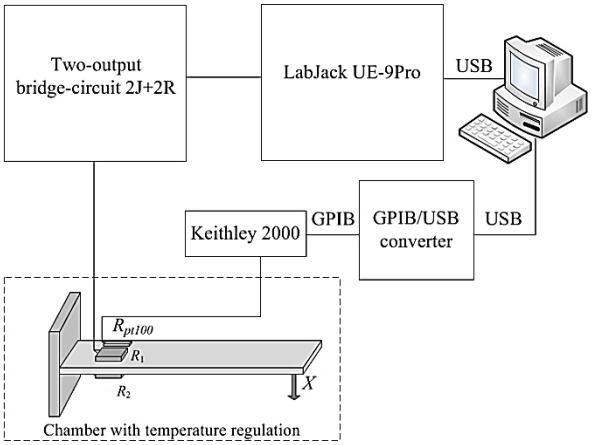

Fig. 4a. Laboratory stand consisting of a two-current bridge (2J+2R), a beam with attached strain gauges and a Pt100 sensor, a heating chamber with a thermostat, a LabJack measurement module, a Keithley 2000 multimeter and a computer

In order to determining the corrected values ΔX_p and ΔT_p, it is vital to know the minimum and maximum reference deflection and reference temperature. Therefore, a platinum Pt100 RTD (class A) was attached on the upper surface of the beam, next to the strain gauge. The RTD was connected to a Keithley 2000 multimeter. The set of the platinum Pt100 RTD with a multimeter was used to set the $T_{\min}$ and $T_{\max}$ temperature values, required to calibrate the bridge, precisely.

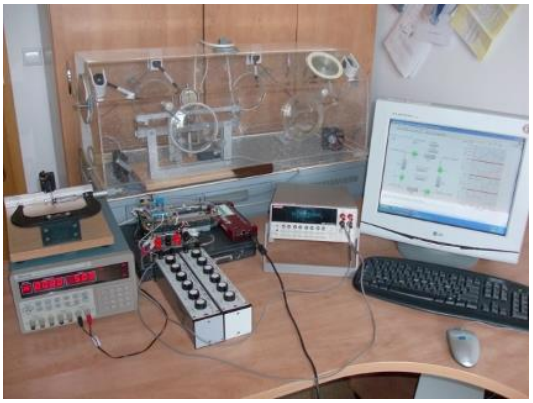

Fig. 4b. General view of the laboratory stand

The beam deflections were done with the use of a micrometer screw within the ⟨0,10⟩ mm range with the limiting error of ±0.01 mm. The mechanism deflecting the beam with attached strain gauges and the Pt100 sensor was placed in a heating chamber with a thermostat. This gave the experiment the temperature stability during the bridge calibration (in the range of ±1 °C). It is crucial that all positions of deflection on the micrometer screw are performed at a selected, constant temperature.

Before the experiment, the temperature coefficient value of α resistance of the strain gauge attached to the beam was checked through measuring the resistance increases of the strain gauges at the temperature change from 22 °C to 62 °C. The experimentally determined coefficient equalled $4.07 \cdot 10^{-5}$[1/°C]. The manufacturer of the strain gauges gives the coefficient value of $4 \cdot 10^{-5}$[1/°C] (for a measurement mesh of strain gauges made of constantan) (TENMEX, 2016). Due to the fact that the difference is insignificant, the value given by the manufacturer was taken in further calculations.

Connecting the temperature meter and the LabJack system to the computer with the use of the USB interface enabled simultaneous reading the voltage on the bridge and the adequate temperature in the chamber. The results recalculated with the use of a computer program (created in the LabVIEW environment) were recorded in a text file. The measurements were conducted at the following LabJack data acquisition system settings: 20 bits of the A/C transducer resolution, 5 μV voltage resolution of the measurement.

4.2. Comparison of the Beam Deflection Values and the Temperature Changes Resulted from the Measurement Equations Before and after Calibration. Metrological Estimation of the Results Differences

The measurement experiment aimed at comparing the values of deflection increases ΔX_m (6) and the temperature increases ΔT_m (7) obtained without calibration with the ΔX_p (8) and ΔT_p (9) values obtain as a result of calibration. Therefore, there was

DOI 10.1515/ama-2017-0021

a necessity to determine the k_1 and k_2 calibration coefficients experimentally.

Tab. 1 and 2 present the measurement results of the bridge output voltages and the supplying current at the following temperatures: $T_{\min}$=22 °C and $T_{\max}$= 62 °C, for the beam deflections set with the use of the micrometric screw within the range of ⟨0,10⟩ mm with the step of 1 mm. Each value is the arithmetic mean of N= 200 recorded samples.

Tab. 1. Voltage and current mean values for sensors at $T_{\min}$=22 °C for subsequent beam deflection values

X	$\bar{U}_{ABW}$ (T=22 °C)	$\bar{U}_{DCW}$ (T=22 °C)	$\bar{J}$
mm	μV	μV	μA
0.00	-40867.3(min)	5060.9	10054.9
1.00	-35806.5	4743.0	10054.8
2.00	-33202.0	4239.9	10054.7
3.00	-28259.3	4257.0	10054.7
4.00	-24290.6	4142.8	10054.8
5.00	-19625.3	3994.8	10054.8
6.00	-14685.8	4014.4	10054.8
7.00	-8959.9	3764.7	10054.8
8.00	-6340.7	3357.4	10055.0
9.00	-2354.5	3373.3	10055.0
10.00	1539.0(max)	3553.6	10055.2

Tab. 2. Voltage and current mean values for sensors at $T_{\min}$=62 °C for subsequent beam deflection values

X	$\bar{U}_{ABW}$ (T=62 °C)	$\bar{U}_{DCW}$ (T=62 °C)	$\bar{J}$
mm	μV	μV	μA
0.00	-51256.5(min)	-94704.2	10054.3
1.00	-46244.4	-94540.2	10054.3
2.00	-40514.1	-95133.6	10054.2
3.00	-39103.7	-94788.3	10054.5
4.00	-33479.8	-95694.5	10054.4
5.00	-27306.3	-95882.1	10054.3
6.00	-22926.6	-96213.6	10054.2
7.00	-21209.7	-97158.6	10054.6
8.00	-19232.6	-97337.2	10054.6
9.00	-10317.2	-96427.9	10054.3
10.00	-5438.7(max)	-96257.5	10054.2

The k_1 and k_2 calibration coefficients were calculated on the basis of (12) and (14). The results are given in Tab. 3.

On the basis of the values included in Tab. 3, a change of the k_1 calibration coefficient value can be observable. The value of this coefficient is greater (of 8.05%) for the lower temperature. In the case of the k_2 coefficient it can be assumed that the X value, for which the calibration is carried out, is not important (the change in this case is only 0.05%).

Tab. 3. Values of the k_1 and k_2 calibration coefficients

	Range of X: X_{min}=0 mm X_{max}=10 mm		Range of T: T_{min}=22°C T_{max}=62°C
	k_1		k_2
T=22°C	1.20232	X=0 mm	0.66182
T=62°C	1.11279	X=10 mm	0.66152

The following fixed values were assumed in order to conduct the calculations: a_d=0.00832 mm^{-1} [2], W=100, α=0.00004 °C^{-1}, R_0=121.116 Ω.

Tab. 4 and 5, accept the X values set on the screw (at two fixed temperatures $T_{\min}$=22 °C and $T_{\max}$=62 °C), contain also the ΔX_m values – the beam deflection change calculated on the basis of the measurement equation (6), and ΔX_p – the corrected deflection change obtained from the equation (10).

Moreover, the $\Delta_{Xm}=\Delta X_m-X$ and $\Delta_{Xp}=\Delta X_p-X$ differences were calculated for both temperatures. The Δ_{Xp} differences were related to the $\Delta X=X_{\max}-X_{\min}$ measurement range, calculating relative errors of the δ_{p22} and δ_{p62} determined deflection values.

Tab. 4. The ΔX_m values obtained on the basis of the measurement equation (6) and the ΔX_p values determined on the basis of the calibration function (10) at the $T_{\min}$=22 °C fixed temperature. The differences of the two values and the X value set on the micrometric screw and the relative value of the determined deflection value

X	ΔX_m	ΔX_p	ΔX_m-X	ΔX_p-X	$\delta_{p22}=\frac{(\Delta X_p-X)100}{X_{\max}-X_{\min}}$
mm	mm	mm	mm	mm	%
0.00	0.00	0.00	0.00	0.00	0.00
1.00	0.99	1.19	-0.01	0.19	1.93
2.00	1.50	1.81	-0.50	-0.19	-1.92
3.00	2.47	2.97	-0.53	-0.03	-0.27
4.00	3.25	3.91	-0.75	-0.09	-0.91
5.00	4.17	5.01	-0.83	0.01	0.09
6.00	5.14	6.17	-0.86	0.17	1.74
7.00	6.26	7.52	-0.74	0.52	5.24
8.00	6.77	8.14	-1.23	0.14	1.42
9.00	7.55	9.08	-1.45	0.08	0.82
10.00	8.32	10.00	-1.68	0.00	0.00

Tab. 5. The ΔX_m values obtained on the basis of the measurement equation (6) and the ΔX_p values determined on the basis of the calibration function (10) at the $T_{\min}$=22 °C fixed temperature. The differences of the two values and the X value set on the micrometric screw and the relative value of the determined deflection value

X	ΔX_m	ΔX_p	ΔX_m-X	ΔX_p-X	$\delta_{p62}=\frac{(\Delta X_p-X)100}{X_{\max}-X_{\min}}$
mm	mm	mm	mm	mm	%
0.00	0.00	0.00	0.00	0.00	0.00
1.00	0.98	1.09	-0.02	0.09	0.94
2.00	2.11	2.34	0.11	0.34	3.45
3.00	2.38	2.65	-0.62	-0.35	-3.48
4.00	3.49	3.88	-0.51	-0.12	-1.20
5.00	4.70	5.23	-0.30	0.23	2.27
6.00	5.56	6.18	-0.44	0.18	1.83
7.00	5.89	6.56	-1.11	-0.44	-4.42
8.00	6.28	6.99	-1.72	-1.01	-10.11
9.00	8.03	8.94	-0.97	-0.06	-0.65
10.00	8.99	10.0	-1.01	0.00	0.00

Fig. 5 – 8 were done on the basis of the values from Tab. 4 and 5. Moreover, the slope coefficients and the regression lines shifts were calculated: $\Delta\widehat{X}_m=m_1X+m_2$ (for $T_{\min}$=22 °C

DOI 10.1515/ama-2017-0021

and T_{max}=62 °C) and $\Delta\hat{X}_p = p_1 X + p_2$ (for T_{min}=22 °C and T_{max}=62 °C).

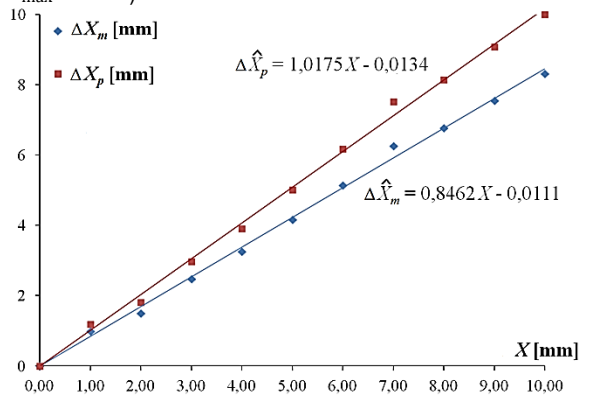

Fig. 5. Linear regression functions of the measured deflection change (ΔX_m) and the corrected deflection change (ΔX_p), depending on the X deflection set on the screw (at T_{min}=22 °C)

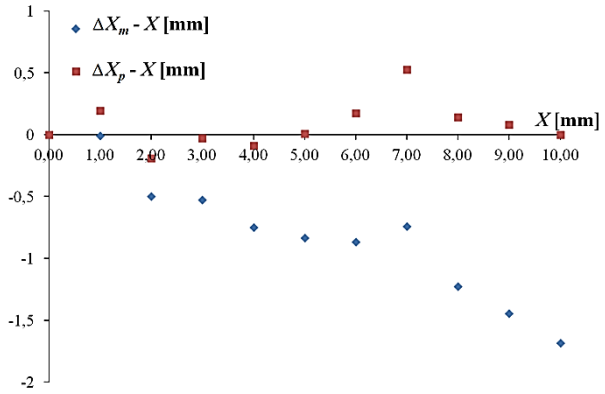

Fig. 6. The ΔX_m -X and ΔX_p -X differences (at T_{min}=22 °C)

This can be seen in Fig. 5 and 7 that, due to the temperature increase from T_{min} to T_{max}, the slope and lines shift coefficients change. However, the p_1 slope coefficient of the corrected regression lines are far closer to the ideal value (the value of one) than those of the lines which have not been corrected (without m_1). Fig. 6 and 8 show that, with very few exceptions, the $|\Delta X_p - X|$ differences are smaller than $|\Delta X_m - X|$ at almost whole range of changes $\langle X_{min}, X_{max}\rangle$. Therefore, calibration has a positive influence on the measurement precision. The errors of the δ_{pT} determined deflection value related to the $\Delta X = X_{max} - X_{min}$ for both temperatures were assigned as: δ_{p22} (T_{min}=22 °C) and δ_{p62} (T_{max}=62 °C).

With some exceptions, the obtained $|\delta_{p22}|$ values were smaller in comparison with $|\delta_{p62}|$ values. This means that the calibration has better results in the lower temperature. The maximum relative error of the determined deflection value $|\delta_{p62}|$ equals 10.11%.

Tab. 6 contains the voltage coefficient of temperature sensitivity values (S_{TU}) calculated on the basis of (15) for different values of X. The fixed mean value of S_{TU}= -2496.9 µV/°C ≈-2.5 mV/°C was assumed within the range of $X \in \langle 0,10\rangle$ mm.

Tab. 7 compares the temperature change values ΔT_m (without calibration) and ΔT_p (after calibration) obtained as a result of applying equations (7), (9), (14) at constant deflection X = 0 mm. Moreover, $\Delta_{Tm} = \Delta T_m - \Delta T$ and $\Delta_{Tp} = \Delta T_p - \Delta T$ for X=0 mm were calculated. The Δ_{Tp} differences in relation to the T_{max}-T_{min} measurement range were determined by calculating the relative errors of the determined temperature change value δ_{Tp}.

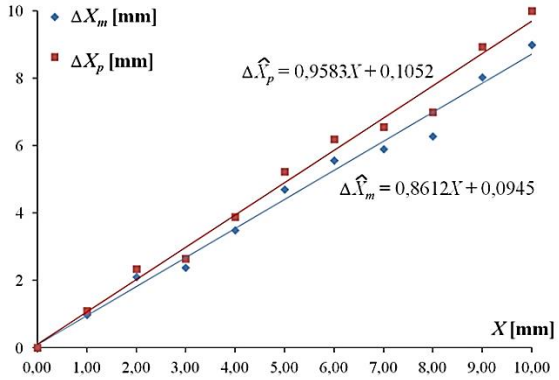

Fig. 7. Linear regression functions of the measured deflection change (ΔX_m) and the corrected deflection change (ΔX_p), depending on the X deflection set on the screw (at T_{min}=62 °C)

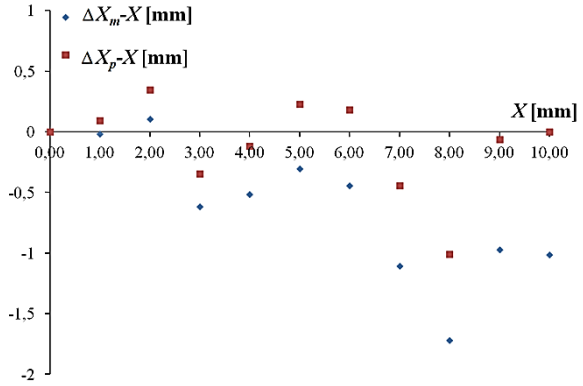

Fig. 8. The ΔX_m -X and ΔX_p -X differences (at T_{min}=62 °C)

Tab. 6. Voltage coefficient of temperature sensitivity (S_{TU}) determined on the basis of the voltage measurement at two temperatures: T_{min}=22 °C and T_{max}=62 °C for the X value fixed with the use of a micrometric screw

X	$\overline{U}_{DCWmin}$	$\overline{U}_{DCWmax}$	S_{TU}
mm	µV	µV	µV/°C
0.00	5060.9	-94704.2	-2494.1
1.00	4743.0	-94540.2	-2482.1
2.00	4239.9	-95133.6	-2484.3
3.00	4257.0	-94788.3	-2476.1
4.00	4142.8	-95694.5	-2495.9
5.00	3994.8	-95882.1	-2496.9
6.00	4014.4	-96213.6	-2505.7
7.00	3764.7	-97158.6	-2523.1
8.00	3357.4	-97337.2	-2517.4
9.00	3373.3	-96427.9	-2495.0
10.00	3553.6	-96257.5	-2495.3

Also, linear regression functions $\Delta\hat{T}_m = m_3 \Delta T + m_4$ (for X = 0 mm) and $\Delta\hat{T}_p = p_3 \Delta T + p_4$ (for X = 0 mm).are presented (Fig. 9). Fig. 10 shows differences between the values calculated from equations (7) or (9) and the reference value ΔT. The maximum error value δ_{Tp} (after calibration) was 1.71%.

Adam Idźkowski, Jerzy Gołębiowski, Wojciech Walendziuk
DOI 10.1515/ama-2017-0021

Tab. 7. Temperature increase values (ΔT_m) obtained from (7) and ΔT_p values determined on the basis of the calibration function (9) for T_{min}=22 °C and T_{max}=62 °C at fixed deflection X=0 mm. The differences $\Delta_{Tm}=\Delta T_m-\Delta T$, $\Delta_{Tp}=\Delta T_p-\Delta T$ and the relative error δ_{Tp} (Δ_{Tp} in relation to the T_{max}- T_{min} changes)

ΔT	$\overline{U}_{DCW}$	$\Delta\overline{T}_m$	$\Delta\overline{T}_p$	$\Delta\overline{T}_m-\Delta T$	$\Delta\overline{T}_p-\Delta T$	$\delta_{Tp}=\frac{\Delta_{Tp}100}{T_{max}-T_{min}}$
°C	mV	°C	°C	°C	°C	%
0	5.06 (min)	0.0	0.00	0.00	0.00	0.00
5	-7.73	7.7	5.13	2.65	0.13	0.32
10	-20.70	15.4	10.33	5.42	0.33	0.82
15	-33.15	22.9	15.32	7.87	0.32	0.81
20	-45.74	30.4	20.37	10.41	0.37	0.92
25	-58.36	38.0	25.43	12.96	0.43	1.07
30	-70.81	45.4	30.42	15.41	0.42	1.05
35	-83.53	53.0	35.52	18.03	0.52	1.30
40	-96.41 (max)	60.7	40.68	20.74	0.68	1.71

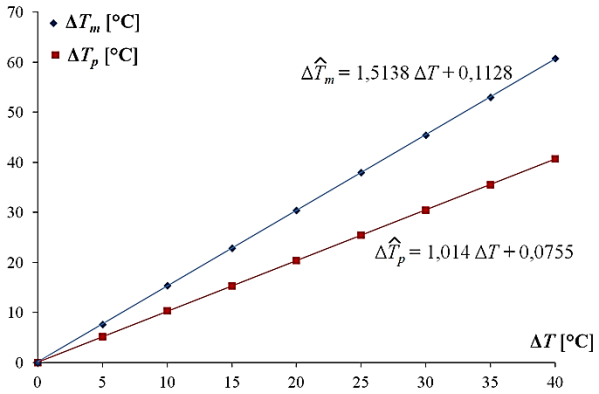

Fig. 9. Linear regression functions of the temperature increase ΔT_m and ΔT_p depended on the temperature increase (ΔT) set on the thermostat (at the deflection X=0 mm)

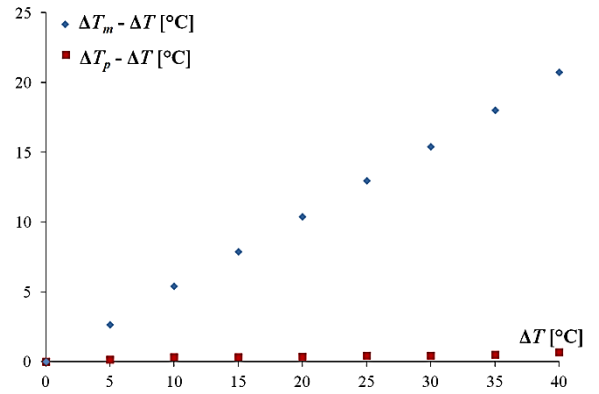

Fig. 10. The values of $\Delta\overline{T}_m-\Delta T$ and $\Delta\overline{T}_p-\Delta T$ differences for subsequent values of temperature increase (ΔT) set on the thermostat (at the deflection X=0 mm)

Tab. 7 and Fig. 9, 10 clearly show that calibration increases significantly the precision of measurement.

5. THE ANALYSIS OF THE K1 AND K2 CALIBRATION COEFFICIENTS UNCERTAINTY

According to (7), the k_1 Calibration coefficient was calculated. Discussing the k_1 coefficient requires information concerning: the values of numerous quantities listed in Tab. 8 (in the first column), their uncertainties (three middle columns) and the assumed probability distribution (the last column). The measurement procedure for indirect measurements when the input quantities are not correlated was used.

The combined uncertainty was calculated from equation (16)

$$u_c(k_1)=\sqrt{\left(\frac{\partial k_1}{\partial \bar{J}}\right)^2\cdot u_c^2(\bar{J})+\left(\frac{\partial k_1}{\partial(\Delta\bar{U}_{ABW})}\right)^2\cdot u_c^2(\Delta\bar{U}_{ABW})+\left(\frac{\partial k_1}{\partial(\Delta X)}\right)^2\cdot u_c^2(\Delta X)+\left(\frac{\partial k_1}{\partial R_0}\right)^2\cdot u_c^2(R_0)}, \quad (16)$$

where:

– the squared combined uncertainty of current measurement $\bar{J}$

$$u_c^2(\bar{J})=\left(\frac{1}{2R_{J1}}\right)^2 u^2(\bar{U}_{RJ1})+\left(\frac{1}{2R_{J2}}\right)^2 u^2(\bar{U}_{RJ2})+\left(\frac{\bar{U}_{RJ1}}{2R_{J1}^2}\right)^2 u^2(R_{J1})+\left(\frac{\bar{U}_{RJ2}}{2R_{J2}^2}\right)^2 u^2(R_{J2}), \quad (17)$$

– the squared combined uncertainty of voltage difference measurement $\Delta\bar{U}_{ABW}$

$$u_c^2(\Delta\bar{U}_{ABW})=u^2(\bar{U}_{ABW\max})+u^2(\bar{U}_{ABW\min}), \quad (18)$$

– the squared combined uncertainty of deflection difference measurement ΔX

$$u_c^2(\Delta X)=u^2(X_{\max})+u^2(X_{\min}). \quad (19)$$

Tab. 9 contains the product of sensitivity coefficients (in the second power) and the combined uncertainties (in the second power, calculated on the basis of equations (17 – 19)). They are components (in the second power) of the combined uncertainty of the k_1 coefficient. Calculating a component related to the resistance dispersion (R_0) was conducted with the assumption that the limiting error equals δ_{grR0}=±0.5% (estimated with the use of the exact differential).

The expanded uncertainty $U(k_1)$ was calculated with the assumption that the expansion coefficient k_p=2 and the confidence interval p=0.95

$$U(k_1)=k_p\sqrt{u_c^2(k_1)} \quad (20)$$

The complete result of the calculated k_1 coefficient (at T=22°C)

$$k_1=1.202\pm0.015 \text{ for } k_p=2 \text{ and } p=95\%. \quad (21)$$

The relative combined uncertainty $U_w(k_1)$ equals

$$U_w(k_1)=\frac{U(k_1)}{k_1}100\%=\pm1.25\%. \quad (22)$$

The limiting measurement error for the Pt100 sensor of class A equals $\pm(0.15+0.002\cdot T)$. On this basis, the components of the k_2 combined uncertainty coefficient were calculated with the use of equations similar to (16)-(19), and presented in Tab. 10.

DOI 10.1515/ama-2017-0021

Tab. 8. Uncertainty budget of the k_1 calibration coefficient: input quantities, their standard uncertainties and probability distribution

Measurement quantities symbol (x_i)	Uncertainty of A type $u_A(x_i)$	Uncertainty of B type $u_B(x_i)$	Combined standard uncertainty $u(x_i)$	Type of probability distribution
U_{RJ1}	$\sqrt{\frac{\sum_{k=1}^{N}(U_{RJ1_k}-\bar{U}_{RJ1})^2}{N(N-1)}}$	$\frac{\Delta_{grU}}{\sqrt{3}}$	$\sqrt{u_A^2(U_{RJ1})+u_B^2(U_{RJ1})}$	convolution of normal and continuous uniform distribution
R_{J1}	-	$\frac{\Delta_{grRJ}}{\sqrt{3}}$	$u_B(R_{J1})$	continuous uniform distribution
U_{RJ2}	$\sqrt{\frac{\sum_{k=1}^{N}(U_{RJ2_k}-\bar{U}_{RJ2})^2}{N(N-1)}}$	$\frac{\Delta_{grU}}{\sqrt{3}}$	$\sqrt{u_A^2(U_{RJ2})+u_B^2(U_{RJ2})}$	convolution of normal and continuous uniform distribution
R_{J2}	-	$\frac{\Delta_{grRJ}}{\sqrt{3}}$	$u_B(R_{J2})$	continuous uniform distribution
$U_{ABW\max}$	$\sqrt{\frac{\sum_{k=1}^{N}(U_{ABW\max_k}-\bar{U}_{ABW\max})^2}{N(N-1)}}$	$\frac{\Delta_{grU}}{\sqrt{3}}$	$\sqrt{u_A^2(U_{ABW\max})+u_B^2(U_{ABW\max})}$	convolution of normal and continuous uniform distribution
$U_{ABW\min}$	$\sqrt{\frac{\sum_{k=1}^{N}(U_{ABW\min_k}-\bar{U}_{ABW\min})^2}{N(N-1)}}$	$\frac{\Delta_{grU}}{\sqrt{3}}$	$\sqrt{u_A^2(U_{ABW\min})+u_B^2(U_{ABW\min})}$	convolution of normal and continuous uniform distribution
R_0	-	$\frac{\Delta_{grR0}}{\sqrt{3}}$	$u_B(R_0)$	continuous uniform distribution
$X_{\max}$	-	$\frac{\Delta_{grX}}{\sqrt{3}}$	$u_B(X_{\max})$	continuous uniform distribution
$X_{\min}$	-	$\frac{\Delta_{grX}}{\sqrt{3}}$	$u_B(X_{\min})$	continuous uniform distribution

The following symbols were assumed: Δ_{grU} – limiting error of the voltage measurement conducted with a LabJack module (±250 μV), Δ_{grRJ} – resistance limiting error R_{J1}= R_{J2}=22 Ω (±0.22 Ω), Δ_{grR0} - resistance limiting error R_0 =121.116 Ω (±0.6 Ω), Δ_{grX} – limiting error of the X deflection measurement conducted with a micrometer screw (±0.01 mm).

Tab. 9. Squared combined uncertainty components of the k_1 and their sum.

$\left(\frac{\partial k_1}{\partial \bar{J}}\right)^2 \cdot u_c^2(\bar{J})$	$\left(\frac{\partial k_1}{\partial(\Delta\bar{U}_{ABW})}\right)^2 \cdot u_c^2(\Delta\bar{U}_{ABW})$	$\left(\frac{\partial k_1}{\partial(\Delta X)}\right)^2 \cdot u_c^2(\Delta X)$	$\left(\frac{\partial k_1}{\partial R_0}\right)^2 \cdot u_c^2(R_0)$	$u_c^2(k_1)$
0.000024	0.000033	0.000001	0.000001	0.000059

Tab. 10. Squared combined uncertainty components of the k_2 and their sum.

$\left(\frac{\partial k_2}{\partial \bar{J}}\right)^2 \cdot u_c^2(\bar{J})$	$\left(\frac{\partial k_2}{\partial(\Delta\bar{U}_{DCW})}\right)^2 \cdot u_c^2(\Delta\bar{U}_{DCW})$	$\left(\frac{\partial k_2}{\partial(\Delta T)}\right)^2 \cdot u_c^2(\Delta T)$	$\left(\frac{\partial k_2}{\partial R_0}\right)^2 \cdot u_c^2(R_0)$	$u_c^2(k_2)$
0.000059	0.000002	0.000010	0.000001	0.000072

The k_2 coefficient was determined on the basis of the data from tab. 10, with consideration of the expanded uncertainty

$$k_2 = 0.662 \pm 0.017 \text{ for } k_p = 2 \text{ and } p = 95\%. \quad (23)$$

The relative expanded uncertainty $U_w(k_2)$ equals

$$U_w(k_2) = \frac{U(k_2)}{k_2} 100\% = \pm 2.56\%. \quad (24)$$

Relative uncertainty values of the expanded calibration coefficients are less than 5%.

6. CONCLUSIONS

An example of a direct current bridge (2J+2R) with two foil strain gauge sensors stuck on a cantilever beam application

is described. The discussed circuit is a transducer of two quantities, i.e. the beam deflection change and the temperature change into two analogue DC voltages. The measurement equations (6) and (7) were applied for the tested circuit. After taking the described assumptions into account, the deflection and temperature changes are proportional towards the appropriate output voltage. The obtained results (Tab. 4 – column 2, Tab. 5 – column 2, Tab. 7 – column 3) required calibration. Calibration coefficients (k_1 and k_2) were calculated from equations (12) and (14). The value and precision of determining those coefficients influence significantly the beam deflection and the temperature change obtained during measurements. It results from the values presented in Tab. 3 that determining the precise value of the k_1 is more difficult because its values obtained at $T_{\min}$ and $T_{\max}$ are different of 8.05%. This probably results from the current drift of the supplies used to construct the bridge and its influence on the measured voltage U_{AB}. In the case of the k_2 coefficient the values determined for $T_{\min}$ and $T_{\max}$ differ only of 0.05%. For the purpose of calculations, the fixed voltage coefficient of temperature sensitivity S_{TU} (15) was assumed within the tested range of the beam deflection, i.e. $S_{TU} \approx$-2.5 mV/°C for $X \in \langle 0{,}10 \rangle$ mm.

Equations (8) and (9) describe the values of the beam deflection and temperature change after calibration. The appropriate results are Included in Tab, 4 – column 3, Tab. 5 – column 3 and Tab. 7 – column 4.

Relative errors (Tab 4, 5 and 7 – the last columns), which are the differences between the set and calibrated (with the use of a micrometric screw and a thermal chamber) bridge values related to the measurement ranges of both quantities, were calculated. The maximum relative errors of the determined value of deflection equalled: $|\delta_{p22}|$=5.24% (calibration conducted at 22 °C), $|\delta_{p62}|$=10.11% (calibration conducted at 62 °C). The maximum relative error of the determined value of the temperature change equalled $|\delta_{Tp}|$=1.71% (calibration for X=0 mm).

Additionally, the combined standard uncertainties of the k_1 and k_2 calibration coefficients were determined. The so called "uncertainty budget" was formulated (Tab. 8 – 10). Satisfactory values of relative extended uncertainties $U_w(k_1)=\pm 1.25\%$, $U_w(k_2)=\pm 2.56\%$ for the expansion coefficient $k_p=2$ and the confidence level $p=95\%$ were obtained.

The presented experiments and calculations contribute to the development of alternative circuits applied to simultaneous measurement of a few physical quantities. They may be an interesting and valuable complement of well-known devices conditioning analogue signals (Kalita et al., 2015; Proto et al., 2016, Swartz et al., 2004). The ways of compensating the temperature influence in the inseparable structures of the Wheatstone's bridges (e.g. in the integrated pressure transducers) can be an example INTERSIL (2005), MAXIM Integrated Products Inc. (2002), Mozek et al., (2008). In solutions of this type, an additional temperature sensor, resistors or resistance temperature detectors circuits for compensating e.g. pressure piezoresistive silicon sensors of the X-ducer type, Motorola, are frequently applied (Swartz et al., 2004).

REFERENCES

1. **Cappa P., Marinozzi F., Sciuto S.A.** (2001), A Novel method for the simultaneous measurement of temperature and strain using a three-wire connection, *Measurement Science and Technology*, 12(4), 502-506.
2. **Idzkowski A., Walendziuk W., Warsza Z.L**. (2015), Unconventional double-current crcuit for deflection and temperature simultaneous measurement, *Elektronika ir Elektrotechnika*, 21(1), 23–27.
3. **INTERSIL** (2005), *Sensor circuits and digitally controlled potentiometers*, application note AN135.
4. **JCGM - Joint Committee of Guides in Metrology** (2008), *Evaluation of measurement data – guide to the expression of uncertainty in measurement*.
5. **Kalita K., Das N., Boruah P.K., Sarma U.** (2016), Design and uncertainty evaluation of a strain measurement system, *MAPAN – Journal of Metrology Society of India*, 31(1), 17-24.
6. **MAXIM Integrated Products Inc.** (2002), *Sensor temperature compensation using the four DAC signal conditioning architecture*, application note 1839.
7. **Mozek M., Vrtacnik, D., Resnik D., Aljancic U., Penic S., Amon S.** (2008), Digital self-learning calibration system for smart sensors, *Sensors & Actuators: A. Physical* 141(1), 101-108.
8. **Musiol K., Met A., Skubis T**. (2010), Automatic bridge for comparison of inductance standards, *Measurement*, 43(10), 1661-1667.
9. **Nudzikova, P., Slanina, Z.** (2016), User identification by biometric methods, *Intelligent Systems for Computer Modelling - Advances in Intelligent Systems and Computing,* 423, 181-190.
10. **Parker A.R**. (1993), Simultaneous measurement of temperature and strain using four connecting wires, *NASA Technical Memorandum* 104271.
11. **Pedersen C., Jespersen S.T., Krog J.P., Christensen C., Thomsen E.V.** (2005), Combined differential and static pressure sensor based on a double-bridged structure, *IEEE Sensors Journal* 5 (3), 446- 454.
12. **Proto A., Penhaker M., Bibbo D., Vala D., Conforto S., Schmid M.** (2016), Measurements of generated energy/electrical quantities from locomotion activities using piezoelectric wearable sensors for body motion energy harvesting, *Sensors* ,16(4), 524.
13. **Surya S., Nag S., Fernandes A.J., Gandhi S., Agarwal D., Chatterjee G., Ramgopal Rao V**. (2011), Highly sensitive ΔR/R measurement system for nano-electro-mechanical cantilever based biosensors, *International Symposium on Electronic System Design (ISED)*, 34- 38.
14. **Swartz C., Derrington C., Gragg J.** (2004), *Temperature compensation methods for the Motorola X-ducer pressure sensor element*, Motorola Semiconductor application notes AN840.
15. **TENMEX** (2016), strain gauges producer webpage, http://www.tenmex.pl.
16. **VISHAY Precision Group** (2007), *Measurement of thermal expansion coefficient using strain gages*, technical note TN-513-1, http://www.vishaypg.com/docs/11063/tn5131tn.pdf.

Acknowledgement: The paper was prepared at Bialystok University of Technology within a framework of the S/WE/1/2013 project sponsored by Ministry of Science and Higher Education.